THE UNIVERSITY *of* EDINBURGH

Optimisation and integration of membrane processes in coal-fired power plants with carbon capture and storage

Davide Bocciardo

For the Degree of Doctor of Philosophy

School of Engineering

University of Edinburgh

May 2015

Thesis declaration

I, Davide Bocciardo, certify:

(a) that the thesis has been composed by me, and

(b) either the work is my own or, where I have been a member of a research group, that I have made a substantial contribution to the work, such contribution being clearly indicated, and

(c) that the work has not been submitted for any other degree or professional qualification except as specified.

Signed: 

Date: **25/05/2015**

Acknowledgements

I would first like to thank my supervisors Stefano Brandani and Maria-Chiara Ferrari for believing in me and for giving me the opportunity to grow both personally and professionally in these years. It has been a pleasure to work with you and to be part of the Carbon Capture Group.

I would also like to thank Scottish Power and Energy Technology Partnership (ETP) Scotland for funding this PhD Project.

A special thanks to Daniel Friedrich for his patient mathematical and programming support.

When I think about Edinburgh I think about the great people I met who made me feel home and who are like family to me. A special thanks to the *Criminal Penguins* - Chiara, Daniel, Dave, Enzo, Simone and Steph - for the fantastic time spent together.

Thanks also to Zoe, Dursun, Ares, Elsa, Gabriel, Hilda, Cris and Erika for sharing this adventure with me. I would also like to thank Alessandra, Rita, Adriano, Margherita, Gabriella and Loriana for being such good friends.

Last but not least, a special thanks to my dad, my grandmother Meri and my aunt Carla for their continuous and invaluable support.

Lay summary

Energy generation from fossil fuel power plants has been strongly related to climate change: according to the Intergovernmental Panel on Climate Change, a substantial reduction in greenhouse gases emissions is required in order to limit its consequences. Carbon Capture and Storage can reduce CO_2 emissions and its contribution will be essential in the direction of meeting both national and worldwide reduction targets.

This PhD project - funded by Scottish Power and Energy Technology Partnership Scotland – is focused on CO_2 capture from the flue gas of coal-fired plants. In order to evaluate alternative technologies to the conventional solvent based solution, a feasibility study focusing on membrane gas separation is carried out. Membrane technology is already successfully applied in the oil and gas industry but the characteristics of commercial materials are not sufficient to guarantee an economically feasible separation for Carbon Capture and Storage applications.

In this work the current research targets in terms of optimal membrane characteristics for carbon capture applications are considered and a detailed process analysis is carried out. In order to predict the performances of a membrane separation unit, mathematical models are developed. These are then integrated into a commercially available simulation software where complete process designs are carried out.

In conclusion of this thesis, a rigorous economic analysis is presented to evaluate the effect of the capture unit on the overall power plant performances over its entire life. As a result of this feasibility evaluation, optimal material and process characteristics are identified and promising perspectives for membrane gas separation applied to Carbon Capture and Storage applications are shown.

Abstract

This thesis investigates membrane gas separation and its application to post-combustion carbon capture from coal-fired power plants as alternative to the conventional amine absorption technology.

The attention is initially focused on membrane module modelling, with the aim of obtaining more detailed predictions of the behaviour of the separation though spiral-wound and hollow-fibre modules. Both one- and bi-dimensional models are implemented, compared and tested for different separations. Module geometry is investigated as well as the effect on the performances due to possible fabrication defects.

A key part of the work involves the integration of the customised models into UniSim® Design, the Honeywell process simulator. Thanks to the developed interface, multi-stage process designs are developed, compared with the available literature and linked to a rigorous economic analysis. In particular, a long-term indicator such as the Levelised Cost Of Electricity (LCOE) is evaluated and parametric analyses are conducted with respect to both material and process parameters.

Table of contents

Table of figures

Table of tables

Chapter 1: Introduction

Greenhouse gases emissions are considered one of the main contributors to the global climate change [1]. Different scenarios in terms of increasing global temperatures have been predicted [2]: according to IPCC (Intergovernmental Panel on Climate Change), an increase of 1.5 - 2 °C in surface temperature could be expected by the end of the 21st century compared to 1900 levels [3]. CO_2 is considered one of the main contributors to GHG (greenhouse gases) emissions and it represents 77 % of the total anthropogenic emissions [4]. Considering the total CO_2 emitted, 40 % comes from industry (cement, iron and steel and chemicals are the main emitters) while around 30 % is from fossil fuel power plants [4, 5]. United Kingdom presents one of the strictest regulations in terms of reduction targets: according to the 2008 Climate Change Act [6] 20 % of CO_2 emissions needs to be cut by 2020 compared to 1990 levels. In order to meet the energy demand, combustion of fossil fuels will still play a key role in the next decades, despite the increasing effort on the development of renewables [7].

Coal is one of the most abundant fossil fuel sources and it currently meets approximately 23 % of the global primary energy demand [8]. In particular, electricity generation from coal almost doubled from 1990 to 2010 and its projected increase by 2020 is almost twice the one predicted for wind and solar photovoltaic [9]. For example, in China [10] the coal demand is expected to reach 3.9 to 4.3 billion tonnes by 2025.

In this scenario, CCS – Carbon Capture and Storage – is one of the main candidate solutions to reduce CO_2 emissions from fossil fuel power plants [11]. Research effort is currently focused on both engineering (capture and transport) and geological (storage) aspects [12].

In Figure 1.1 the IEA (International Energy Agency) Blue Map Scenario is reported [13]. According to this scenario, which is based on a 50 % reduction of the global

CO_2 emissions by 2050 compared to 2005 levels, CCS will be one of the main contributors accounting for 19 % emission reduction, in addition to nuclear, renewables, Combined Heat and Power (CHP) plants and energy efficiency improvements. This should enable the CO_2 concentration in the atmosphere to remain below 450 ppm.

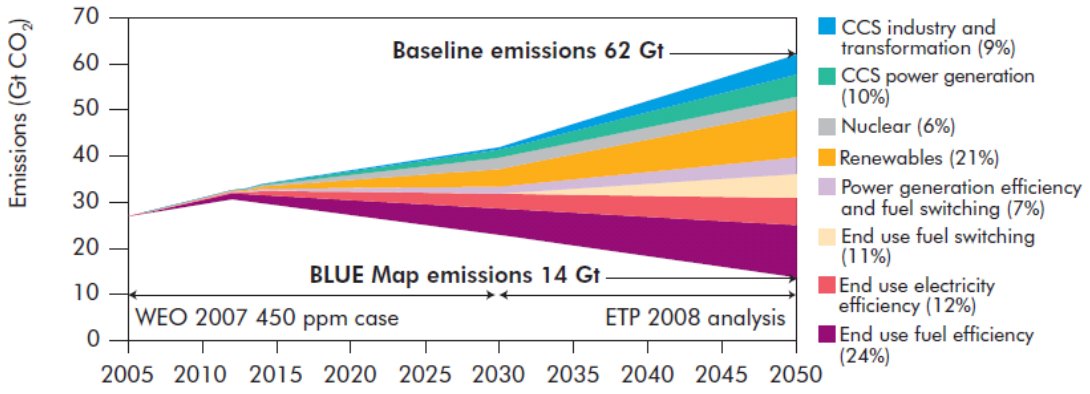

Figure 1.1: IEA *Blue Map* CO_2 emission Scenario [13].

Figure 1.2 shows the three ways of capturing CO_2 from a fossil fuel power plant (in addition to CCS from industrial sources):

- *Post-combustion*: CO_2 is separated directly from the flue gas emitted by the power plant. This process is characterised by relatively low temperature (323 K), atmospheric pressure and low CO_2 content (depending on the fuel, 5 – 15 % if air is fed to the combustor). The main advantage of this option is its possible retrofit to existing plants without further modifications. Chemical absorption using amines is the conventional solution, while adsorption, membranes and ammonia-based scrubbing are among the candidate technologies [7, 14].
- *Pre-combustion*: the fuel is converted to syngas (mainly CO, H_2, CO_2 and H_2O), it is sent to a water gas shift unit and CO_2 (approximately 30 % vol / vol) is then captured before sending the hydrogen as fuel to turbines. The CO_2–rich stream is at both high pressure (up to 8 MPa) and temperature (573 – 973 K). Example of a pre-combustion capture is physical absorption from

Integrated Gasification Combined Cycle Power Plants (IGCC) using Selexol [15]. Hydrogen sulphide and carbon dioxide are captured due to the high selectivity of the solvent with respect to both components.

- *Oxyfuel*: before feeding the oxidant stream to the boiler, O_2/N_2 separation is performed, so that a mixture of CO_2 and H_2O is produced from combustion. Carbon dioxide can then be easily separated from water via condensation. However, an Air Separation Unit (ASU) needs to be installed in order to achieve the required oxygen concentration, generally higher than 95%. Before being fed to the boiler, the O_2-rich stream is mixed with recycled flue gas in order to maintain conditions similar to an air-fired combustion (to reach an Oxygen content of 25 - 30 % vol / vol), since combustion with almost pure Oxygen would not be tolerated by commercial boiler materials [14, 16]. In order to reduce the drop in efficiency - currently in the range 8 - 12 % for oxy-fuel coal-fired systems - different solutions are considered, as the adoption of pressurised combustion cycles which would guarantee an improved heating value of the fuel as well as improved combustion efficiencies [16].

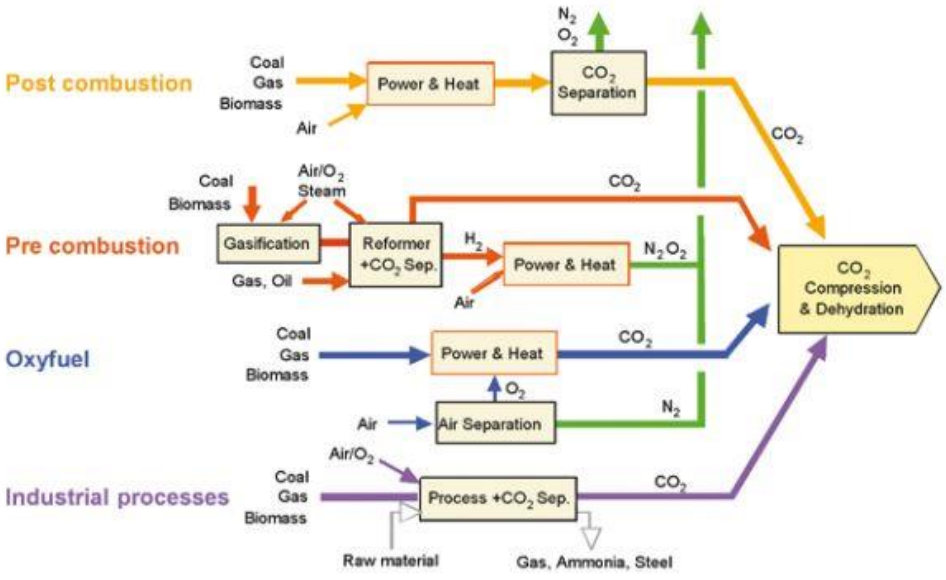

Figure 1.2: Carbon capture solutions from fossil fuel plants and industrial processes [17].

The state-of-the-art post-combustion carbon capture technology is represented by amine absorption: the CO_2 in the flue gas is absorbed by a solvent in the first column and the CO_2-rich solvent is then regenerated in the second one, as shown in Figure 1.3. The drawback of this separation is represented by the energy penalty due to the reboiler duty in the regeneration column and energy consumptions lower than 400 kWh_e/t_{CO_2} are reported as achievable [18-20]. New solvents are currently under investigation, as enzyme-catalysed solvent and concentrated piperazine which are developed within the US DOE-NETL (Department Of Energy-National Energy Technology Laboratory) funded projects [21]. Research effort is also focused on improvement of heat integration and new process configurations [20, 21] in order to reduce energy consumptions.

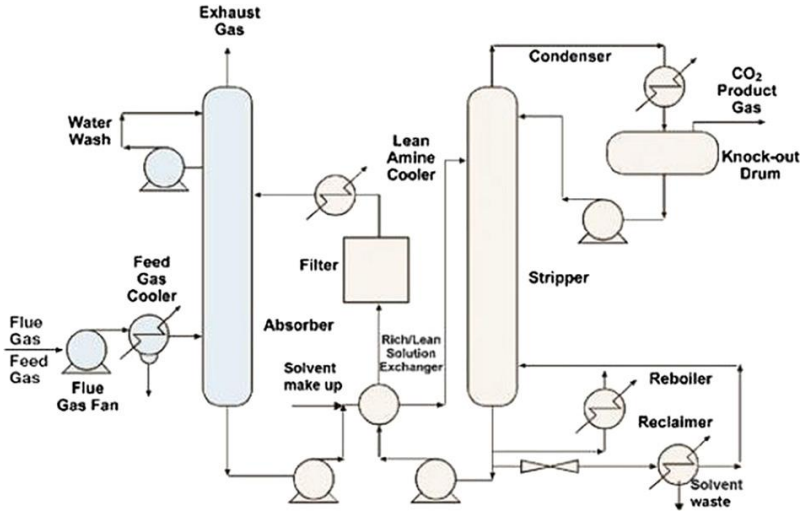

Figure 1.3: Conventional amine system [22].

This thesis focuses on membrane gas separation and its application to post-combustion carbon capture from coal-fired power plants [7]. Membrane technology is already applied to industrial gas and liquid separations but it is not commercial for carbon capture applications. It is a modular and flexible solution, no solvents are needed and the separation is carried out through the selective membrane film. A schematic representation of the plant with the capture unit is presented in Figure 1.4, where a CO_2-selective membrane unit is placed after FGD (Flue Gas Desulphurisation).

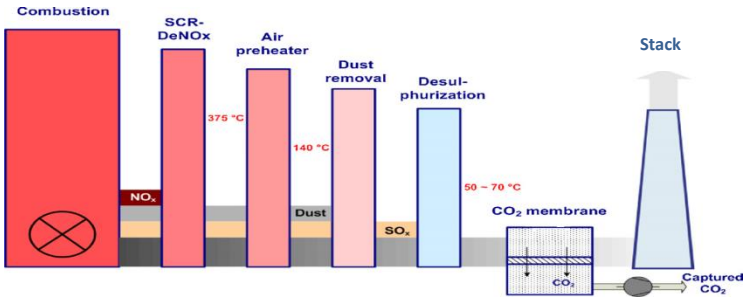

Figure 1.4: Typical design of a post-combustion capture system with membranes [23].

In order to carry out CCS feasibility studies, detailed process designs are required, linked to rigorous economic evaluations. In this work process simulations will be combined with a detailed economic evaluation but also with sensitivity analyses to evaluate the key contributions. Therefore, material, process and cost assumptions will be carefully discussed.

Particular attention will also be focused on the modelling aspect of the separation, in order to achieve a detailed prediction of the performance of the modules. This is an essential aspect due to the rigorous targets which need to be addressed for CCS applications, where a CO_2 recovery of 90 % and a purity above 95 % are required [14, 24]. Therefore, accurate models are needed to validate the feasibility of membrane technology to post-combustion carbon capture.

A significant part of this PhD Project has been focused on the customisation of a commercially available process simulator, Honeywell UniSim® Design. Since a membrane unit operation is not available in the simulation environment, a new simulation tool has been developed and the communication between the in-house software and UniSim® has been set up. This innovative customization has been awarded as winner of the *Honeywell UniSim® Design Challenge for Europe, Middle-East and Africa (EMEA)* and the work was presented at the *EMEA Honeywell Users Group* conference in Istanbul, November 2012 [25].

The Chapters are organised as follows:

- **Chapter 2**: a literature review on membrane separation applied to post-combustion carbon capture is presented. The different multi-stage designs from the literature are analysed with attention to material and process assumptions.
- **Chapter 3**: the modelling strategy is presented, starting from the available models in the literature. Mono- and bi-dimensional approaches for modelling the separation through spiral-wound and hollow-fibre modules are analysed. A statistical approach to account for module defects is also introduced.
- **Chapter 4**: the results from single-stage simulations for carbon capture are presented and the optimal flow patterns are identified. The performances of a single module are analysed and natural gas separation is simulated to investigate non-ideal and non-isothermal effects.
- **Chapter 5**: multi-stage designs are presented and compared with the available literature. Process performances are evaluated in terms of energy consumption and membrane area. A parametric analysis is also conducted.
- **Chapter 6**: the economic analysis in terms of *Levelised Cost Of Electricity* (LCOE) is presented. A sensitivity analysis with respect to key membrane and process parameters is carried out.
- **Chapter 7**: the conclusions of this thesis are given.

Chapter 2: Literature and background

In this Chapter an introduction on membrane separation is given and the main targets for CCS applications are introduced before focusing on a literature review on membranes applied to post-combustion carbon capture.

2.1 Introduction on membrane separation

In Figure 2.1 a schematic representation of the separation through a membrane is shown. The ability of a gas to permeate through a film is defined as *Permeability*, generally measured in Barrer [1 Barrer = 10^{-10} cm^3(STP)/(cm·s·cmHg) = $3.35 \cdot 10^{-16}$ mol/(m·s·Pa)]. For dense polymeric materials, permeability is represented by the product of solubility and diffusivity according to the solution-diffusion theory [26]. In the case of porous inorganic materials, the separation through the membrane can be governed by different mechanisms, such as surface, Knudsen diffusion, viscous flow or molecular sieving effect according to the diameter of the molecule and the pores. Gas separation using membranes is mainly dominated by polymeric materials due to their lower cost and ease of fabrication compared to inorganic membranes. Examples of commercial polymers are Cellulose Acetate, Polyimide and Polysulfone which are widely used for industrial separations [26-29].

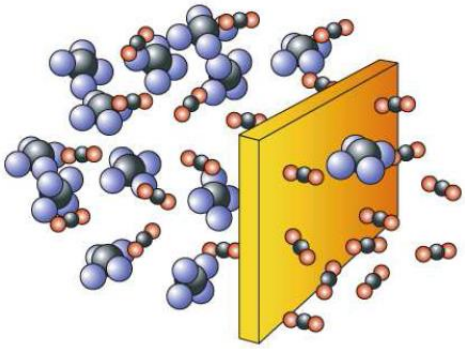

Figure 2.1: Schematic representation of the separation through a membrane [30].

The membrane *Selectivity* represents the ability of a material to separate one component over the other and it is defined as the ratio between the permeabilities of the two species. In the case of process simulations, a parameter generally used is *Permeance*, defined as the ratio between permeability and membrane thickness. It is commonly measured in GPU [*Gas Permeation Unit*, 1 GPU = 10^{-6} $cm^3(STP)/(cm^2 \cdot s \cdot cmHg) = 3.35 \cdot 10^{-10}$ $mol/(m^2 \cdot s \cdot Pa)$]. Since Barrer and GPU are the most common units for, respectively, permeability and permeance, they will be used throughout the presented thesis. SI units will be used for the other variables and, when required in the calculation, permeance and permeability will be converted to SI units as well.

A membrane module is a device where an amount of membrane area is assembled according to a certain configuration (flat sheet, tubular, hollow-fibre). A schematic module is shown in Figure 2.2. A stream is sent as *Feed* and separated into *Permeate* - components which permeate through the film according to their permeabilities - and *Retentate* streams.

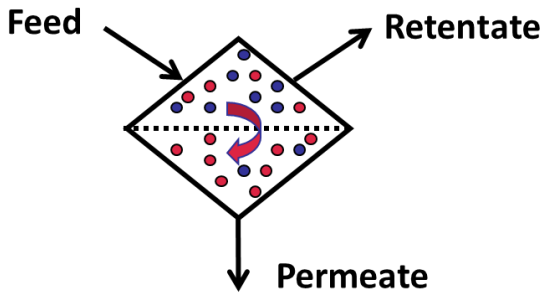

Figure 2.2: Scheme of a membrane module.

Common parameters in separation processes are *Purity* and *Recovery*. For post-combustion carbon capture applications the available membranes are CO_2-selective and CO_2 purity is calculated from the permeate composition while its recovery is the amount of CO_2 in the permeate side over its amount in the feed. Another parameter commonly adopted in membrane separations is the *Stage Cut*, defined as ratio between permeate and feed flow rate.

An important parameter in process designs is the *Pressure Ratio*, defined as the ratio between feed and permeate pressure. The driving force for the separation is the gradient in chemical potential across the membrane and it can be simplified as difference in partial pressure between the two sides [26]. Compression at the feed side and/or vacuum at the permeate side are adopted to increase the driving force. However, this clearly affects the energy consumption for the separation. Therefore, optimisations with respect to process conditions are generally required. The *Energy Consumption* can be expressed as its absolute value – power required by compressors/vacuum pumps – or relative to the amount of gas separated (e.g. kJ/mol or kWh/t).

A solution commonly adopted in membrane separations is a *Multi-stage Design*, where a *Stage* represents a defined area which separates the components under certain process conditions. In general, a number of modules are assembled in order to achieve the required area for the separation. Depending on the separation requirements (e.g. purity on retentate/permeate stream and/or overall recovery), one stage cannot be enough to meet the required specifications and, therefore, a multi-stage design is needed. Particular attention needs to be focused on the appropriate process design in order to optimise energy consumption and membrane area, the two criteria generally adopted to compare different configurations. Therefore, parameters as pressure ratios for the different stages, recycles and number of compressors need to be carefully investigated [31-33].

2.2 Post-combustion carbon capture and membranes

According to the US Department of Energy (DOE) [14] the targets for carbon capture are a CO_2 recovery of 90 % with a purity above 95 %. The CO_2 composition and the content of impurities in the final stream need to meet the requirements for transportation (e.g. avoid corrosion) and storage [34].

In Figure 2.3 an example of block-flow diagram for a pulverised coal-fired power plant with post-combustion carbon capture using amine technology is reported.

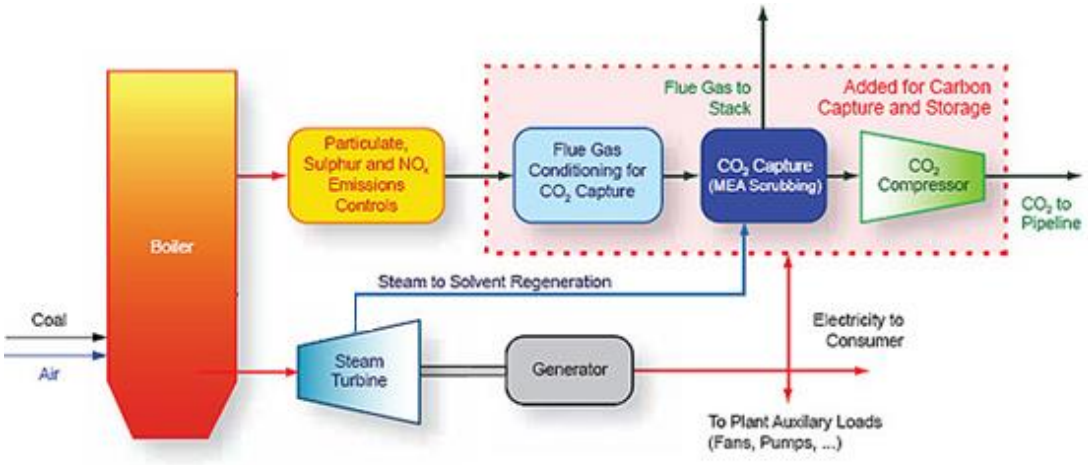

Figure 2.3: Block-flow diagram of a coal-fired power plant with CCS [35].

After Selective Catalytic Reaction (SCR) for nitrogen oxide removal, Electrostatic Precipitator (EP) and Flue Gas Desulphurisation (FGD), the flue gas is sent to the capture unit. In Table 2.1 the range of flue gas composition for a coal-fired power plant is reported. The CO_2 content is lower than 15 % (molar basis), the flue gas is humid and its temperature is above 323 K.

Component	Composition [% volumetric]
CO_2	12.6 - 15.0
N_2	71.4 - 74.0
O_2	3.0 - 4.3
H_2O	8.0 - 10.8
Others	0.9 - 1.0

Table 2.1: Flue gas composition range in coal-fired power plant [36].

Once the CO_2 separation is performed, the resulting CO_2-rich stream is compressed up to 15 MPa to reach the requirements for storage [24]. Therefore, a multi-stage compression system with intercooling is required after the capture unit. An example of a 4-stage compression train from Ahn et al. [20] is reported in Figure 2.4. Once

the CO_2 stream becomes a dense phase at 7.5 MPa, a pump is placed to reach the target pressure of 15.3 MPa.

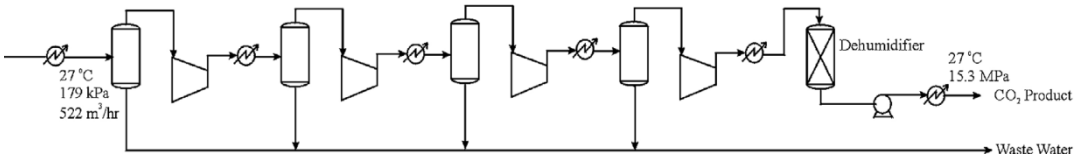

Figure 2.4: Compression system from Ahn et al. [20].

Several studies investigate the perspective of membrane technology in post-combustion carbon capture applications [18, 19, 23, 36-45]. The low CO_2 partial pressure in the flue gas and low selectivities of commercial CO_2-selective materials with respect to other components present in the stream are among the main challenges for this separation.

Research effort in the last decade [7, 46, 47] has been focusing on materials able to guarantee high CO_2 permeabilities while keeping high selectivities over the other components. This would ensure efficient separations by lowering both membrane areas and energy consumptions. Additionally, the stability of the material to contaminants (sulphur compounds, ashes and NO_x) and its resistance to humid conditions [48] are key requirements. Pilot plant tests on real flue gases are currently reported in order to evaluate stability and durability of the materials [49].

In Table 2.2 CO_2 permeability and CO_2/N_2 selectivity of some conventional and promising polymers are shown. With the aim of overcoming the so-called Robeson trade-off [50, 51] between permeability and selectivity reported in Figure 2.5 for CO_2/N_2, innovative research is currently focusing on co-polymers (e.g. PEBAX), thermally rearranged (TR) and mixed matrix membranes (MMMs). MMMs are a promising category of materials which consist in inorganic fillers incorporated into a polymeric disperse phase. The advantage of polymers is combined with the superior characteristics of inorganic materials.

Examples of commercial polymers:	CO_2 permeability [Barrer]	CO_2/N_2 selectivity [-]
CA (Cellulose Acetate) [46]	9	21
PI (Polyimide) [48]	0.5 - 600	16 - 39
PC (Polycarbonate) [48]	2 - 110	15 - 26
PSF (Polysulfone) [46]	7	30
PEO (Polyethylene oxide) [46]	7	60
PPO (Polypropylene oxide) [46]	59	34
PEBAX 1657 [48]	73	45
Examples of polymers under R&D:		
TR PBI *(polybenzimidazole)* [48]	1624	26
PIM 1 (Polymer of Intrinsic Microporosity) [52]	12600	25
PIM-PI 1 [48]	1100	23
PTMSP (Poly(1-trimethylsilyl-1-propyne) [48]	31600	11
Examples of Mixed Matrix Membranes:		
PEBAX + Silica [46]	306	81
PEI (Polyethylenimine) + Zeolite [46]	0.7	31
PI + Silica [46]	150	28

Table 2.2: CO_2 permeabilities and CO_2/N_2 selectivities from the literature of polymers and examples of Mixed Matrix Membranes.

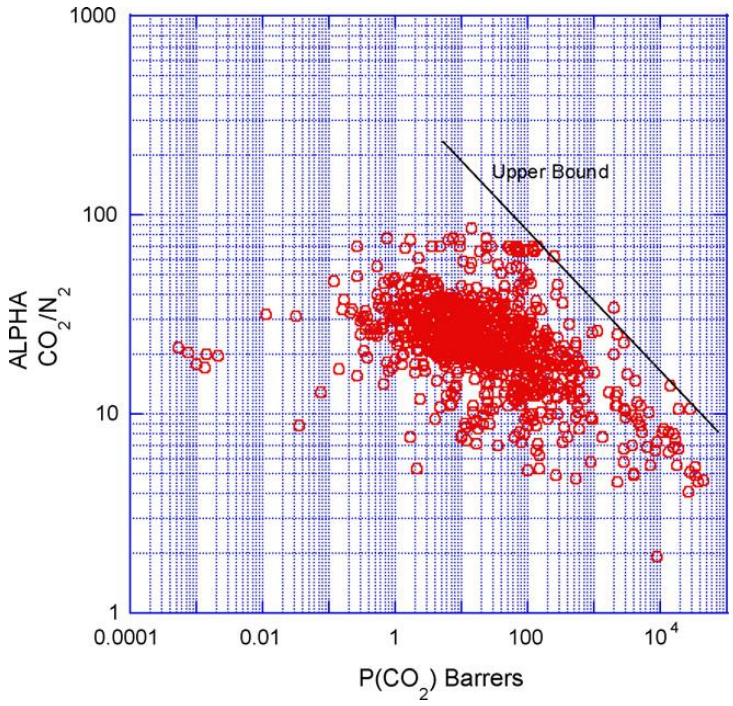

Figure 2.5: Robeson trade-off for CO_2/N_2 separation [51]. Legend: P(CO_2) = CO_2 permeability and ALPHA CO_2/N_2 = CO_2/N_2 selectivity.

The most commonly adopted parameter in process simulations is the CO_2 permeance, which already takes into account the thickness of the material. Thicknesses of commercial materials for gas separation range from 10^{-4} to 10^{-7} m and this is mainly dependent on the manufacturing process [26].

However, it is difficult to find in the literature a complete comparison among different materials in terms of achievable CO_2 permeance. In order to show the targets for carbon capture applications, a representative plot is reported in Figure 2.6, where the properties of Polaris^{TM} - the material produced by Membrane Technology and Research (MTR) Inc. [39, 53, 54] - are shown in comparison with the commercial materials in terms of CO_2 permeance and CO_2/N_2 selectivity. Polaris^{TM} is reported with an achievable thickness of 10^{-7} m [53] but no permeability data are available and, therefore, it cannot be directly compared with the data presented in Figure 2.5 and Table 2.2. The properties of Polaris^{TM} first generation (CO_2 permeance of 1000 GPU and CO_2/N_2 selectivity of 50) are considered as benchmark in the literature when polymeric membranes are used. Polaris^{TM} 2nd generation is currently tested at pilot plant scale and it has a CO_2 permeance of 2000 GPU (Figure 2.6).

The most recent developments in terms of carbon capture targets on a research level (Polaris^{TM} advanced in Figure 2.6) report a CO_2 permeance above 5000 GPU by keeping a CO_2/N_2 selectivity of 50 [54]. If the same thickness s assumed, a higher permeance – and therefore higher permeability – by keeping the same selectivity would also lead to a membrane able to overcome the experimental trade-off between permeability and selectivity (Figure 2.5).

The analysis presented in this work is based on optimal material characteristics, in line with the targets for Polaris^{TM} advanced. These will be carefully discussed in Chapter 5 and Chapter 6, where parametric analyses will be also carried out.

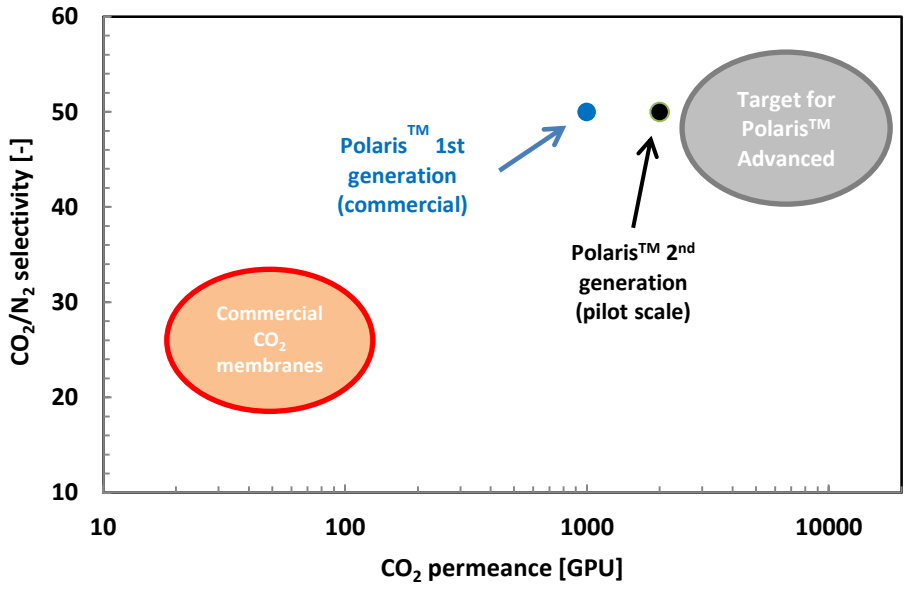

Figure 2.6: Targets for Polaris™ membranes in terms of CO_2 permeance and CO_2/N_2 selectivity (data taken from [55]).

2.1 Process design approaches

As already reported in the literature [23, 39, 48], a single-stage membrane unit cannot achieve the requirements for CCS since a trade-off is identified between CO_2 purity and recovery. Therefore, an efficient multi-stage design is essential for achieving competitive performances with the state-of-the-art amine absorption.

Dual-stage designs are generally adopted [39, 43, 44]. In Figure 2.7 the different process configurations proposed by Zhao et al. [45] are reported. In order to increase the driving force for the separation, feed compression and/or vacuum at the permeate side are required. A key element to consider is the number of compressors (and vacuum pumps) which are the main contributors to energy consumption [31-33].

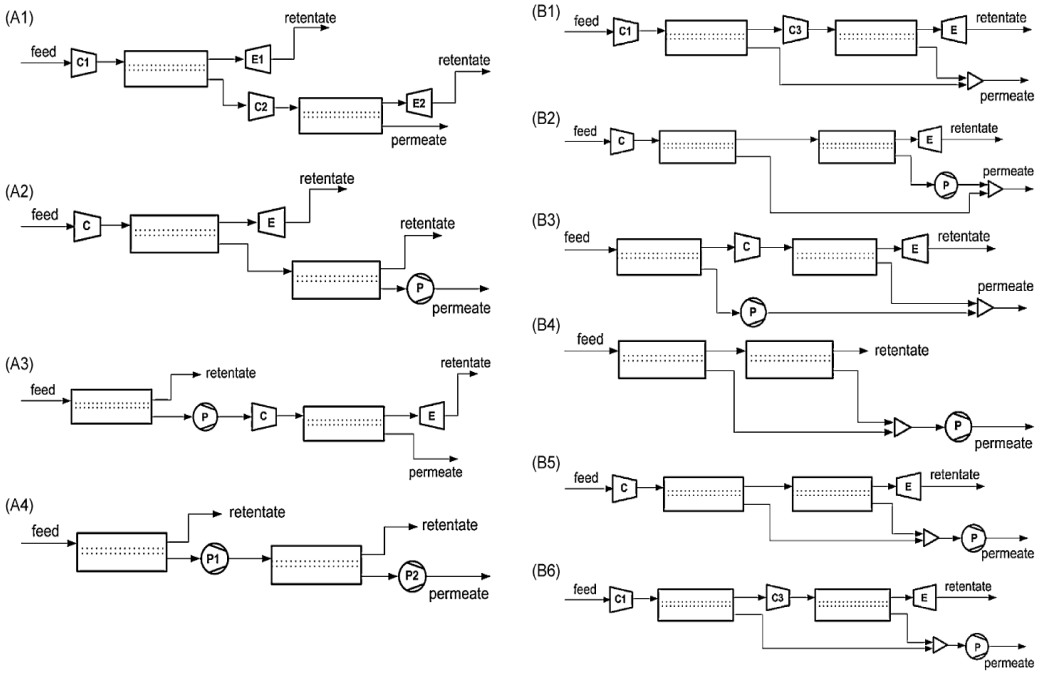

Figure 2.7: Dual-stage configuration from Zhao et al. [45].

Most of the available process simulations are based on data from polymers [36, 39, 41, 43-45]. A CO_2 permeance of 1000 GPU or higher is generally assumed and sensitivity analyses are conducted with respect to both permeance and selectivity. Membrane parameters are strictly related to the assumed process conditions and pressure ratio is one of the key parameters. Pressure ratios higher than 10 are generally used in the literature, despite the penalizing energy consumption which is related to this assumption. However, low values require specific membrane properties and this is related to the different optimal material characteristics which are identified in the literature. An example of a parametric analysis with respect to pressure ratio and CO_2/N_2 selectivity carried out by Huang et al. [56] is reported in Figure 2.8. In this study, a single-stage membrane unit is simulated assuming a bi-component feed 10 % CO_2/ 90 % N_2 (vol/vol) and a CO_2 permeance of 1000 GPU. The CO_2 retentate composition is fixed to 9.9 %. A trade-off is encountered between membrane area and permeate composition: for high CO_2/N_2 selectivities the increased CO_2 purity is associated to a higher membrane area. On the other hand, the optimal selectivity range is dependent on the assumed pressure ratio (θ in Figure

2.8), which is directly related to energy consumption. Both material and process assumptions should be carefully considered and this aspect will be discussed in the next paragraphs where the multi-stage approaches from the literature will be presented.

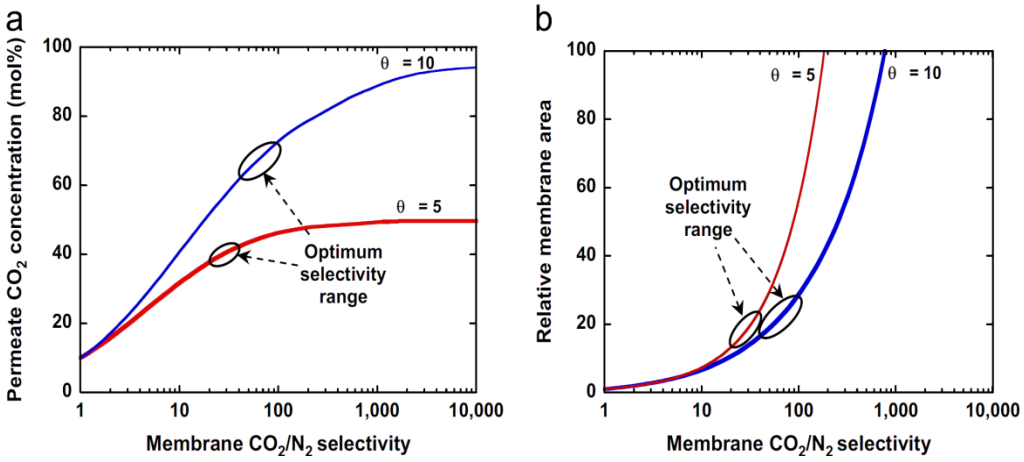

Figure 2.8: Parametric analysis with respect to pressure ratio and CO_2/N_2 selectivity. Single stage membrane unit with feed composition 10 % CO_2/90% N_2[56]. Legend: θ = pressure ratio.

In a recent publication from Low et al. [48] data from the most promising materials are included and their potential to carry out separations in humid conditions is investigated. The behaviour of a membrane in presence of water is in fact a key parameter. It is well-known that water may achieve high permeabilities in polymers but their stability is a key issue. It is also difficult to find permeability data in presence of water in the literature. For example, the available data on Polymers of Intrinsic Microprosity (PIMs) [57, 58] suggest permeabilities comparable to CO_2 or higher can be achieved. For the purpose of process simulations considering polymeric membranes, water is generally assumed at least as permeable as CO_2.

The inlet temperature to the membrane module is also an important parameter as the operating temperature is expected to affect membrane performance [26]. It should be also pointed out that the inlet temperature has an effect on the water content if a drying unit is not assumed [48]. Inlet temperature values between 298 K and 323 K are reported in the literature. This assumption is directly related to the heat exchanger

area required for the pre-treatment of the flue gas which is above 50°C at the exit of the FGD.

Process assumptions that directly influence energy consumption are compressor, expander and vacuum pump adiabatic efficiencies for the capture unit and the final compression system. In the literature values that range from 75 % to 90 % are reported, but an efficiency of 80 % [39] is generally assumed as a benchmark.

The membrane designs presented in the literature are based on steady-state simulations [23, 38, 39, 41, 43-45, 59]. It is assumed that the response of the membrane to a change in process conditions does not have a significant effect on the performances and, therefore, dynamic simulations are not generally carried out for membranes. In line with the available literature, the process designs presented in this thesis will be based on steady state simulations. However, since this work is mainly a feasibility study, the assumption of a fast response of the membrane unit to a change in process conditions is also verified for carbon capture applications. Preliminary single stage dynamic simulations are carried out to evaluate the behaviour of a membrane unit if fluctuations in process conditions take place. Such fluctuations are probable in future energy scenarios with increasing penetration of renewable energy and this will be analysed in Section 2.9.

An optimisation with respect to process and material parameters is required [39, 41, 43, 45, 46, 60-62] in order to reduce both membrane area and energy consumption. The results presented in the literature focusing on membrane technology appear promising in terms of carbon capture feasibility. Energy consumptions lower than 400 kWh_e/t_{CO_2} are reported as achievable [59] and capture costs lower than 30 $\$/t_{CO_2}$ are shown in different investigations (amines are in the range 40 - 50 $\$/t_{CO_2}$) [39, 45, 60]. In line with recent publications from different international and national organisations for amine technology [13, 63, 64], cost of electricity calculations have also been carried out for membranes [41, 44, 65]. Cost of electricity is a particularly useful parameter since it takes into account the electricity produced by the plant throughout its entire life as well as capital and operating costs. In particular, different

investigations [41, 43, 65] show that membranes can meet the target of a relative increase in Cost of Electricity lower than 35 %, as stated by US Department of Energy (DOE) guidelines [65]. However, it should be pointed out that the most promising results are shown for hypothetical material characteristics based on current research targets.

An example of possible improvement in capture cost by using membranes with increasing CO_2 permeance is reported in Figure 2.9. It can be seen that by having membrane characteristics similar to the targets for Polaris™ advanced (Figure 2.6), a significant improvement in terms of economic performances can be achieved. A detailed insight into economic analyses will be given in Chapter 6 where the effect of membrane permeance will be taken into account.

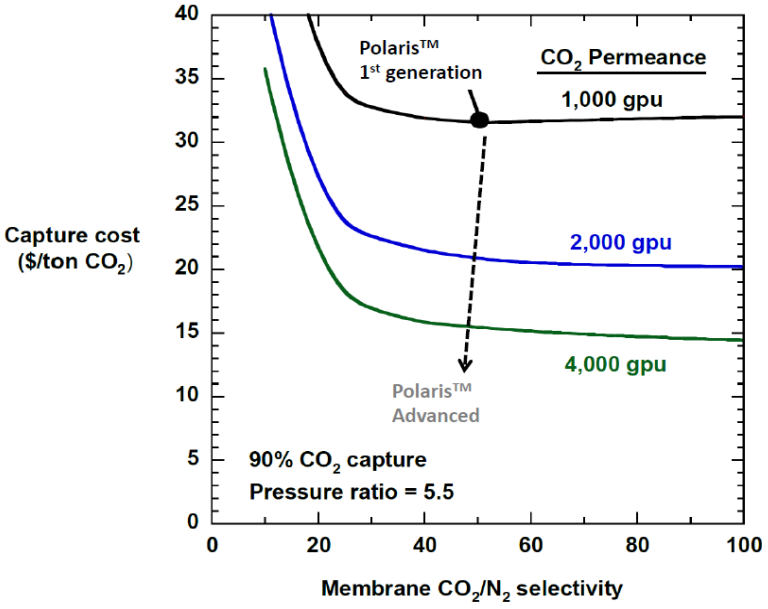

Figure 2.9: Capture cost with respect to membrane permeance and CO_2/N_2 selectivity [55].

2.2 Multi-stage designs from the literature

In this section an overview of the multi-stage designs from the literature is presented. They are classified according to the following criteria:

- ***Retrofit***: designs including membrane stages treating directly the flue gas from the power plant;

- ***Hybrid***: designs which include a refrigeration unit performing part of the separation;

- ***Selective exhaust gas recycling***: designs which include the recycle of part of the CO_2 to the boiler.

The membrane units used in process simulations are generally based on plug-flow models in counter-current flow pattern which will be discussed in Chapter 3. Cross-flow one-dimensional models are also adopted [39, 41, 43] to model the separation through spiral-wound permeators.

If not differently stated, CO_2 recovery is fixed to 90%, its purity above 95% and the final compression part is included for all the results reported herein.

2.3 Retrofit configurations

Different solutions are available in the literature based on multi-stage membrane capture [38, 44, 45, 59, 60] followed by compression of the high-purity CO_2 stream. These are mainly dual-stage designs.

Zhao et al. [23, 45] present a single and dual-stage analysis to show the potential of membrane separation for flue gas treatment. Non-dispersed plug-flow stages are simulated and the reference membrane material is a polyimide with a CO_2/N_2 selectivity of 40 and a CO_2 permeance set to 365 GPU. Parametric studies with respect to membrane permeability, selectivity, pressure ratio and inlet CO_2 concentration are presented and feed compression is identified as less energy demanding. In their dual-stage design [45] particular attention is focused on the optimal process configuration, as shown in Figure 2.7 where different schemes are reported. Different recoveries in the range 50 - 90 % are simulated and a rigorous

analysis based on capture cost evaluation is linked to the process design. The investigation focuses on the design in Figure 2.10, which is variant A3 in Figure 2.7 with recycle of the retentate of the second stage to inlet stage 1. However, this option is identified as optimal in terms of both membrane area and energy consumption if the recovery is fixed to 70 %. It is shown that a membrane with a CO_2 permeance of 1825 GPU and a CO_2/N_2 selectivity of 40 is promising for carbon capture applications. In fact, by fixing the inlet pressure in stage 2 to 4 bar feed side and a vacuum of 100 mbar at permeate side, a membrane area of approximately $1.5x10^6$ m^2 and an energy consumption of 171 kWh_e/t_{CO_2} can be obtained.

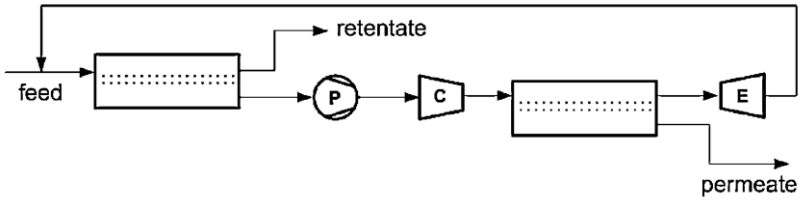

Figure 2.10: Proposed configuration by Zhao et al.[45].

Ho et al. [38] present a dual-stage design with PPO (*PolyPhenylene Oxide*) with a CO_2 permeability of 70 Barrer, a CO_2/N_2 selectivity of 20 and a thickness of 125 μm. The schematic flowsheet is reported in Figure 2.11, where a dehydration unit is simulated before the cross-flow membranes stages and CO_2 recovery is fixed between 85 and 90%. Vacuum on the permeate side is identified as preferable to feed compression and a sensitivity analysis with respect to material properties and membrane price is also presented. A CO_2 permeability of at least 500 Barrer and CO_2/N_2 selectivity in the range 40 - 60 are identified as requirements for achieving a competitive separation. A dual-stage design with cross-flow stages analogous to Figure 2.10 is also proposed by Zhai et al. [43], based on a bi-component feed CO_2/N_2, assuming a CO_2 permeance of 1000 GPU and CO_2/N_2 selectivity of 50.

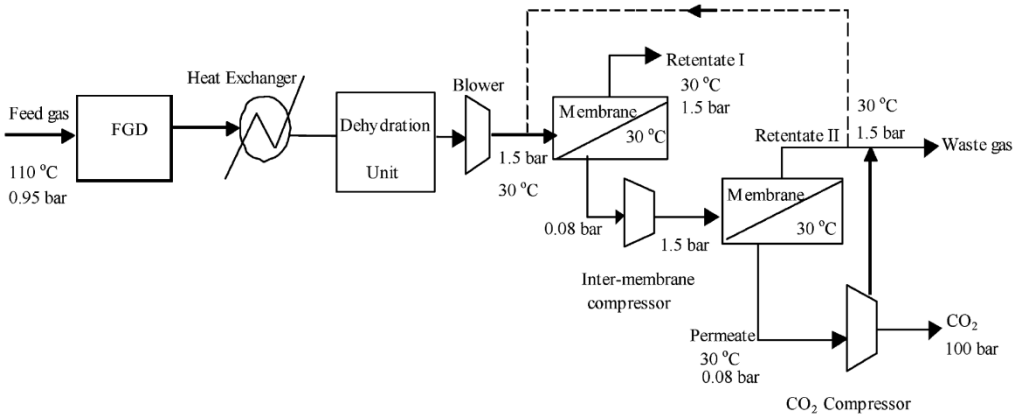

Figure 2.11: Dual-stage design from Ho et al.[38].

Shao et al. [41] develop a dual-stage design based on cross-flow stages based on a membrane with a CO_2 permeance of 1000 GPU and a CO_2/N_2 selectivity of 50. Optimal conditions in terms of minimal power demand are identified for a feed pressure of 0.24 Mpa and a pressure ratio of 17. It is also shown that a CO_2/N_2 selectivity of 200 with a membrane permeance of 1000 GPU may lead to a decrease of the capital cost due to the reduced energy consumption, despite an increase in membrane area is encountered ($1.06x10^6$ to $1.39x10^6$ m^2).

Zhang et al. [44] present a single and dual-stage design linked to a detailed energy and exergy [66] analysis in comparison with MEA (Mono-Ethanol Amine) and with respect to recovery (range 50 - 90 %). The base membrane presents CO_2 permeances in the range 365 - 2920 GPU and CO_2/N_2 selectivities of 50 - 220. As a result of this analysis, CO_2/N_2 selectivity in the range 70 - 90 is identified as optimal for carbon capture applications.

A comparison with MEA is also proposed by Hasan et al. [36] including a dehydration unit before the membrane system with triethylene glycol (TEG) absorption. After being dehydrated and compressed to the desired pressure, the flue gas is sent to a multi-stage design followed by the compression system. The membrane considered has a CO_2 permeance of 730 GPU, CO_2/N_2 selectivity of 40, CO_2/O_2 selectivity of 40 and CO_2/H_2O selectivity of 2. A detailed economic analysis

is presented for different feed compositions and membrane separation is competitive with MEA absorption for CO_2 composition greater than 30 %.

Alsehri et al. [60] propose an optimisation study based on a counter-current/sweep design with pressure drops on permeate side (bore side of the assumed hollow-fibre module): CO_2 permeances in the range 500 - 2000 GPU and CO_2/N_2 selectivities in the range 20 - 200 are simulated and an optimisation routine using the capture cost formulation from Merkel et al. [39] is set up. For example, a CO_2/N_2 selectivity of 144 is identified as optimal if a membrane with a CO_2 permeance of 1000 GPU is adopted.

A facilitated transport membrane is assumed in the study of Hussain and Hägg [59] who present a dual stage design with counter-current stages simulated as non-dispersed plug-flow. The material has a CO_2 permeance of 405 GPU, CO_2/N_2 selectivity of 200, CO_2/O_2 selectivity of 50 and CO_2/H_2O selectivity of ~10^8. Due to the high water selectivity, vapour is used as sweep increasing the driving force for the separation on the permeate side: this strategy is favourable for pressure ratios in the range 40 - 80 compared to permeate sweep. A membrane area of $1.5x10^6$ m^2 and specific energy consumption lower than 350 kWh_e/t_{CO_2} are achieved by keeping both recovery and purity at 90 %.

Metallic membranes have also been considered for post-combustion applications and a feasibility study is proposed by Yuan et al. [67]. The concept of using a N_2-selective membrane stage as a CO_2-enricher appears as a promising application and one of the proposed designs is shown in Figure 2.12. It is assumed that only N_2 permeates through the metallic material with a permeance of 1000 GPU. A CO_2 permeance of 1000 GPU and a CO_2/N_2 selectivity of 50 are assumed for the CO_2-selective stage. However, energy consumption due to the high operating temperature of metallic membranes (873 – 1173 K) is an important process limitation. Higher N_2 permeances are also needed and the effect on the membrane of other components in the flue gas needs to be investigated.

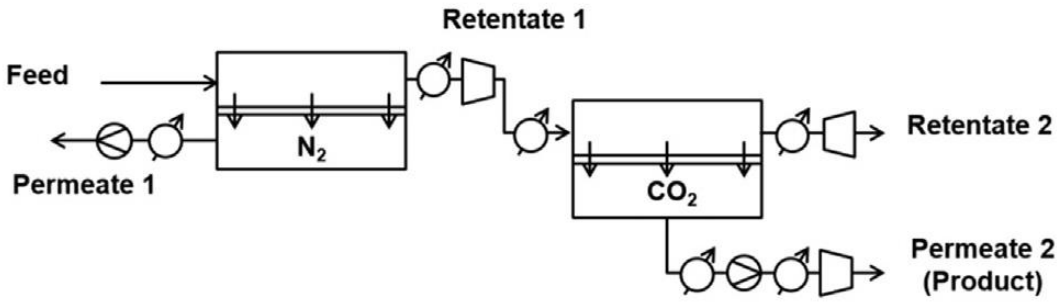

Figure 2.12: Proposed design by Yuan et al. [67] with a combination of a N_2-selective and a CO_2-selective stage.

2.4 Hybrid configurations

In addition to designs presenting only membrane stages and compression system, different studies show *hybrid* solutions where an additional separation process is added in order to increase the efficiency of the design. The configurations considered in this thesis include a refrigeration stage to increase the final CO_2 purity by keeping lower energy consumptions.

Merkel et al. from MTR Inc. (Membrane Technology Research) present a hybrid multi-stage design based on cross-flow stages reported in Figure 2.13 [39, 55]: the permeate stream from stage 1 (with a CO_2 purity of 80 %) is sent to a refrigeration stage which cools down the CO_2–rich stream to 273 K. This configuration can achieve higher CO_2 purities improving the energy efficiency of the capture process. Two stages are simulated before the compression/refrigeration system and an additional stage is located after the refrigeration. The pressure ratio is fixed to 10 (0.2 Mpa bar feed side and 20 kPa at permeate side) and vacuum at the permeate side is identified as preferred to feed compression. For CO_2 permeances above 4000 GPU a pressure ratio of 5 with a blower at feed side has the potential of reducing the energy penalty; for lower permeances the significant increase in membrane area affects the capital cost contribution. The membrane is Polaris^{TM}, same permeances for N_2 and

O_2 are assumed and a selectivity of 0.7 for CO_2/H_2O is reported [39, 65]. An energy consumption of 315 kWh_e/t_{CO_2} is achieved with a membrane area of $3x10^6$ m^2.

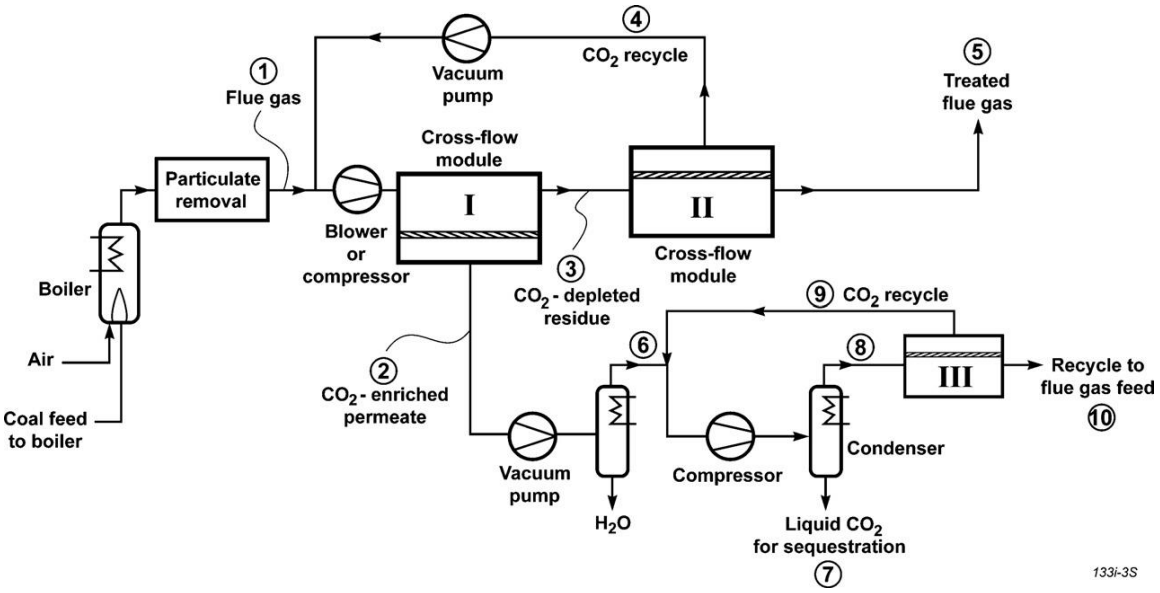

Figure 2.13: Multi-stage *hybrid* design from MTR Inc.[39].

An alternative hybrid design proposed by Air Liquide in a project funded by NETL [68, 69] is shown in Figure 2.14. The main idea of the process is to capture CO_2 in a membrane unit operating in sub-ambient temperature (243 to 233 K): by decreasing the inlet temperature the main outcome is an increased CO_2/N_2 selectivity (>90) by keeping similar CO_2 permeance compared to ambient temperature performances. Recently published results [70] show energy consumptions of 216 - 232 kWh_e/t_{CO_2}.

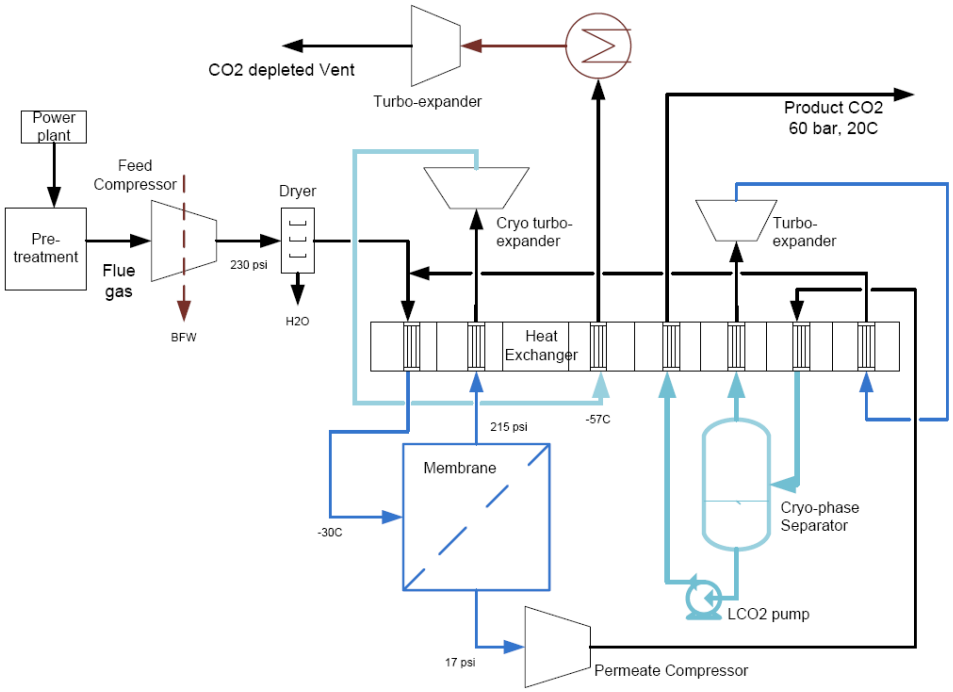

Figure 2.14: Hybrid process from Air Liquide [70].

2.5 Selective exhaust gas recycling configurations

Configurations which involve the recycle of part of the CO_2 to the boiler with the combustion air are now considered. This solution was initially proposed and patented by Merkel et al. [39, 55, 71] and it involves the use of atmospheric combustion air as sweep in a counter-current stage, as shown in Figure 2.15. A stream containing CO_2 is sent as feed to a counter-current stage with air as sweep usually after a first stage where part of it is recovered: the CO_2 permeates and the resulting permeate stream is sent as feed to the boiler. The main benefit of this design is the achievement of higher CO_2 concentrations in the flue gas, making the separation more efficient.

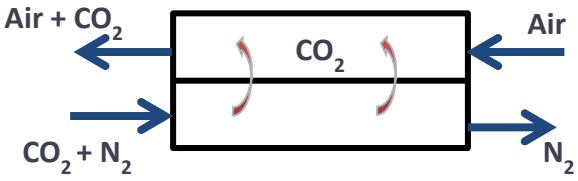

Figure 2.15: Counter-current stage with air as sweep.

The three-stage design proposed by MTR Inc. [39] is reported in Figure 2.16: the resulting stream to the boiler from stage 2 contains 8.7 % of CO_2 and 17 - 18 % of Oxygen. Compared to the hybrid solution assuming the same membrane characteristics, this process configuration results in a reduction of both membrane area ($1.3x10^6$ m^2) and energy consumption (234 kWh_e/t_{CO_2}). Recently published data using the same design [65] consider a CO_2 permeance of 3500 GPU, a CO_2/N_2 selectivity of 35 and pressure drops in the atmospheric counter-current stage (7 kPa on both sides), resulting in a membrane area of $1.5x10^6$ m^2.

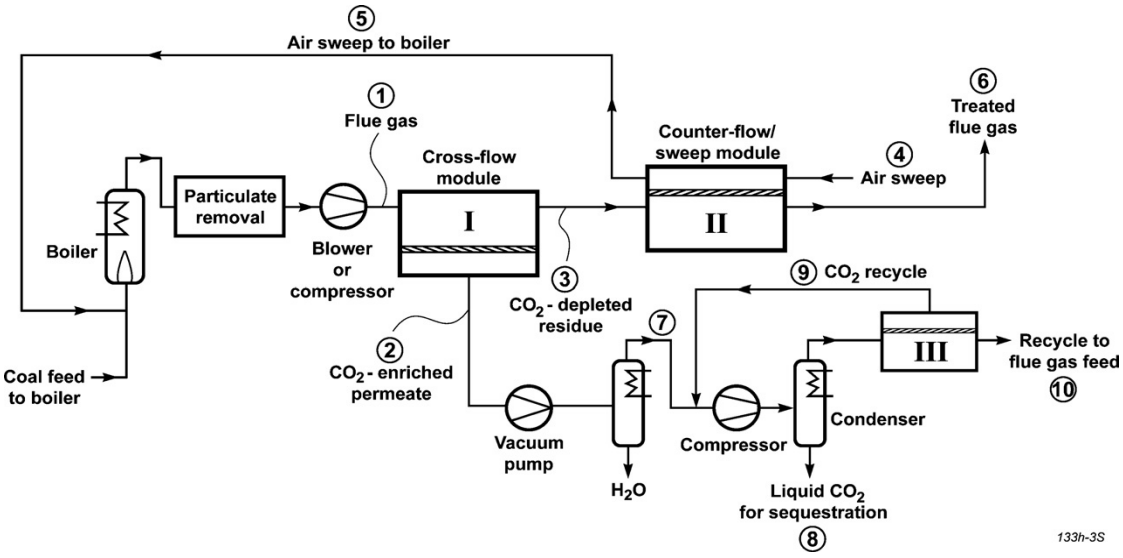

Figure 2.16: Selective exhaust gas recycling design from MTR Inc. [39]. Air (stream 4) is sent as sweep to stage II and the resulting CO_2-enriched permeate (stream 5) is sent as feed to the boiler.

RTI international [70] in a DOE/NETL funded project presents a solution based on a three-stage design reported in Figure 2.17. The material adopted for the simulation is

a membrane with a permeance of 500 GPU and a CO_2/N_2 selectivity of 35 that is the target for Vinylidene Fluoride-based material (PVDF) [72]. As a result of this design, a membrane area of $3.4x10^6$ m^2 and an energy requirement of 357 kWh_e/t_{CO_2} are achieved.

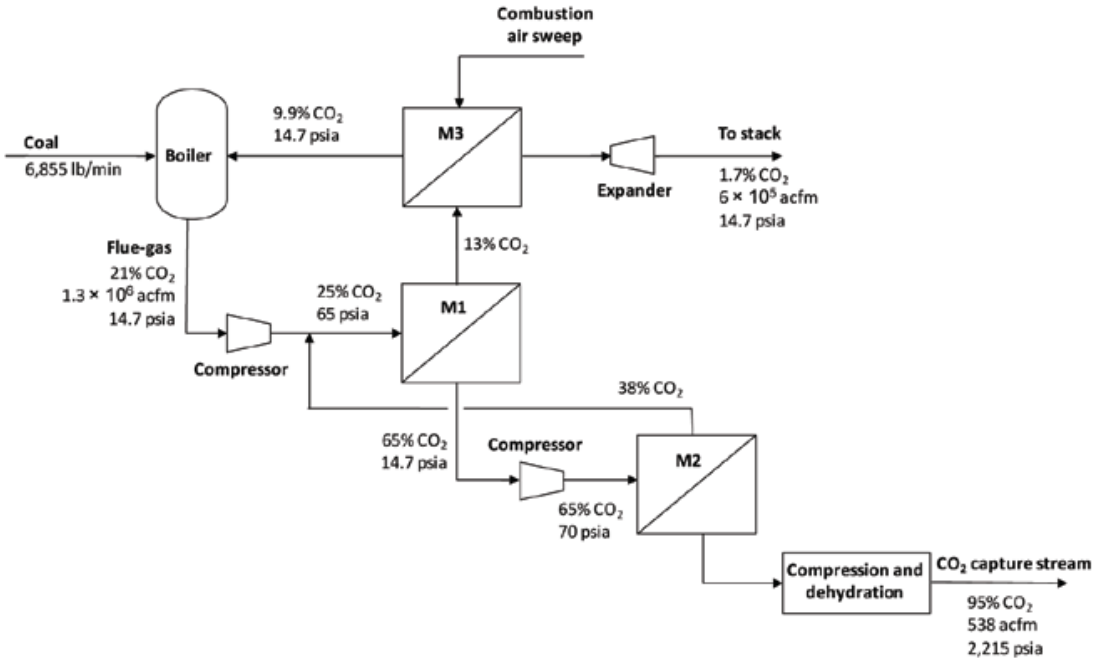

Figure 2.17: Selective exhaust gas recycling design from RTI International [70].

Ramasurbramanian et al. [61] report a detailed dual-stage selective exhaust gas recycling design: the membrane scheme (before compression) is analogous to the one proposed by Merkel et al. [39]. A CO_2 permeance of 3000 GPU is identified as optimal, and, despite the increase in membrane area with CO_2/N_2 selectivity observed, a minimum in energy consumption is identified for selectivities of 150.

Zhai et al. [43] also present a three-stage cross-flow design reported in Figure 2.18. The feed-side pressure is 0.2 MPa keeping vacuum on the permeate side. The membrane area decreases for high pressure ratios but this is associated with higher energy consumption. However, the performances are identified as more dependent on the feed-side pressure, due to the increased energy consumption for feed compression.

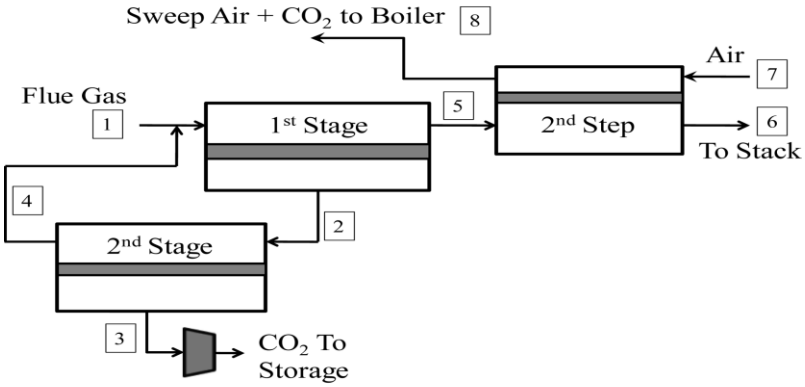

Figure 2.18: Three-stage design from Zhai et al.[43].

One of the main drawbacks of these configurations is the dilution and possible back-permeation of Oxygen in the counter-current/sweep stage with combustion air. This may lead to different conditions in the boiler, therefore penalising its performances. A recent publication from Scholes et al. [73] includes an additional membrane air separation stage based on a cross-flow Air Products PRISM membrane [74]. Vacuum is kept at the permeate side of an Oxygen-selective membrane stage where an Oxygen purity of 50 % is reached at the permeate side before being diluted with a bypass from the feed and the CO_2 molar fraction to the burner is kept to 9 %. The CO_2-selective membrane has a permeance of 1000 GPU, CO_2/N_2 and CO_2/O_2 selectivity of 50 and CO_2/H_2O selectivity of 0.1. One of the proposed designs is showed in Figure 2.19: the downstream part of stage 1 is analogous to Merkel et al. [39] with compression/refrigeration and additional membrane stage 3. The possibility of removing this stage is also investigated. Despite the additional membrane stage, FGD and SCR (both units are not required by Australian regulations), competitive economic results are achieved as discussed Chapter 6.

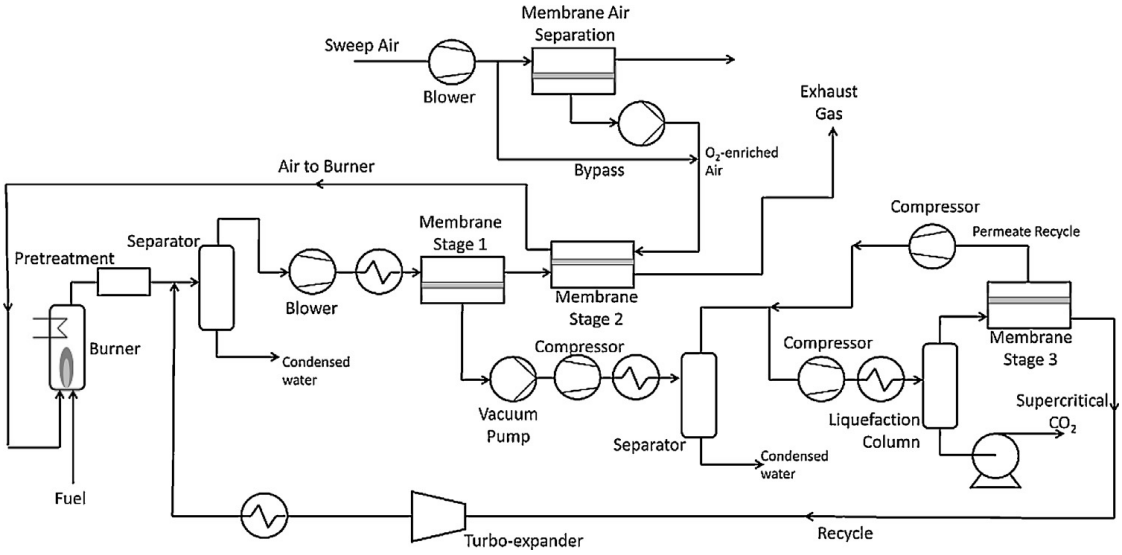

Figure 2.19: Selective exhaust gas recycling solution from Scholes et al. [73].

2.6 Pilot projects

In order to make CCS commercial in the next decades, several organisations set roadmaps in terms of pilot plant projects. In 2008 the leaders of G8 agreed that large-scale deployment of CCS should start by 2020 [75]. Additionally, according to IEA, 100 demonstrations are needed by 2020 [76].

The promising results for post-combustion CO_2 capture using membranes achieved in terms of both material performances and process simulations led to pilot-scale projects. MTR Inc. is currently carrying out pilot plant tests on real flue gas in a project funded by US NETL (National Energy Technology Laboratory) [65]. In 2010 a three-month field test at APS Cholla coal-fired power plant in New Mexico was carried out by four 8-inch diameter Polaris^{TM} (20 - 100 m^2 each [55]) cross-flow and counter-current/sweep modules designed to treat 7,000 m^3/day (0.25 MMscfd) of flue gas and to capture one tonne CO_2/day. The system showed stable performance for the 45-day test: fouling did not appear to be a problem and no significant reductions in CO_2 permeance and CO_2/N_2 selectivity were encountered, giving promising results for future tests. In 2012 continuous operation of the skid was

initiated: during the first 1000 hours of operation a CO_2 recovery of 65 % was achieved and modules were then added in order to achieve 85 % recovery. However, problems were encountered in the rotating equipment (compressors and vacuum pumps) due to the corrosive operating environment. Formation of sulphate salts on the surface of membrane was also encountered causing loss of CO_2 flux [53]. The next stage of the research includes additional operation of the 0.05 MWe equivalent gas flow and construction of a larger-scale system able to treat 1 MWe equivalent of flue gas for a six-month test which is currently carried out at the National Carbon Capture Center (NCCC) [77]. In order to minimise permeate side pressure drops which reach a value of 4 psi with the current spiral-wound modules form MTR Inc., a new module design is currently being tested in order to achieve a tolerable value of 7 kPa [54]. In Figure 2.20 a skid containing 28 modules from this pilot project is reported: approximately 400 of these skids are required considering a realistic value of 100 m^2 per module [55] to achieve the membrane area required for the selective exhaust gas recycling design reported in Figure 2.16.

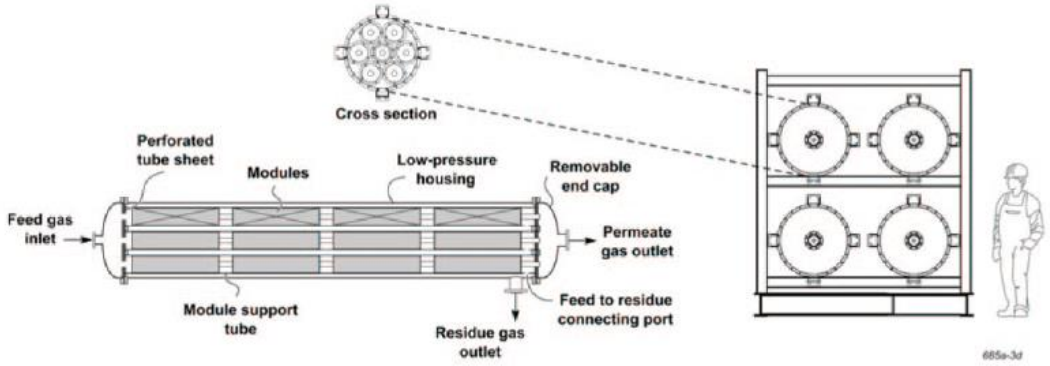

Figure 2.20: Example of membrane skid from MTR Inc. pilot plant project [78].

Studies on boiler performances resulting from the selective exhaust gas recycling configuration are also reported within the DOE-NETL project from MTR Inc. [53, 54]. Stable and attached flames but less luminous than conventional combustion conditions have been obtained if CO_2-enriched air is adopted (16 - 18 % O_2). A reduction in NO_x emissions is also expected (-30 %) and it has been calculated that with 18 % Oxygen a net reduction of 0.75 % in efficiency can be expected.

Other pilot plant tests are reported within the nanoGLOWA project, a joint 5-year partnership concluded at the end of 2011 among 27 organisations from 14 countries funded by the European Commission under the 6th Framework Programme [79]. In Figure 2.21 the targets of the project are reported. The aim of this project was to investigate different materials (polymers, ceramic and carbon) to be assembled in fibres, spiral, tubular and flat sheet module configurations. According to the available information, a 6-month test campaign with 1.5 m^2 of (flat sheet) membranes has been carried out at EDP Sines coal-fired power plant on 20 - 30 m^3/h of flue gas. A pilot test at EON Sholven power plant was also reported using curtain-and-tube membrane modules. Polymers gave the best results among the different materials [80]: tests on s-PEEK (sulphonated poly(ether etherketone)), PEO (Poly Ethylene Oxide) and PPO (Poly Prophylene Oxide) are reported [34]. Polymers gave the best results particularly in terms of CO_2/N_2 selectivities: values of 100 are reported [80].

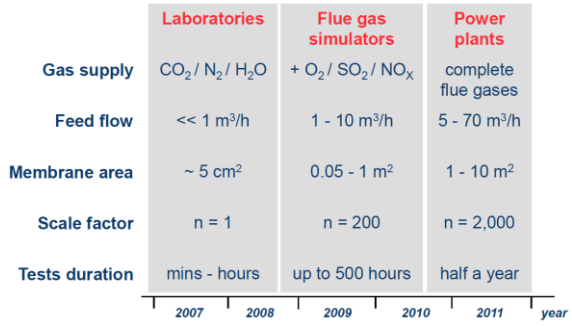

Figure 2.21: NanoGLOWA project targets [81].

Pilot plant tests on membranes for post-combustion capture are also reported in the aim of the CO2CRC project [30] in particular the H3 project which involves tests on flue gas from IPH International Power Hazelwood. Unfortunately, no data are available from this project to date.

2.7 The importance of a flexible capture unit for future CCS applications

The previously reviewed solutions from the literature are based on steady-state simulations. However, dynamic operations represent a challenging aspect in terms of future CCS applications, since flexibility will become one of the key aspects. One of the main problems of renewables is in fact their low capacity factor and their fluctuation on both daily and annual basis. In Figure 2.22 the UK average annual capacity factor for renewables is reported.

Consequently, fossil plants should be able to guarantee the demand when these fluctuations take place but this will require frequent start-ups and shut-downs of the plants. Despite gas-fired power plants are more adapt to a flexible operation, coal-fired power stations will also be required to meet the energy demand. In the perspective of an increasing role of renewables, the need for flexible plant operation is expected to become a key element. On the other hand, in order to achieve the GHG emission reduction targets in the next decades [6], CCS will be also required: therefore, the capture scheme should be designed to guarantee this flexibility.

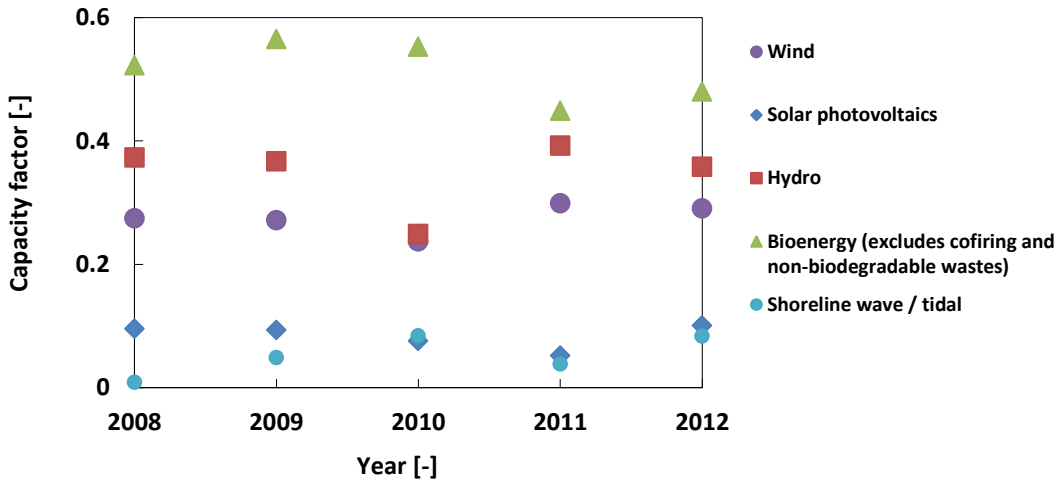

Figure 2.22: Capacity factor for renewables in UK averaged per year, 2008 – 2012 [82].

Another important aspect in terms of a flexible operation is also the deployment of the capture units depending on both demand and electricity price. In Figure 2.23 the 2012 demand for UK with respect to daily time is presented [83]. The trend is quite homogeneous and it is dependent on both season and peak times. In Figure 2.24 the 2012 daily trend of *System Selling Price* (SSP) for electricity is presented: in this case dramatic fluctuations can be observed. An analysis of both Figure 2.23 and Figure 2.24 shows that there are prospects for flexible CCS operations on a daily basis. Therefore, an understanding of the response of the capture system is essential. It may be in fact more convenient for the plant owner to run the plant at full load in order to maximise the profits during certain hours. In this case, a continuous operation of the plant can be assumed associated to a discontinuous capture rate.

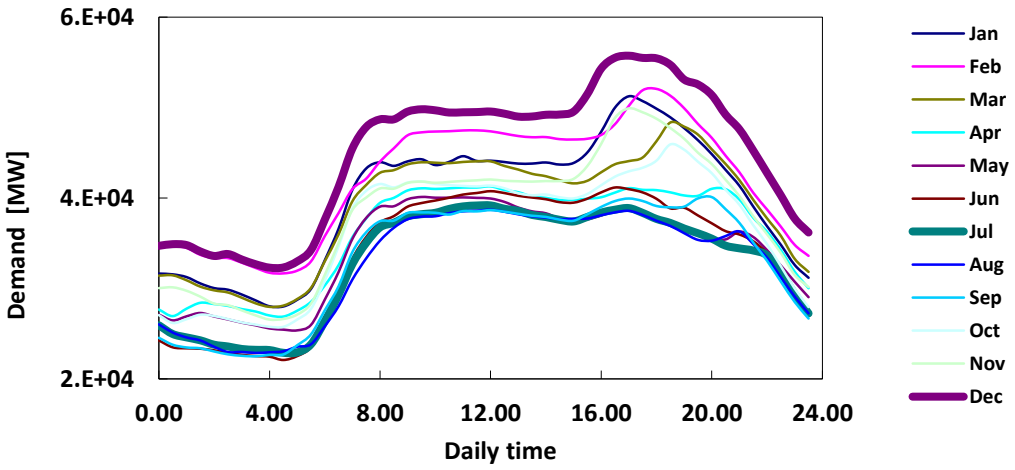

Figure 2.23: UK 2012 monthly averaged daily demand [83].

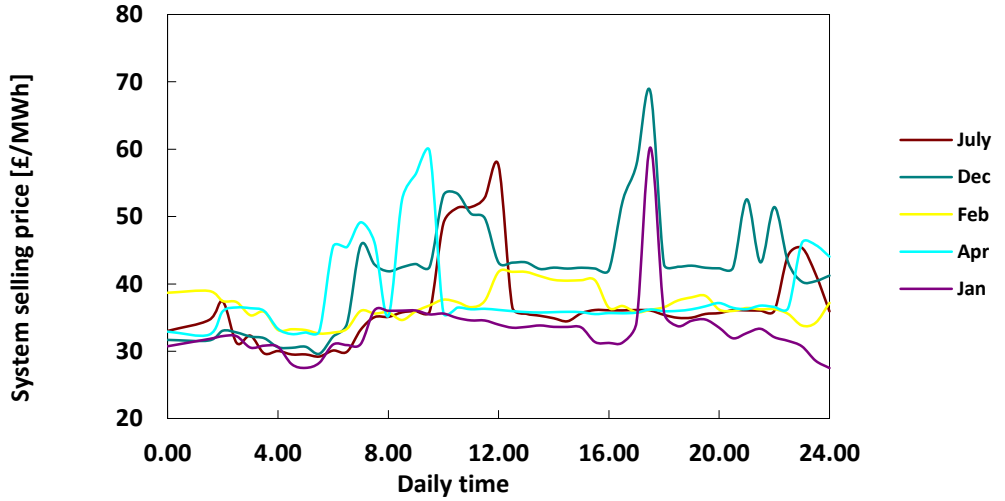

Figure 2.24: Monthly averaged daily trend for 2012 System Selling Price (SSP) [83].

In the literature studies on flexible amine capture are available [84, 85] and their main idea is to store the solvent and to regenerate it when either demand or electricity selling price are lower.

Dynamic simulations for carbon capture applications are not available yet in the literature for membrane separation since, as previously mentioned, it is generally assumed that membranes have a fast response to fluctuations in process conditions. Despite this will not be the main focus of this thesis, preliminary single-stage simulations will be run to validate this assumption for carbon capture applications and to evaluate the potential of membrane separation under dynamic conditions. This could give important indications on the application of this technology in case of discontinuous operations as start-up/shut-down procedures and changes in process conditions.

Chapter 3: Membrane module modelling

In this Chapter the modelling of the separation is investigated: both theory and numerical approach are presented. The aim of this work is to predict the separation through both hollow-fibre and spiral-wound modules, which are among the most common membrane module configurations [26].

In a hollow-fibre permeator schematically shown in Figure 3.1, a bundle of fibres is assembled in analogy with shell-and-tube heat exchangers. The feed can be either at bore or shell side and the flow patterns which can be found in these modules are co/counter-current, cross-flow or, more likely, a combination of these.

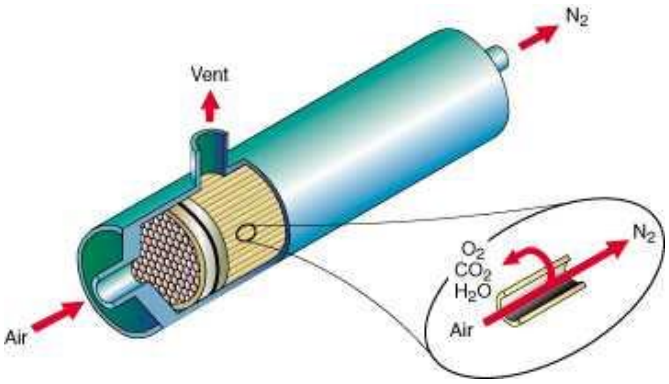

Figure 3.1: Representation of a hollow-fibre module from MEDAL™ - Air Liquide [86].

In a spiral wound module one or multiple membrane sheets are assembled around a central perforated collection pipe, as shown in Figure 3.2. Spacers are present on both feed and permeate sides to allow the flow through the two compartments and a schematic representation is reported in Figure 3.3. The retentate flow is along the main direction of the module, while the permeate stream flows in a perpendicular direction before being collected in the collection pipe. The flow pattern which can be found in these modules is cross-flow.

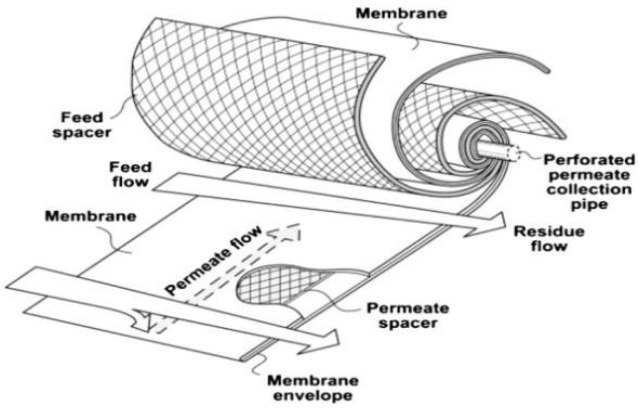

Figure 3.2: Spiral-wound module [26].

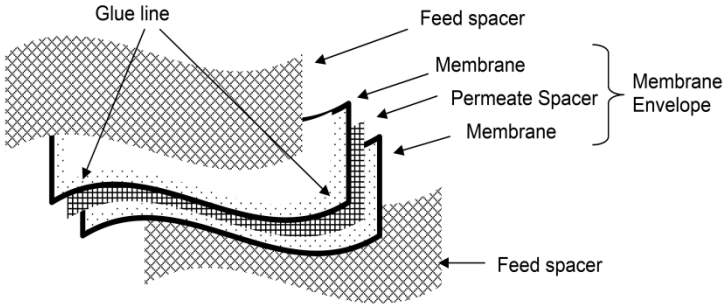

Figure 3.3: Membrane envelope in a spiral-wound module [87].

The investigation in the following paragraphs starts from the models available in the literature before focusing on bi-dimensional analyses aiming at more detailed predictions. A complete list of the parameters used in this Chapter with relative units is reported in Appendix A.

3.1 Preliminary models

In this section the models available in the literature which use membrane area as main design parameter are considered. Therefore, no module geometry is required.

The first approach to the modelling process is considering the membrane module as a well-mixed system on both sides [2, 8]. The general form of the mass balance for **NC** components consists in a set of nonlinear algebraic equations reported in Eq. (2.1) - (2.4). **F** is the molar flow, **x** is the vector of the molar fractions, **A** is the membrane area, **P** is the pressure and **π** is the component permeance. Suffixes **r** and **p** refer to retentate and permeate side. Component mass balances are reported in Eq. (2.1) and Eq. (2.2) for, respectively, overall system and permeate side. The closure condition for retentate and permeate molar fractions in Eq. (2.3) and Eq. (2.4) are also required.

$$F_f x_{fi} = F_r x_{ri} + F_p x_{pi} \qquad i = 1...NC \tag{2.1}$$

$$F_p y_{pi} = \pi_i \left(P_r x_{ri} - P_p x_{pi} \right) A \qquad i = 1...NC \tag{2.2}$$

$$\sum_{i=1}^{NC} x_{ri} = 1 \tag{2.3}$$

$$\sum_{i=1}^{NC} x_{pi} = 1 \tag{2.4}$$

This model does not completely represent the behaviour of industrial modules, since constant driving force is assumed between the two compartments. However, it can be considered as a starting point both for its quick numerical resolution and for an initial indication of the performances. In the literature [88, 89] the average logarithmic mean is also considered in the permeation term in Eq. (2.1) and Eq. (2.2) in order to achieve a more realistic prediction.

A more accurate approach considers the two sides as one-dimensional plug-flow, coupled by the flux through the membrane. Under the main assumptions of constant permeabilities along the module, no pressure drops, isothermal and ideal behaviour the model is formulated as reported in the literature [1-3, 8]. It is important to point out that in this model the effect of dispersion is not taken into account, which in a plug-flow reactor accounts for contributions as molecular diffusion, turbulent mixing

and laminar velocity profiles [90]. Therefore, this model will be referred as non-dispersed plug-flow throughout this thesis.

The set of differential equations which represent the mass balance across the system is given by Eq. (2.5) - (2.6) for retentate side and Eq. (2.7) – (2.8) for permeate side.

$$\frac{d\left(F_r x_{ir}\right)}{dA} = -\pi_i \left(P_r x_{ir} - P_p x_{ip}\right) \quad i = 1...NC \tag{2.5}$$

$$\frac{dF_r}{dA} = -\sum_{i=1}^{NC} \pi_i \left(P_r x_{ir} - P_p x_{ip}\right) \tag{2.6}$$

$$\frac{d\left(F_p x_{ip}\right)}{dA} = \pi_i \left(P_r x_{ir} - P_p x_{ip}\right) \quad i = 1...NC \tag{2.7}$$

$$\frac{dF_p}{dA} = \sum_{i=1}^{NC} \pi_i \left(P_r x_{ir} - P_p x_{ip}\right) \tag{2.8}$$

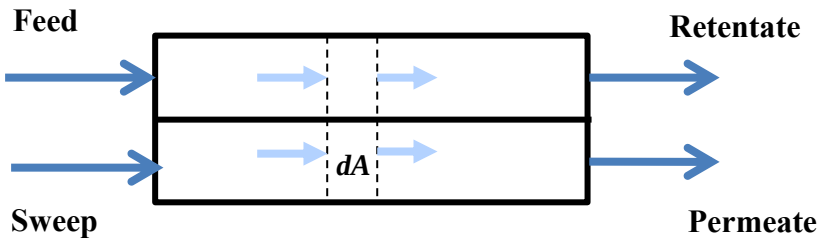

Figure 3.4: Co-current representation.

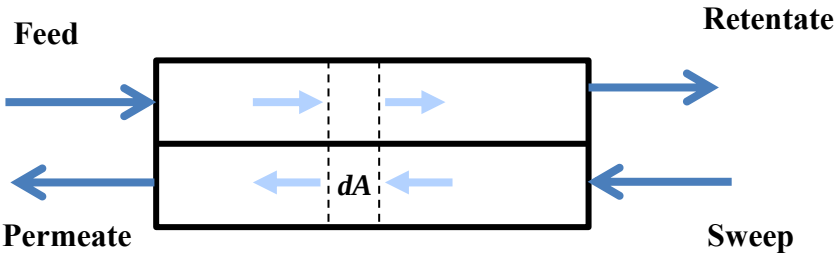

Figure 3.5: Counter-current representation.

The inlet boundary conditions for the retentate side are feed flow rate and molar fractions. According to the sign of the permeate molar flow, this model can account for both co- and counter-current flow patterns, as evident from Figure 3.4 and Figure 3.5. An important option is the sweep, a stream with a low concentration of the most permeable components which can be sent as inlet to the permeate side. This lowers the partial pressure, therefore increasing the driving force for the separation. In the case of no-sweep, the no-flux condition for the permeate inlet is used.

Cross-flow models are also widely used in the literature, under the same assumptions as the one-dimensional plug-flow models previously reported. The first proposed formulations accounting for a cross-flow flow pattern for a bi-component mixture [91-93] can be referred as cross-plug flow: the retentate is modelled as plug-flow similarly to co- and counter-current cases, while the permeate side is considered as withdrawn in perpendicular direction to the membrane. This model assumes no mixing on the permeate side and, consequently, the local permeate composition is calculated from the ratio of the local fluxes reported in Eq. (2.9).

$$\frac{x_p}{1-x_p} = \frac{\alpha\left(x_r - \theta \cdot x_p\right)}{[1-x_r - \theta(1-x_p)]} \tag{2.9}$$

Where $\mathbf{x_r}$ and $\mathbf{x_p}$ are retentate and permeate molar fractions, $\boldsymbol{\theta}$ is the pressure ratio (ratio between permeate and feed pressure) and $\boldsymbol{\alpha}$ is the selectivity of the membrane.

Saltonstall [94] propose a cross-flow model for a bi- and multi-component mixture with no pressure drops. The presented method calculates the permeate compositions, flux and area over small increments of change in feed composition. The single contributions are then summed over the entire area to obtain the outlet streams.

Shao et al [41] in their modelling analysis for CO_2/N_2 separation assume cross-flow permeation inside a membrane module divided in segments: plug-flow occurs on retentate and no mixing occurs on the permeate side. The contributions of the single components are summed over the entire area and an equation relating permeate and retentate molar fractions, membrane selectivity and pressure ratio is obtained.

A common assumption in cross-flow modelling is that no mixing occurs after permeation, with the permeate stream withdrawn perpendicularly to the retentate flow. In different investigations [95-97] the retentate side is considered as plug-flow and the algebraic constraint in Eq. (2.10) is adopted.

$$\frac{d\left(F_r x_{ir}\right)}{dF_r} = x_{ip} \tag{2.10}$$

Consequently, the model results in a set of differential and algebraic equations: the resolution is similar to the plug-flow cases but the permeate side is solved by using the algebraic constraint in Eq. (2.10). The equations for the retentate side are analogous to Eq. (2.5) – (2.6).

The models implemented in this analysis which will be used as term of comparison with the more detailed predictions are:

- Well-mixing on both sides: Eq. (2.1) - (2.4);
- One-dimensional non-dispersed plug-flow: Eq. (2.5) - (2.8);
- 1D cross-flow model: plug-flow on retentate side according to Eq. (2.5) - (2.6) and no-mixing constraint on permeate side according to Eq. (2.10).

These models represent the starting point for having a first approximation of the separation behaviour of a membrane permeator. In the next paragraphs more detailed analyses of both hollow-fibre and spiral-wound modules will be carried out and bi-dimensional models will be presented.

3.2 Hollow-fibre modelling

Hollow-fibre modules are widely adopted in industry and their main strength is the high area/volume ratio, which is reported to reach values up to 10000 m^2/m^3 [29]. In order to achieve these characteristics, research effort is currently focused on

assembling fibres with small diameters, which can be down to μm scale [26]. A uniform diameter and thickness of both selective layer and porous support are essential for having a performing separation as well as optimized module geometries [26, 29, 98, 99].

Different studies in the literature present one-dimensional analyses of hollow-fibre permeators where the bore side is modelled as a plug-flow. Pressure drops are generally expressed as Hagen-Poiseuille dependency which can be assumed valid for Reynolds numbers lower than 2000 [100]. Different investigations based on non-dispersed plug flow models, using membrane area as main design parameter, confirmed the best overall performances of counter-current configurations [39, 93] in comparison to co-current. Therefore, counter-current flow pattern is generally adopted in 1D hollow-fibre analyses but also in industrial applications.

Due to its relatively simple implementation, the most common approach in the literature for hollow-fibre modelling consists in the non-dispersed plug-flow models presented in Section 2.2 [60, 61, 101, 102].

Pan [97] investigates a bi-component separation using a 1D plug-flow model on both sides: this type of approach is used in many analyses for multi-component separations due to its relatively simple implementation [60, 61, 101, 102]. Chern et al. [103] carry out a 1D analysis applied to natural gas separation where the effect of fibre dimension on the bore-side pressure drop is investigated, the shell side is modelled as plug-flow and pressure drops are usually neglected as in other studies [104].

Coker et al. [104, 105] present both an isothermal and a non-isothermal analysis based on a 1D model which is applied to natural gas and hydrogen separations. Redlich-Kwong-Soave equation of state is included in order to study real-gas behaviour which is expected to be significant in high pressure separations with non-ideal mixtures [106]. The gas expands while permeating through the membrane and a change in temperature is expected according to the Joule-Thomson effect.

Non-ideal behaviour using a 1D model is also investigated in the work by Wang et al. [107] where the flux through the membrane is written in terms of fugacities. A similar approach is adopted by Scholtz et al. [108] who analyse non-idealities and model pressure drops on the shell-side with Hagen-Poiseuille relationship, written in terms of equivalent radius.

Thundyil and Koros [109] take into account different flow patterns inside a hollow-fibre module for gas separation: co-current, counter-current and radial cross-flow are compared using a finite element approach. Radial cross-flow is the flow pattern which can be found if the modules are fed from the shell side and a perforated pipe is placed at the centre of the fibre bundle to collect the permeate stream. This flow pattern is identified by Thundyil and Koros [109] as optimal in terms of flow distribution and for a better mitigation of thermal effects, while counter-current is favourable for larger bundle sizes. Radial cross-flow is also simulated by Marriot et al. [110, 111] who present a detailed 1D and 2D analysis in hollow-fibre permeators in terms of mass, energy and momentum balances applied to gas and liquid separation.

Labecki et al. [112] develop a 2D hollow-fibre model where both sides are treated as two interpenetrating porous regions where membrane and fluid are assumed as incompressible. This is called Porous Medium Model (PMM) and it strictly related to the assumption of low Reynolds numbers where Darcy`s flow can be applied, as in the reported filtration and membrane contactor examples. A similar 2D approach can be found in Lemanski et al. [113] who present a 2D model for hollow-fibre permeators: equations are volume-averaged, Darcy's law is adopted for both shell and bore sides and the results are compared and validated using a shell-fed module for air separation. Wang and Cussler [114] present an analysis based on a compartmental modelling approach where the feed is at the shell-side. A model including concentration gradient only on the shell is implemented and compared to a 2D approach where the bore profile is also considered. Perfect mixing and no-mixing are simulated in the connection between one compartment and the adjacent one. An

analysis investigating the effect of different number of compartments is also carried out and the model is applied to membrane contactors.

3.2.1 General assumptions and design parameters

Before focusing on the hollow-fibre models presented in this thesis, module assumptions for both 1D and 2D cases are presented. The membrane permeator is assumed to have a rectangular section, following the analysis of Wang and Cussler [115].

The design parameters which account for hollow-fibre module geometry are:

- Module area density **σ** [membrane area/module volume, m^2/m^3];
- Fraction of volume occupied by the fibres **Δ** and number of fibres $\mathbf{N_f}$;
- Fibre internal $\mathbf{r_{in}}$ and external radius $\mathbf{r_{out}}$, consequently the thickness of the porous support can be calculated assuming a membrane with asymmetric structure. The selective layer is assumed in the external part of the fibre and its thickness is considered as negligible compared to the porous support;
- External dimensions: module length **L**, width **W** and height **H**.

The module is assumed to have the feed on the shell side [105, 113]. The input parameters are module area density, volume fraction, thickness of the porous support and membrane permeance from which the remaining parameters can be calculated by using Eq. (2.11) and Eq. (2.12).

$$\sigma = \left[\frac{m^2}{m^3}\right] = \frac{A}{V} = \frac{2\pi N_f r_{out}}{W H} \tag{2.11}$$

$$\Delta = \left[\frac{m^3{}_{bore}}{m^3{}_{shell}}\right] = \frac{N_f \pi r_{out}{}^2}{W H} \tag{2.12}$$

The choice of this work is to fix these variables since they can be considered as realistic design parameters in industrial modules. However, different parameters as

the total number of fibres can also be fixed but input variables need to be consistent with Eq. (2.11) and Eq. (2.12).

3.2.2 1D hollow-fibre model

The first approach in the proposed modelling analysis consists in a 1D model based on available literature [104]. Both feed and permeate sides are considered as disperse plug-flow, with the option of co- and counter-current flow pattern and sweep at the permeate side. A module schematic is reported in Figure 3.6.

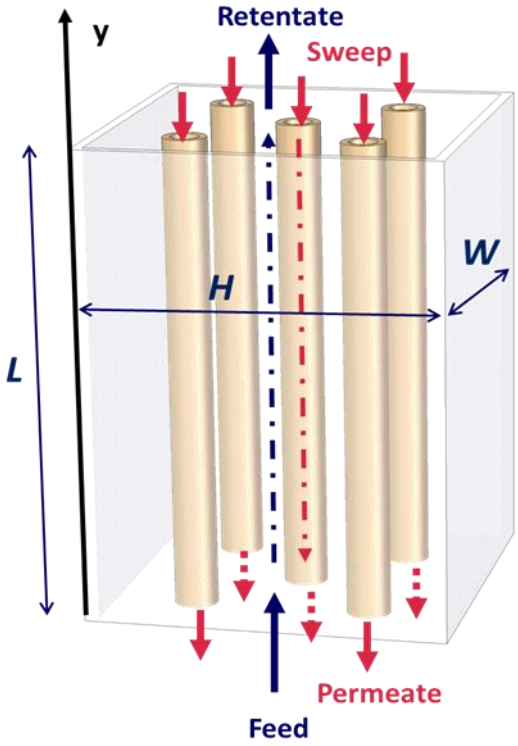

Figure 3.6: 1D hollow-fibre representation for counter-current operation.

Differently from the model reported in Eq. (2.5) - (2.8), here module geometry is taken into account and membrane area is not the only design parameter. Therefore, a more detailed simulation of module performances can be achieved. A comparison between models with different level of accuracy will be carried out in Chapter 3.

Apart from considering module geometry, this model accounts for the dispersion contribution along the axial direction. Therefore, considering a fibre of generic cross-section **S** and in position $\mathbf{y_o}$ along the module, the flow of component i [mol/s] is the sum of convective and dispersive flow, as reported in Eq. (2.13), where **D** is the axial dispersion coefficient, **u** is the velocity and **c** is the concentration.

$$\left(u\ c\ x_i S\right)\Big|_{y_0} - \left(S\ D\ \mathrm{c}\ \frac{dx_i}{dy}\right)\Bigg|_{y_0} \tag{2.13}$$

The axial dispersion coefficient **D** is calculated depending on the Reynolds number using the correlations reported by Levenspiel [90], as reported in Figure 3.7. Therefore, this model can also be referred as dispersed plug-flow.

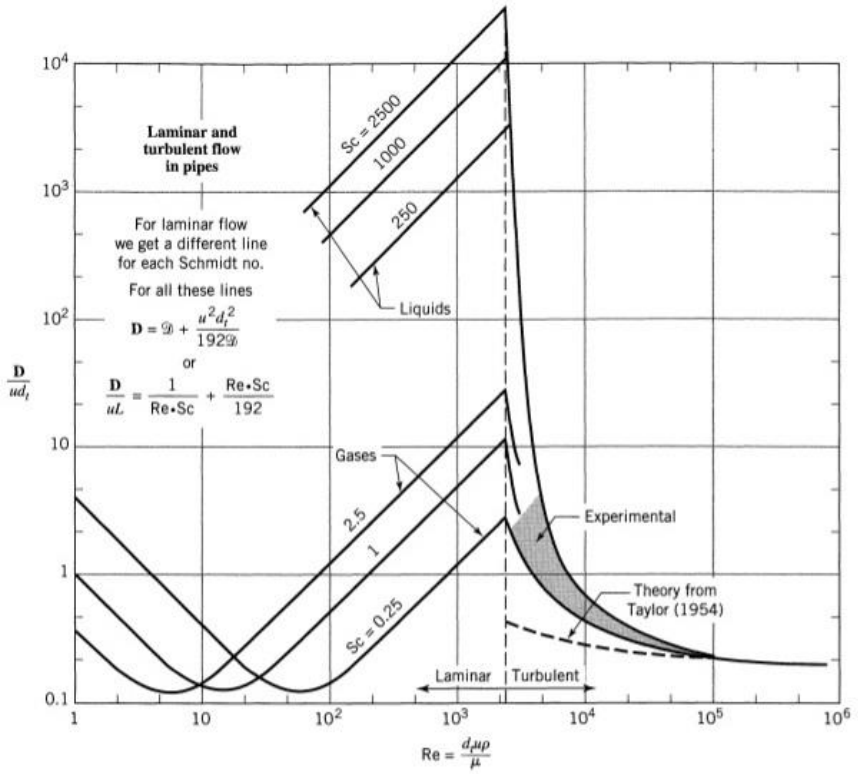

Figure 3.7: Dispersion coefficient and its dependence with respect to Reynolds (Re) and Schmidt (Sc) numbers [90]. Legend: $\mathscr{D}$ is the molecular diffusion, u is the velocity, d_t is the diameter of the fibre and L is the length of the fibre.

Component and total mass balances for feed and permeate side are reported in Eq. (2.14) - (2.17) where **u** is the velocity, **c** is the concentration, **D** is the axial dispersion coefficient and $\mathbf{N_i}$ is the flux through the membrane.

$$\frac{d}{dy}\left(u_r c_r\right)+\left(\frac{\sigma}{1-\Delta}\right)\sum_{i=1}^{NC} N_i = 0 \tag{2.14}$$

$$\frac{d}{dy}\left(u_r c_r x_{ir}\right)-\frac{d}{dy}\left(D_r c_r \frac{dx_{ir}}{dy}\right)+\left(\frac{\sigma}{1-\Delta}\right)N_i = 0 \tag{2.15}$$

$$\frac{d}{dy}\left(u_p c_p x_{ip}\right)-\frac{d}{dy}\left(D_p c_p \frac{dx_{ip}}{dy}\right)-\left(\frac{\sigma}{\Delta}\right)N_i = 0 \tag{2.16}$$

$$\frac{d}{dy}\left(u_p c_p\right)-\left(\frac{\sigma}{\Delta}\right)\sum_{i=1}^{NC} N_i = 0 \tag{2.17}$$

The cross-sectional areas for retentate and permeate sides are calculated from Eq. (2.18) and Eq. (2.19).

$$A_s^r = \left(1-\Delta\right)\left(W\,H\right) \tag{2.18}$$

$$A_s^p = \Delta\left(W\,H\right) \tag{2.19}$$

The permeate flow can have both positive and negative sign according to the flow pattern and Danckwerts boundary conditions are adopted as well. These need to be adopted if the dispersion contribution is taken into account [90]. They are reported in (2.20) and (2.21) for shell side.

$$c_r u_r x_{ir}\big|_{y=0} - D\,c_r \left.\frac{dx_{ir}}{dy}\right|_{y=0} = c_r u_r x_{ir}\big|_{\mathrm{IN}} \tag{2.20}$$

$$\left.\frac{dx_{ir}}{dy}\right|_{y=L} = 0 \tag{2.21}$$

Pressure drops are included into the model formulation: their effects are expected to affect the performances, particularly in terms of energy consumption. Hagen-Poiseuille relationship is assumed for bore side pressure drops [100] since the reported simulations are in laminar regime, with Re < 1000. The formulation for pressure drop in the bore side is reported in Eq. (2.22) that is coupled with a fixed pressure at the outlet.

$$\frac{dP}{dy} = -\left(\frac{8\mu}{\pi \cdot r_{in}^{\ 2}}\right)u \tag{2.22}$$

where $\boldsymbol{P}$ is the pressure, $\mathbf{r_{in}}$ the internal diameter and $\boldsymbol{\mu}$ is the static viscosity, which is calculated point-by-point considering the property of the mixture [116].

In the literature, shell-side pressure drops are often neglected [104] but they are expected to be significant, particularly for shell-feed modules. Here the equivalent shell diameter $\mathbf{r_{eq}}$ is calculated, following the relationships available for heat exchangers [117], and the Hagen-Poiseuille relationship is assumed in terms of equivalent radius [108].

As a further step of the analysis, energy balance is also included into the model formulation [105, 108] as reported in Eq. (2.23) and Eq. (2.24) for, respectively, retentate and permeate sides. Danckwerts` boundary conditions are adopted and they are reported in Eq. (2.25) and Eq. (2.26) for the shell side.

$$\frac{d}{dy}\left(\sum_{i=1}^{NC} c_{ir} u_r H_i\right) - \frac{d}{dy}\sum_{i=1}^{NC}\left(D_i c_t \frac{dx_{ir}}{dz} H_i\right) - k\frac{d^2 T_r^2}{dy^2} + \frac{\sigma}{(1-\Delta)} H_m \sum_{i=1}^{NC} N_i + \\ + \frac{h_m \cdot \sigma}{(1-\Delta)}\left(T_r - T_p\right) + \frac{h_w}{w(1-\Delta)}\left(T_r - T_{amb}\right) = 0 \tag{2.23}$$

$$\frac{d}{dy}\left(\sum_{i=1}^{NC} c_{ip} u_p H_i\right) - \frac{d}{dy}\sum_{i=1}^{NC}\left(D_i c_p \frac{dx_{ip}}{dy} H_i\right) - k\frac{d^2 T_p}{dy^2} - \frac{\sigma}{\Delta} H_m \sum_{i=1}^{NC} N_i - \\ - \frac{h_m \sigma}{\Delta}\left(T_r - T_p\right) + \frac{h_w}{w\Delta}\left(T_p - T_{amb}\right) = 0 \tag{2.24}$$

$$\sum_{i=1}^{NC} c_{ir} u_r H_i \Big|_{y=0} - k \frac{dT_r}{dy}\Big|_{y=0} = \sum_{i=1}^{NC} c_{ir} u_r H_i \Big|_{IN} \tag{2.25}$$

$$\frac{dT_r}{dy}\Big|_{y=L} = 0 \tag{2.26}$$

H is the enthalpy, **T** the temperature, **k** the thermal conductivity, **h** the heat transfer coefficient between the sides and $\mathbf{h_w}$ the heat transfer coefficient with the environment. The enthalpy of the permeating $\mathbf{H_m}$ stream is assumed at the same conditions as the retentate stream, considering an iso-enthalpic decompression through the membrane film [108].

The overall heat transfer coefficient $\mathbf{h_m}$ is determined following the correlations presented by Coker et al. [105] taking into account the contribution of convection and conduction for both gases and membrane. Both a constant and a position-dependent heat transfer coefficient are assumed. However, no significant changes are encountered by using the different approaches.

In order to achieve more realistic predictions – particularly for high-pressure separations – non-ideal behavior is also taken into account, following similar analyses presented in the literature [105, 108]. In particular, for gases having high Joule-Thomson coefficients (e.g. CO_2 and CH_4) a change in temperature can be encountered due to the expansion of the gas during permeation. In the case of natural gas and hydrocarbon separations, the temperature can be below the dew point of the mixture causing undesirable condensations inside the module. This dramatically affects the performances causing reduction of effective area and possible problems in compressor equipment. Both Virial and Peng-Robinson (PR) equation of state are included into the model formulation according to the formulation reported in Reid and Prausnitz [116]. Virial EOS is used for carbon capture simulations (the pressure is lower than 0.5 MPa) while PR EOS is used for validating natural gas separations (approximately 6.0 MPa).

As a general approach to non-ideal behavior:

- the EOS is included into the program (substituting it to ideal gas law);
- the flux through the membrane is expressed in terms of fugacity coefficients [108] as reported in Eq. (2.27);
- the residual function is used for the enthalpy calculation in Eq. (2.28), assuming no mixing effects.

$$H = \sum_{i=1}^{NC} x_i H_i + H_R(T, P, x) \tag{2.27}$$

$$N_i = \pi_i \left(\phi_r P_r x_{ir} - \phi_p P_p x_{ip} \right) \tag{2.28}$$

3.2.3 2D hollow-fibre compartmental model

In order to evaluate the effect of a combined flow pattern in hollow-fibre separators, a 2D compartmental model is now implemented. The analysis is based on the work from Wang and Cussler [115] who apply their model to membrane contactor applications. In the case of gas separation, the fluid is compressible and gas permeation is included into the model. Equal sections divided by baffles are considered, in analogy to shell-and-tube heat exchangers. The flow pattern inside each compartment is cross-flow: depending on the sign of the shell side flow, the overall separation can be considered either co- or counter-current. In Figure 3.8 a 5-compartment module in overall counter-current flow is represented. Similarly to the 1D analysis, the feed is on the shell side.

The set of equations for the gas separation model is the same as the 1D model but, in this case, the spatial coordinates are two: **z** and **y** directions. When the fluid leaves the compartment, it is assumed that complete mixing occurs. Consequently, average conditions after mixing are calculated and homogeneous inlet boundary conditions are assumed in the following compartment.

Particular attention should be focused on the calculation of the cross-sectional area for the shell-side analysis. Due to the different geometry, the flow is now perpendicular to the module height. Therefore, the adopted formulation reported in Eq. (2.29) calculates the equatorial cross-sectional area as in cross-flow shell-and-tube heat exchangers [117]. In order to simplify the nomenclature the parameter **Δ*** - void fraction for the shell side - is introduced in Eq. (2.30), where $\mathbf{d_0}$ is the outer fibre diameter and $\mathbf{p_t}$ (calculated as $1.25 \cdot d_0$ from Sinnott [117]) is the tube pitch.

$$A_s^r = (W\ L_b)\frac{p_t - d_0}{p_t} = (W\ L_b)\Delta^* \tag{2.29}$$

$$\Delta^* = \frac{p_t - d_0}{p_t} \tag{2.30}$$

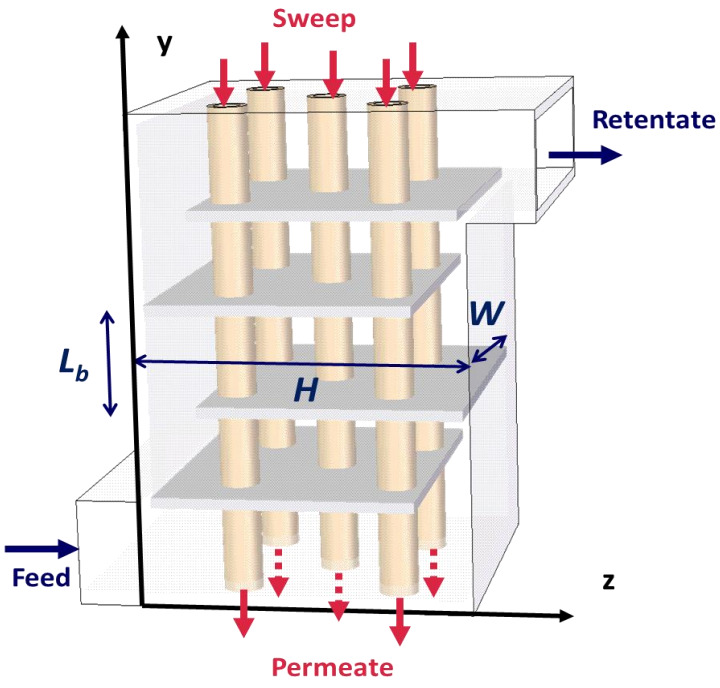

Figure 3.8: Compartmental model representation - shell feed and counter-current flow pattern.

Component, overall mass balance and energy balance for the shell-side are reported in Eq. (2.31) - (2.33). The permeate side along y direction as an analogous

formulation to the 1D model previously reported, since the flow is on the direction of the fibres.

$$\frac{\partial}{\partial z}\left(u_r c_r x_{ir}\right)-\frac{\partial}{\partial z}\left(D_r c_r \frac{\partial x_{ir}}{\partial z}\right)+\left(\frac{\sigma}{\Delta^*}\right)N_i=0 \tag{2.31}$$

$$\frac{\partial}{\partial z}\left(u_r c_r\right)+\left(\frac{\sigma}{\Delta^*}\right)\sum_{i=1}^{NC}N_i=0 \tag{2.32}$$

$$\frac{\partial}{\partial z}\left(\sum_{i-1}^{NC}c_{ir}u_r H_i\right)-\frac{\partial}{\partial z}\sum_{i=1}^{NC}\left(D_i c_t \frac{\partial x_{ir}}{\partial z}H_i\right)-k\frac{\partial^2 T_r^2}{\partial z^2}+\frac{h_m\,\sigma}{\Delta^*}\sum_{i=1}^{NC}H_i N_i+$$
$$+\frac{h_m\,\sigma}{\Delta^*}\left(T_r-T_p\right)+\frac{h_w}{w\cdot\Delta^*}\left(T_r-T_{amb}\right)=0 \tag{2.33}$$

Non-ideal behavior is also included into the model formulation in analogy to the one-dimensional case (Section 3.2.2) considering both Virial and Peng-Robinson EOS.

3.2.4 Momentum balance for the compartmental model

Momentum balance is included into the compartmental analysis analogy with the 1D case. Bore-side pressure drops follow Hagen-Poiseuille relationship as the 1D model, while for the shell side a different correlation should be used due to the different geometry.

Lemanski and Lipsicomb [113] in their 2D analysis of hollow-fibre permeators assume Darcy`s relationship for both bore and shell side. Different formulations for the Darcy`s permeability coefficient are available in the literature [118, 119] but they are only valid for viscous flow regime. However, in the simulations reported in this thesis, higher Reynolds numbers are obtained, despite still in the laminar regime. Therefore, a more detailed analysis of shell side pressure drops needs to be carried out.

Costello et al. [100, 120] investigate pressure drops in hollow-fibre modules applied to membrane contacting: an Ergun-type relationship reported in Eq. (2.34) is adopted and validated with experimental results. In particular, the effect of packing density is analysed for Reynolds number in the range 20 < Re < 350 showing that for packing densities lower than 50 %, the turbulent contribution is significant. Ergun equation in its general formulation can also be applied for gas separation and, in this case, the fluid is compressible.

$$\frac{dP}{dz} = F_{viscous}\, u + F_{inertial}\, u^{1.75} \tag{2.34}$$

Correlations adopted in heat exchanger design have also been investigated: an example is given by Prithiviraj et al. [121] who analyse the shell-side flow inside heat exchangers accounting for cross-flow flow pattern. The expression in Eq. (2.35) is adopted calculating the parameter **K** depending on Reynolds number and geometry as reported by Rehme [122].

$$\frac{dP}{dz} = -\frac{0.5\,K}{dz}\,\rho\, u\,|u| \tag{2.35}$$

Lively et al. [123, 124] adopt a shell-fed hollow-fibre module in their analysis focused on Rapid Temperature Swing Adsorption for carbon capture applications. The adopted correlation for shell-side pressure drops is based on heat exchanger design and it is reported in Eq. (2.36). $\mathbf{N_r}$ depends on the geometry and it represents the obstacle to the flow due to the fiber bundle, $\boldsymbol{f}$ is a friction factor and $\boldsymbol{\mu_w}$ is the viscosity at the wall. Their initial calculations show lower pressure drops than 30 kPa which are feasible for a blower on the feed side.

$$\Delta P_s = \frac{2\, f\, \mathrm{N_r} \rho\, u^2}{2}\left(\frac{\mu}{\mu_w}\right)^{-0.14} \tag{2.36}$$

The analysis developed in this thesis is based on two approaches which are widely adopted for heat exchanger design: Kern and Bell-Delaware methods. This represents

an innovative aspect compared to the available literature and it aims at a more detailed and realistic pressure drop estimation.

The general expression for overall shell-side pressure drops for heat exchangers using the Kern method [117] is reported in Eq. (2.37). $\mathbf{D_s}$ is the shell diameter (assuming cylindrical geometry), $\mathbf{d_e}$ is the equivalent diameter for the shell side, $\boldsymbol{\rho}$ the density, $\boldsymbol{\mu_w}$ is the viscosity at the wall and $\mathbf{j_f}$ is the friction factor depending on the baffle-cut (baffle length/shell diameter). Pitch and equivalent diameter are reported by Sinnott [117] and coefficient $\mathbf{j_f}$ can be calculated from the available plots [117] according to the baffle-cut: the higher value is assumed in order to have a conservative prediction.

$$\Delta P_s = 8\, j_f \left(\frac{D_s}{d_e}\right)\left(\frac{L}{L_b}\right)\frac{\rho u^2}{2}\left(\frac{\mu}{\mu_w}\right)^{-0.14} \tag{2.37}$$

Rearranging Eq. (2.37), the correlation for pressure drops is reported in Eq. (2.38), where $\mathbf{R_\mu}$ is the viscosity correction factor expressed in Eq. (2.39).

$$\frac{\Delta P_s}{D_s(N_b+1)} \approx \frac{dP}{dz} = -\frac{4\, j_j}{d_e} R_\mu\, \rho\, u\, |u| \tag{2.38}$$

$$R_\mu = \left(\frac{\mu}{\mu_w}\right)^{-0.14} \tag{2.39}$$

The general expression according to the Bell-Delaware method [125] is reported in Eq. (2.40), where $\mathbf{\Delta P_c}$ are the cross-flow pressure drops, $\mathbf{\Delta P_w}$ are the window pressure drops, and $\mathbf{\Delta P_e}$ is the combined contribution from end-zone inlet and outlet sections.

$$\Delta P_{total} = \Delta P_c + \Delta P_w + \Delta P_e \tag{2.40}$$

In this case, no entrance and window pressure drops are considered and the most significant contribution is represented by the cross-flow term. This is calculated from Eq. (2.41) and Eq. (2.42), where:

- $\mathbf{\Delta P_{bi}}$ is the ideal tube bank pressure drop for one baffle compartment (excluding inlet-outlet compartments);
- $\mathbf{N_b}$ is the number of baffles, $\boldsymbol{f}$ is the friction factor (dependent on Reynolds number) and $\mathbf{N_{tcc}}$ is the number of tube rows crossed between baffle tips in one baffle section;
- $\mathbf{R_B}$ and $\mathbf{R_L}$ are, respectively, bypass and leakage correction factors and they depend on the geometry;
- **M** is the mass velocity of the fluid with respect to the cross-sectional area (A_s) and **ρ** is the fluid density.

$$\Delta P_c = \Delta P_{bi}(N_b + 1)R_B R_L \tag{2.41}$$

$$\Delta P_{bi} = 0.002\, f\, N_{t,CC} \frac{M}{\rho} R_\mu \tag{2.42}$$

Rearranging Eq. (2.40) - (2.42) and making them consistent with Kern relationship, pressure drops can be expressed as in Eq. (2.43), where $\boldsymbol{k}$ depends on the geometry of the module as reported in Eq. (2.44).

$$\frac{\Delta P_s}{D_s(N_b + 1)} = \frac{1}{D_s(N_b + 1)}\, k\, f\, \rho\, u\, |u| \tag{2.43}$$

$$k = 0.002\, f\, N_{t,CC} R_\mu\, R_B R_L \tag{2.44}$$

3.3 Spiral-wound modelling

In this paragraph the attention is focused on a detailed analysis of the flow through spiral-wound modules. A schematic diagram of the flow pattern is presented in Figure 3.9: the feed channel is surrounded by two selective membrane layers.

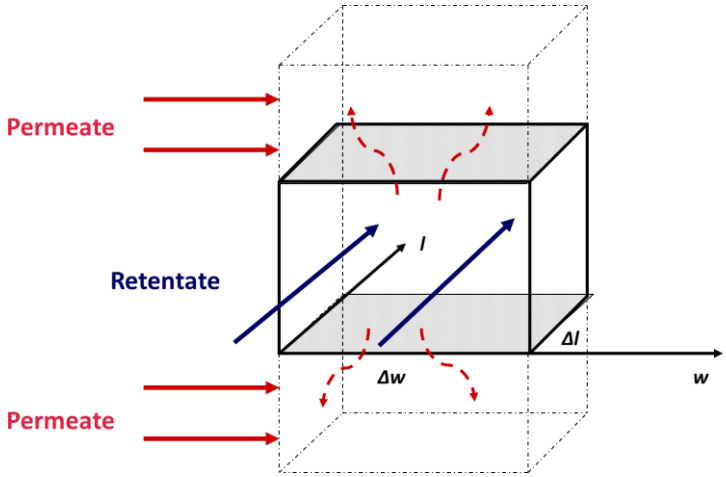

Figure 3.9: Schematic representation of the cross-flow flow pattern through a spiral-wound module.

The retentate direction consists in the module length, while the permeate side consists in the longer path along the spiral, as reported in Figure 3.10. This approximation implies the assumption of a single membrane leaf in the spiral (double selective layer with a spacer inside), while in industrial separators multiple sheets can be found [26].

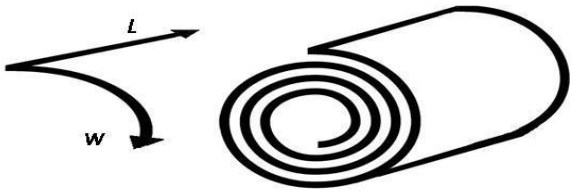

Figure 3.10: Spiral-wound representation.

Pan [97] propose a detailed cross-flow formulation through a spiral-wound module for a bi-component mixture. This consists in the first example in the literature of a bi-dimensional grid for the feed side. The component and the overall mass balance with the relative boundary conditions are shown in Eq. (2.45) - (2.48) where ***l*** (length) is the retentate and ***w*** (width) the permeate direction and **r** the retentate flow rate per unit of width.

$$\left.\frac{\partial (r x_{ir})}{\partial l}\right|_{w} = -2\pi_i \left(P_r x_{ir} - P_p x_{ip}\right) \tag{2.45}$$

$$\left.\frac{\partial r}{\partial l}\right|_{w} = -2\sum_{i=1}^{NC} \pi_i \left(P_r x_{ir} - P_p x_{ip}\right) \tag{2.46}$$

$$r(0, w) = r_f \tag{2.47}$$

$$x_{ir}(0, w) = x_{if} \tag{2.48}$$

The permeate side is modelled using a 1D model averaging flow and composition over the length direction by considering the overall mass balance, as shown in Eq. (2.49) - (2.50). **V** is the permeate molar flow while $\mathbf{r_r}$ and $\mathbf{x_{ir}}$ are, respectively, average molar flow and composition over the length direction.

$$\frac{d\left(V x_{ip}\right)}{dw} = r_f x_{if} - r_r x_{ir} \tag{2.49}$$

$$\frac{dV}{dw} = r_f - r_r \tag{2.50}$$

The choice of a 1D profile on the permeate side directly influences the computational time, affected by the increased requirements for the bi-dimensional feed side.

Qi and Henson [126-128] propose a cross-flow model for a bi-component mixture in spiral-wound permeators, starting from the solution proposed by Pan [97]. Their model consists in a set of 4 nonlinear algebraic equations based on a 1D profile for both feed and permeate side and it also accounts for permeate side pressure drops

following Hagen-Poiseuille relationship. The main assumption is that the retentate flow rate is constant along permeate flow direction.

Marriot and Sørensen [110, 111] propose a 2D cross-flow model based on a bi-dimensional grid on both sides: the approach used by Pan for the feed side is extended to the permeate compartment. Pressure drops are included following Darcy`s law and the model is validated for a reverse osmosis application. A similar analysis applied to gas separation is also reported by Brinkmann et al [129]. These bi-dimensional studies represent the starting point for the 2D model developed in this thesis.

3.3.1 2D cross-flow model

The implementation of a cross-flow model which consists in a 2D profile on both sides is now under investigation. The module structure is considered as two selective layers surrounding the central feed compartment reported in Figure 3.9. Similarly to the original formulation [4], a single membrane leaf is assumed around the central compartment.

The feed side mass balance is expressed following Pan's formulation in Eq. (2.45) - (2.48). Differently from the original model, the mass balance for the permeate side is expressed in the same formulation as the feed side. The complete set of equations with the relative boundary conditions is reported in Eq. (2.51) - (2.58).

The retentate boundary conditions are feed molar fractions and velocity (L = 0 in Figure 3.10). Since the inlet permeate side is sealed (W = 0 in Figure 3.10), the boundary condition for permeate side inlet accounts for no-flux at w = 0.

$$\left.\frac{\partial\left(r x_{ir}\right)}{\partial l}\right|_{w} = \left.\frac{\partial}{\partial l}\left(c_r u_r x_{ir} a_r\right)\right|_{w} = -2\pi_i \left(P_r x_{ir} - P_p x_{ip}\right) \tag{2.51}$$

$$\left.\frac{\partial r}{\partial l}\right|_w = \frac{\partial}{\partial l}\left(c_r u_r a_r\right)\Big|_w = -2\sum_{i=1}^{NC}\pi_i\left(P_r x_{ir} - P_p x_{ip}\right) \tag{2.52}$$

$$u(0) = u_f \tag{2.53}$$

$$x_{ir}(0) = x_{if} \tag{2.54}$$

$$\left.\frac{\partial v}{\partial w}\right|_l = \frac{\partial}{\partial w}\left(c_p u_p a_p\right)\Big|_w = -2\pi_i\left(P_r x_{ir} - P_p x_{ip}\right) \tag{2.55}$$

$$\left.\frac{\partial v}{\partial w}\right|_l = \frac{\partial}{\partial w}\left(c_p u_p a_p\right)\Big|_w = -2\sum_{\mathrm{i}=1}^{NC}\pi_i\left(P_r x_{ir} - P_p x_{ip}\right) \tag{2.56}$$

$$\frac{\partial x_{ip}}{\partial w}(l, w = 0) = 0 \tag{2.57}$$

$$u_p(w = 0) = 0 \tag{2.58}$$

Where **u** is the velocity [m/s], **c** is the concentration [mol/m^3], **a** is the channel thickness and ***w*** and ***l*** are, respectively, width and length directions.

By writing the overall set of equations in a general formulation, it is possible to investigate the effect of module geometry on the performances. For example, a different channel thickness **a** (consequently a different cross-sectional area) can be assumed for retentate and permeate channels as well as variable length and width.

It is important to point out that it is assumed that the permeate concentration is the same on both sides of the retentate channel. Despite not completely representing the situation in spiral-wound modules, this assumption can be justified by the fact that in this analysis the width W is significantly larger than the length L. It is evident from Figure 3.9 (which represents the flow pattern in a real module) that different permeate concentrations should be expected on the two permeate channels

surrounding the retentate compartment. The assumption taken in this work is also consistent with the available literature [110, 111, 129].

Once solved the system of differential equations, retentate and permeate molar flows and molar fractions are obtained by integrating the values over w for feed side and over l for permeate side. The calculation for feed side is reported in Eq. (2.59) and Eq. (2.60). An analogous formulation is used for the calculation of permeate flow rate and molar fractions.

$$F_r = \int_W r \, dw \tag{2.59}$$

$$x_{ri} = \frac{\int_W r x_{ir} \, dw}{\int_W r \, dw} \tag{2.60}$$

Pressure drops are also included into model formulation. The analysis proposed by Pan [4] accounts for pressure drops on permeate side using Darcy's law, as reported in Eq. (2.61).

$$\frac{dP^2}{dw} = -2\frac{RT\mu}{La_p B} F_p \tag{2.61}$$

According to Eq. (2.61), pressure drops depend on the thickness of the permeate channel ($\mathbf{a_p}$), the molar flow across it ($\mathbf{F_p}$) and $\boldsymbol{\mu}$ is the viscosity of the gas, while **B** is the Darcy's permeability coefficient. **R** and **T** are, respectively, ideal gas constant and temperature.

Brinkmann et al. [129] adopt Eq. (2.62) to model pressure drops on both sides side. $\boldsymbol{\rho}$ is the gas density, **a** is the channel thickness, **u** is the velocity and $\boldsymbol{\zeta}$ is a friction parameter calculated in Eq. (2.63).

$$\frac{dP}{dw} = -\xi \frac{\rho u^2}{2a} \tag{2.62}$$

$$\xi = 44\,\mathrm{Re}^{-0.55} \tag{2.63}$$

The formulation adopted in this thesis assumes pressure drops on both sides modelled assuming Poiseuille flow through parallel plates [130]. The characteristic diameter for the Reynolds number calculation is considered twice the channel thickness [130] as reported in Eq. (2.64).

$$\mathrm{Re} = \frac{\rho\,\mathrm{u}\,(2a)}{\mu} \tag{2.64}$$

The formulation for retentate and permeate pressure drop assumes the form reported in Eq. (2.65) and Eq. (2.66):

$$\left.\frac{\partial P_r}{\partial l}\right|_w = -\left(\frac{12\,\mu}{a_r^{\,2}}\right)u_r \tag{2.65}$$

$$\left.\frac{\partial P_p}{\partial w}\right|_l = -\left(\frac{12\,\mu}{a_p^{\,2}}\right)u_p \tag{2.66}$$

Assuming that a vacuum pump creates the vacuum in the central collection pipe of a spiral-wound permeator, the boundary condition in Eq. (2.67) is used.

$$P_p(w = W) = P_p \tag{2.67}$$

In analogy with the hollow-fibre analysis, energy balance is added to the model formulation and it is reported in Eq. (2.68) and Eq. (2.69).

$$\left.\frac{\partial}{\partial l}\left(H_r\sum_{i=1}^{NC}c_{ir}u_r\right)\right|_w - k\frac{\partial^2 T_r}{\partial l^2} + \frac{2}{a_r}H_m\sum_{i=1}^{NC}N_i + \frac{2\cdot h}{a_r}\left(T_r - T_p\right) = 0 \tag{2.68}$$

$$\left.\frac{\partial}{\partial w}\left(H_p\sum_{i=1}^{NC}c_{ip}u_p\right)\right|_l - k\frac{\partial^2 T_r}{\partial w^2} - \frac{2}{a_p}H_m\sum_{i=1}^{NC}N_i - \frac{2\cdot h}{a_p}\left(T_r - T_p\right) = 0 \tag{2.69}$$

H is the enthalpy, **T** is the temperature, **k** is the thermal conductivity and **h** the heat transfer coefficient between the sides. No heat transfer from the external case is considered. In analogy to the hollow-fibre case, the enthalpy of the permeating

mixture $\mathbf{H_m}$ is assumed at the same conditions as the retentate stream [105, 108]. Danckwerts boundary conditions are adopted for inlet and outlet retentate and permeate compartments. They are reported in Eq. (2.70) and Eq. (2.71) for the retentate side.

$$\sum_{i=1}^{NC} c_{ir} u_r H_i \Big|_{l=0} - k \frac{\partial T_r}{\partial l}\Big|_{l=0} = \sum_{i=1}^{NC} c_{ir} u_r H_i \Big|_{IN} \tag{2.70}$$

$$\left.\frac{\partial T_r}{\partial l}\right|_{l=L} = 0 \tag{2.71}$$

Since the membrane leafs are sealed at w = 0, the no-flux boundary condition is assumed as reported in Eq. (2.72), while at w = W the Danckwerts boundary condition reported in Eq. (2.73) is used.

$$\left.\frac{\partial T_p}{\partial w}\right|_{w=0} = 0 \tag{2.72}$$

$$\left.\frac{\partial T_p}{\partial w}\right|_{w=W} = 0 \tag{2.73}$$

The overall heat transfer coefficient between the two sides is calculated assuming fully developed laminar flow through parallel channels [130] and it is determined from the correlation reported in Eq. (2.74), where **Re** is the Reynolds number, **Nu** is the Nusselt number and **Pr** is the Prandtl number. For pressure drop relationship, the characteristic diameter for Reynolds and Nusselt number calculations is twice the channel thickness.

$$Nu = 0.453\,\mathrm{Re}^{0.5}\,\mathrm{Pr}^{0.3} \tag{2.74}$$

Simulations can also be run assuming non-ideal behavior in analogy to the hollow-fibre analysis. Therefore, both EOS and residual function for the enthalpy calculations are included into the model formulation as reported in Section 2.2.2.

3.4 Dynamic models

The attention is now focused on the preliminary dynamic analysis which has been developed in this PhD.

The models implemented in dynamic mode are:

- 1D Hollow-fibre with no pressure drops. The component mass balance for the retentate side and boundary and initial conditions are reported in Eq. (2.75) - (2.76).

$$\frac{\partial(c_r x_{ir})}{\partial t} = \frac{\partial}{\partial y}(u_r c_r x_{ir}) - \frac{\partial}{\partial y}\left(D_r c_r \frac{\partial x_{ir}}{\partial y}\right) + \left(\frac{\sigma}{1-\Delta}\right) \cdot N_i \tag{2.75}$$

$$c_r(t=0,y) = c_0 \qquad x_{ir}(t=0,y) = x_{i0} \qquad x_{ir}(t,y=0) = x_{if} \tag{2.76}$$

- 2D Cross-flow with no pressure drops. Again the mass balance is only reported for the retentate side in Eq. (2.77) and the boundary and initial conditions in Eq. (2.78).

$$a_r \frac{\partial(c_r x_{ir})}{\partial t} = \frac{\partial}{dl}(c_r u_r x_{ir} a_r)\Big|_w - 2\pi_i \left(P_r x_{ir} - P_p x_{ip}\right) \tag{2.77}$$

$$c_r(t=0,y) = c_0 \qquad x_{ir}(t=0,y) = x_{i0} \qquad x_{ir}(t,l=0) = x_{if} \tag{2.78}$$

The analysis of the results from dynamic simulations can be used to have an indication of the response of the modules to fluctuations in process conditions as well as start-up and shut-down procedures.

3.5 Software adopted for the implementation

The language chosen for implementing the models is C using *Microsoft Visual Studio 2008*. The programming approach is the same as the one followed for *CySim*, the adsorption simulator developed by the carbon capture group at the University of Edinburgh [131]. The project is linked to SUNDIALS, open source external libraries [132] which are called by the code in order to carry out the numerical resolution.

SUNDIALS is the acronyms for *SUite of Nonlinear and DIfferential/ALgebraic equation Solvers*: it is a suite of advanced computational codes for solving large-scale problems that can be modelled as a system of nonlinear algebraic equations, initial-value problems in ordinary differential or differential-algebraic equations. Once the libraries are installed, they are linked to a *Visual Studio* project by using *CMake*, an application which generates the project. In the case of the proposed steady-state models, the resolution is based on *Kinsol* which is the solver for nonlinear algebraic equations using Newton Method.

Considering a general system defined in Eq. (2.79):

$$F(u) = 0, \qquad F : R^n \rightarrow R^n \tag{2.79}$$

And given an initial guess $\mathbf{u_0}$, *Kinsol* follows the general steps for $n = 0, 1, 2\ldots$ until convergence:

1. Solve Eq. (2.80):

$$J(b_n)\delta_n = -F(b_n) \tag{2.80}$$

2. Set Eq. (2.81):

$$b_{n+1} = b_n + \lambda\delta_n, \qquad 0 < \lambda < 1 \tag{2.81}$$

3. Test for convergence

where $\mathbf{b_n}$ is the $\mathbf{n^{th}}$ iterate to **b**, and $\mathbf{J(b) = F'(b)}$ is the system Jacobian. At each stage in the iteration process a scalar multiple of the step $\boldsymbol{\delta_n}$ is added to $\mathbf{b_n}$ to produce a new iterate $\mathbf{b_{n+1}}$. The Jacobian can be either calculated by *Kinsol* or provided by the user and both *dense* and *banded* solvers are available.

3.6 Numerical resolution

In the case of the implemented steady state models, the set of differential equations is reduced to a set of nonlinear algebraic equations before being passed to *Kinsol*. The numerical resolution is now under investigation.

At a first instance, the resolution has been carried out by using finite differences (FD) method. This has been chosen as initial strategy to start the implementation. Both retentate and permeate sides are solved by using the upwind method with 1st order approximation. The derivative is calculated by using the previous grid point on the direction of the flow rate: in the case of co-current and cross-flow the flow rate of the permeate side are positive while a negative sign corresponds to the counter-current case. An example is shown here for the non-dispersed plug-flow model in counter-current flow pattern. The discretised forms of the component mass balances are reported in Eq. (2.82) and Eq. (2.83) for, respectively, retentate and permeate sides. The equations are solved for a coordinate $\mathbf{A_1}$ and $\mathbf{\Delta A}$ is expressed in Eq. (2.84) as ratio between the total area and the number of grid points **ND** for the discretisation.

$$\left.\frac{d\left(F_r x_{ir}\right)}{dA}\right|_{A=A_1} \approx \frac{\left(F_r x_{ir}\right)\big|_{A=A_1} - \left(F_r x_{ir}\right)\big|_{A=A_0}}{\Delta A} = -\pi_i \left(P_r x_{ir} - P_p x_{ip}\right)\Big|_{\mathrm{A=A_1}} \tag{2.82}$$

$$\left.\frac{d\left(F_p x_{ip}\right)}{dA}\right|_{A=A_1} \approx \frac{\left(F_p x_{ip}\right)\big|_{A=A_2} - \left(F_p x_{ip}\right)\big|_{A=A_1}}{\Delta A} = +\pi_i \left(P_r x_{ir} - P_p x_{ip}\right)\Big|_{\mathrm{A=A_1}} \tag{2.83}$$

$$\Delta A = \frac{Area}{ND} \tag{2.84}$$

However, a sensitivity of the solver to the initial guesses of the system was found. In particular, in the case of simulations with high recoveries and flat partial pressure profiles, *Kinsol* registered errors in the resolution. Different ways of calculating the initial guesses have been tried such as an initial run assuming well-mixing on both sides. In order to have a more robust and quicker resolution, a different numerical method has been adopted based on Orthogonal Collocations on Finite Elements Method (OCFEM) [133, 134]. A schematic representation of the method is shown in Figure 3.11, where **y** is the dependent variable, **NE** is the number of elements and **NP** is the number of collocation points per element.

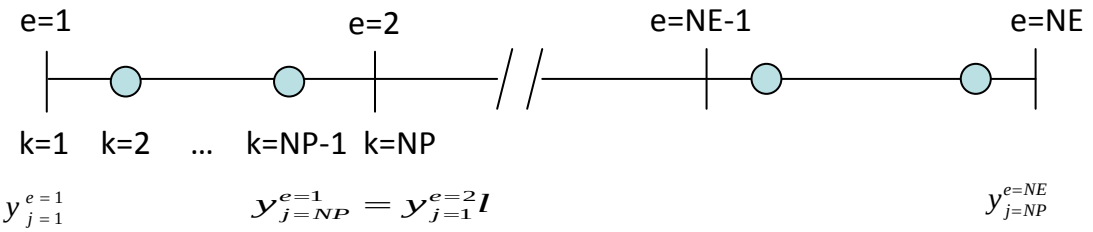

Figure 3.11: Orthogonal Collocations on Finite Elements (OCFEM) representation.

The method is now shown taking as example the retentate component mass balance for the 1D hollow-fibre model which is reported in Eq. (2.85). The relative Danckwerts boundary conditions are reported in Eq. (2.86) and Eq. (2.87). The suffix r is removed to simplify the notation in the following passages.

$$\frac{d}{dy}\left(u\ c\ x_i\right) - \frac{d}{dy}\left(D\,c\ \frac{dx_i}{dy}\right) + \left(\frac{\sigma}{1-\Delta}\right) N_i = 0 \tag{2.85}$$

$$c\ u\ x_i\Big|_{y=0} - D\,c\,\frac{dx_i}{dy}\Big|_{y=0} = c\ u\ x_i\Big|_{\mathrm{IN}} \tag{2.86}$$

$$\frac{dx_i}{dy}\Big|_{y=L} = 0 \tag{2.87}$$

The domain is divided into **NE** elements of length Δy^e as reported in Eq. (2.88).

$$\Delta y^e = y^{e+1} - y^e \tag{2.88}$$

The dependent variable is expanded in a series involving *Legendre* orthogonal polynomials. First and second order derivatives can be written in terms of orthogonal matrix A. The residual is set to zero in the internal collocation points and, consequently, Eq. (2.89) is adopted for the internal points giving NE · (NP – 2) equations.

$$\frac{1}{\Delta y^e}\left(\sum_{k=1}^{NP} A_{jk}\,(c_k^e u_k^e x_{i\ k}^{\ e})\right) + \frac{1}{\left(\Delta y^e\right)^2}\left(\sum_{k=1}^{NP} A_{jk}\left(D\,c_k^e \sum_{t=1}^{NP} A_{kt}\left(x_{i\ k}^{\ e}\right)\right)\right) + \tag{2.89}$$

$$+\left(\frac{\sigma}{1-\Delta}\right) N_i = 0 \qquad \begin{matrix} j = 2...NP-1 \\ e = 1...NE \end{matrix}$$

The remaining equations to be solved are:

- Continuity of the function and the derivative between the elements [NE-1 equations] reported in Eq. (2.90):

$$x_{i\,NP}^{\ e} = x_{i1}^{\ e+1} \tag{2.90}$$

- Continuity of the derivative at the boundaries [NE-1 equations] reported in Eq. (2.91):

$$\frac{1}{\Delta y^e}\sum_{k=1}^{NP} A_{NP,k}\,x_{i\,k}^{\ e} = \frac{1}{\Delta y^{e+1}}\sum_{k=1}^{NP} A_{1,k}\,x_{i\,k}^{\ e+1} \tag{2.91}$$

- Boundary conditions, Eq. (2.92) at e = 1, j = 1 and Eq. (2.93) at e = NE, j = NP:

$$c\ u\ x_i\Big|_{y=0} - D\,c\sum_{k=1}^{NP} A_{0,k}\,x_{i\,k}^{\ e=0} = c\ u\ x_i\Big|_{\mathrm{IN}} \tag{2.92}$$

$$\sum_{k=1}^{NP} A_{NP,k}\,x_{i\,k}^{\ e=NE} = 0 \tag{2.93}$$

The subroutine for the calculation of matrix A has been taken from Villadsen [134] and converted from *Fortran* to *C* language: degree and type of orthogonal

polynomial can be changed as inputs. The subroutine also includes the calculations of the roots of the polynomial and the quadrature weights for evaluating the integrals. The discretisation reported above is also adopted for momentum and energy balances and *Kinsol* is used to solve the resulting set of algebraic equations.

In the case of the dynamic models, the resulting set of partial differential equations is reduced to a set of ordinary differential and algebraic equations. First of all, a discretization with respect to the spatial coordinate in analogy to the steady-state case previously presented is carried out. The resulting set of differential equations with the respective initial conditions is solved using IDA from the SUNDIALS libraries, where IDA is the solver for differential-algebraic equations. An example of discretization is now reported, taking as example the 2D cross-flow model. The retentate component mass balance is reported in Eq. (2.94). Considering a generic coordinate $\mathbf{l_0}$, the discretization using finite differences is shown in Eq. (2.95), where $\mathbf{\Delta L}$ is defined in Eq. (2.96) as ratio between total length and number of discretization points $\mathbf{ND_L}$. The finite difference resolution is adopted due to the higher stability of the solver IDA compared to Kinsol, which was adopted for the steady state model.

$$a_r \frac{\partial(c_r x_{ir})}{\partial t} = \frac{\partial}{dl}\left(c_r u_r x_{ir} a_r\right)\Big|_w - 2\pi_i \left(P_r x_{ir} - P_p x_{ip}\right) \tag{2.94}$$

$$a_r \frac{\partial(c_r x_{ir})}{\partial t}\Big|_{l=l_1} = \frac{\left(c_r u_r x_{ir} a_r\right)_{l=l_1} - \left(c_r u_r x_{ir} a_r\right)_{l=l_0}}{\Delta L} - 2\pi_i \left(P_r x_{ir} - P_p x_{ip}\right)_{l=l_1} \tag{2.95}$$

$$\Delta L = \frac{Length}{ND_L} \tag{2.96}$$

3.7 Statistical analysis for module defects

The general assumption in the modelling process of hollow-fibre permeators is considering a single fibre as representative of all the fibre population, using the so-

called Krogh cylinder unit [19]. However, possible mal-distributions and fibre defects can affect the performances: for example, different fibre diameters imply different velocity profiles, therefore different pressure drops. The previously mentioned Porous Medium Model goes into the direction of considering the flow in each position of the module, but it is with statistical analysis that flow mal-distributions are generally represented [99]. Different analyses in the literature consider a probability distribution of the desired property, generally fibre radius and membrane thickness. The distribution is included into the model formulation and generally applied to analytical solutions of the problem, such as reported by Wickgrmasinhe et al. [22] and Crowder and Cussler [23]. Lemanski and Lipsicomb [135] present a study applied to gas separation where the effect of fibre diameter, permeance and selectivity standard deviation are analysed using a normal distribution. A statistical approach is also used to account for irregular fibre packing, as reported by Wu and Chen [24] who divide the cross-sectional area according to a Voronoi tessellation.

With the aim of giving more detailed simulations and possible guidelines for industrial module design, the implemented 2D analyses can also account for module defects. The proposed approach to the problem is based on a Gaussian distribution of a population of a set property with the required average and variance. A random generation algorithm based on an Irvin-Wall distribution (a 12^{th} order approximation of the Gaussian distribution [136]) is set up to generate an array of properties with the required specifications. For example, each value of channel thickness in a spiral wound module corresponds to a point in the discretization used for the numerical resolution.

Considering a Gaussian radius distribution in a hollow-fibre module as reported in Eq. (2.97), different fibre radius will affect both area density and volume fraction as evident from Eq. (2.98) and Eq. (2.99), where $\mathbf{r}$ is the external fibre radius. Shell side void fraction $\boldsymbol{\Delta}^*$, area density $\boldsymbol{\sigma}$ and fibre fraction $\boldsymbol{\Delta}$ are function of fibre radius as well.

$$g = f(r, r_{avg}, s^2) = \frac{e^{-\frac{1}{2}\frac{(r-r_{avg})^2}{s^2}}}{\sigma\sqrt{2\pi}} \tag{2.97}$$

$$\sigma(< r >) = \left[\frac{m^2}{m^3}\right] = \frac{A}{V} = \frac{N_f 2\pi}{W H} < r > \tag{2.98}$$

$$\Delta(< r >) = \left[\frac{m^3{}_{bore}}{m^3{}_{shell}}\right] = \frac{N_f \pi}{W H} < r >^2 \tag{2.99}$$

Due to module defects, different velocities will be encountered in both bore and shell sides and, therefore, the flow distribution will depend on the position along the module.

An amount of runs is set and the results are analysed using statistic theory. A level of confidence of 95 % is assumed according to a t distribution table for a double-tailed distribution [137]. The average value is calculated and the standard deviation assuming n number of runs is determined according to equation Eq. (2.100),

$$t = \frac{\mu - x}{\sigma / \sqrt{n}} \tag{2.100}$$

In the case of cross-flow model, a channel thickness normal distribution is assumed and the statistical analysis is carried out in analogy to the hollow-fibre case.

Chapter 4: Single-stage simulations

In the previous Chapter the models and their numerical resolution were presented. The attention is now focused on the results from single-stage simulations. Carbon capture and natural gas applications are investigated to test the implemented models under different operating conditions.

4.1 Plug-flow and cross-flow models for carbon capture applications

In the first part of this discussion simulations with no pressure drops and ideal gas behaviour are carried out. Membrane area is the main design parameter without focusing – at this stage – on module geometry.

The models included in this section have been presented in Chapter 3: well-mixing on both sides, non-dispersed plug-flow and cross-flow. These simulations represent the starting point for the multi-stage design which will be presented in Chapter 5.

The feed gas chosen for the single-stage simulations corresponds to a flue-gas from a coal-fired power plant (DOE case 9 [24] – subcritical coal-fired power). Feed gas properties are reported in Table 4.1.

Molar Flow rate	$2.0 \cdot 10^4$ mol / s	
Molar fractions	0.15	CO_2
	0.74	N_2
	0.02	O_2
	0.09	H_2O

Table 4.1: Flue gas properties.

The assumed material presents a CO_2 permeance of 5000 GPU – which is currently a research target for carbon capture applications [49, 54, 78] – and a selectivity CO_2/N_2 of 50 [39]. CO_2/O_2 and CO_2/H_2O selectivities are assumed, respectively, as 15 and 1. Feed pressure is set to 200 kPa and permeate pressure to 20 kPa [39]. Since the adopted membrane is CO_2-selective, CO_2 recovery and purity are evaluated and compared.

The plots showing the partial pressure profiles obtained from the plug-flow models are shown in Figure 4.1 and Figure 4.2. Membrane area is fixed to 3.0×10^5 m^2 and the flue gas is reported in Table 4.1.

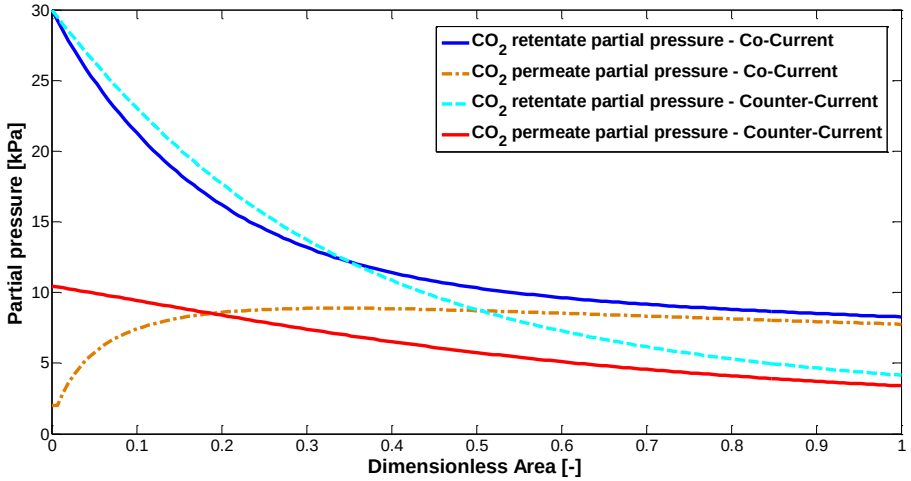

Figure 4.1: One-dimensional co-current and counter-current CO_2 partial pressure profiles. CO_2 permeance = 5000 GPU, CO_2/N_2 selectivity = 50, CO_2/O_2 selectivity = 15 and CO_2/H_2O selectivity = 1.

The difference in the resolution between co- and counter-current flow patterns is the sign of the permeate flow rate. As expected from an analogy with heat exchanger design, counter-current results in the best option with a better exploitation of the membrane area, as shown in Figure 4.1.

A key option is the sweep, a stream with a low concentration of the most permeable components sent to the permeate side inlet which lowers the partial pressure, therefore improving the driving force for the separation. Different sweep streams can

be used and this is an important process parameter in a multi-stage design, where recycles from different stages can also be adopted. High recoveries can be achieved by changing the sweep flow rate keeping small areas, making this solution ideal for high-recovery stages. For the purpose of these simulations, retentate sweep is adopted as reported by Merkel et al. [39]. An example of partial pressure profile with 10 % of the total retentate flow as sweep compared to the dead-end counter-current case is shown in Figure 4.2. It is possible to point out the dramatic improvement of the partial pressure profile comparing the two cases.

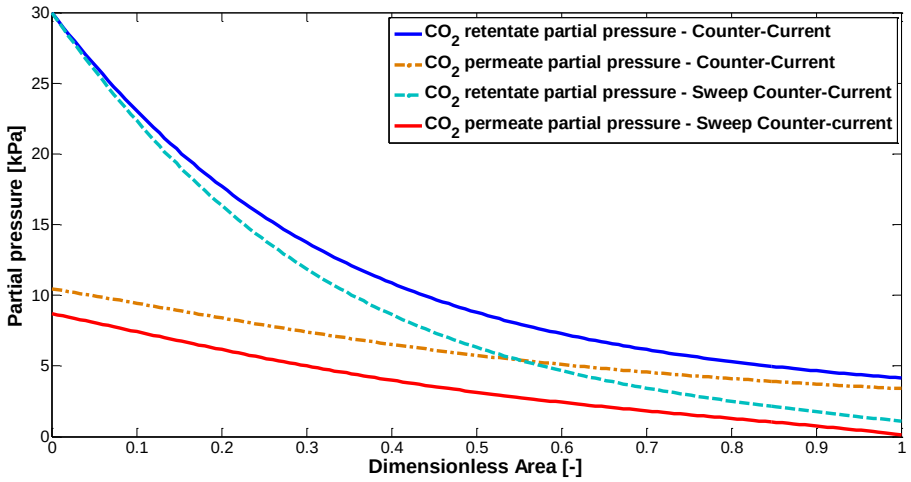

Figure 4.2: One dimensional counter-current and sweep counter-current CO_2 partial pressure profiles. CO_2 permeance = 5000 GPU, CO_2/N_2 selectivity = 50, CO_2/O_2 selectivity = 15 and CO_2/H_2O selectivity = 1.

However, the increase of recovery using sweep affects the purity of the permeate side, following the typical trade-off between purity and recovery.

In Figure 4.3 a partial pressure profile for the 1D cross-flow model is shown. Simulations achieving a recovery of 90 % and 10 % are reported to show the different trend, linear in the low-recovery case. The x-axis is reported in terms of dimensionless area, similarly to the non-dispersed plug flow analysis.

In Figure 4.4 a 2D cross-flow partial pressure profile for the permeate side is presented, corresponding to the same conditions as Figure 4.1 and Figure 4.2. In

order to keep the membrane area as design parameter, a w/l ratio of 25 is fixed and the leaf dimensions are consequently calculated. Module geometry will become significant when pressure drops will be included and this will be shown in the next paragraphs.

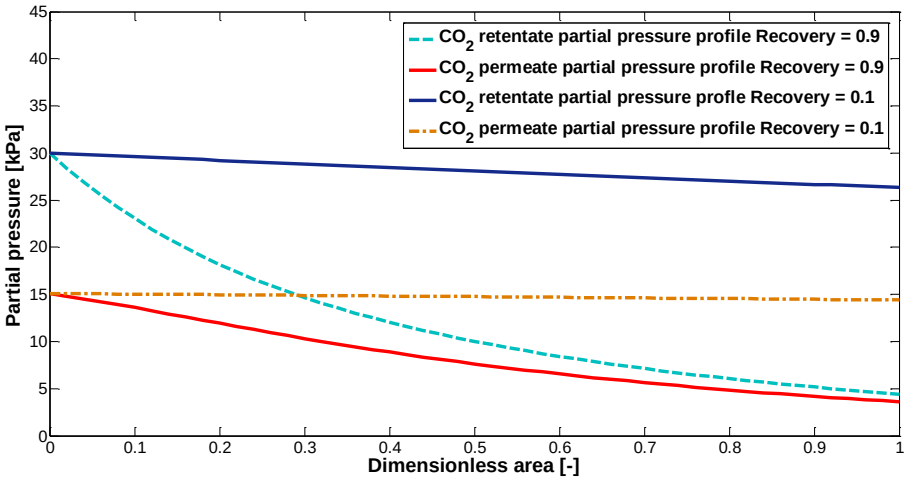

Figure 4.3: 1D CO_2 partial pressure profile (CO_2 recovery = 0.9 and CO_2 recovery = 0.1). CO_2 permeance = 5000 GPU, CO_2/N_2 selectivity = 50, CO_2/O_2 selectivity = 15 and CO_2/H_2O selectivity = 1.

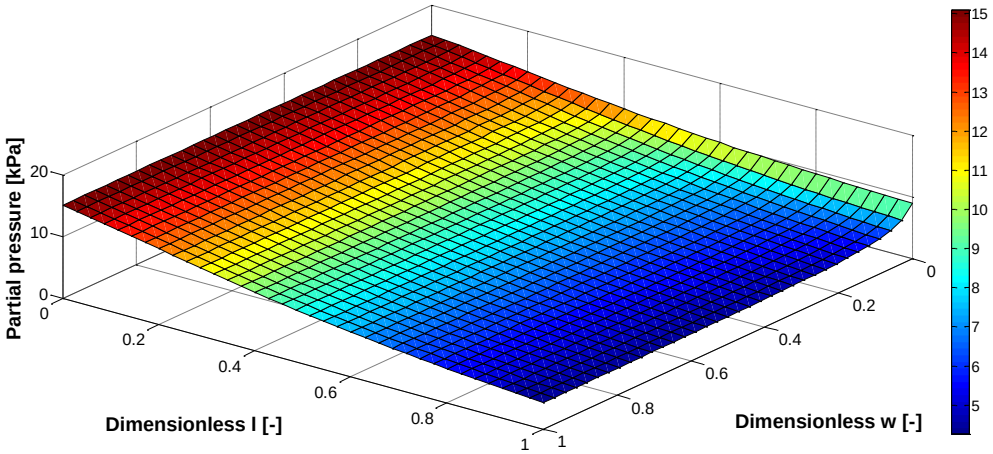

Figure 4.4: Example of 2D cross-flow CO_2 partial pressure profile for permeate side.

An analysis of the results obtained by comparing the different models is shown in Figure 4.5, at a fixed membrane area of 3.0×10^5 m^2. The parameters used for the comparison are stage cut, CO_2 purity and recovery. The 2D cross-flow model is used in all the comparisons to be consistent with the developed bi-dimensional analysis and it is written in terms of molar flow: consequently, no channel thickness is required. Simulations using sweep are run assuming 10 % as sweep as in Figure 4.2. Despite not corresponding to a flow pattern with a real application in industrial separation modules, the CSTR model is included to have an idea of the different predictions among the different models. It is in-fact based on a uniform concentration on both sides which is unrealistic in industrial modules. However, it can be a useful tool for having an initial estimation of the separation.

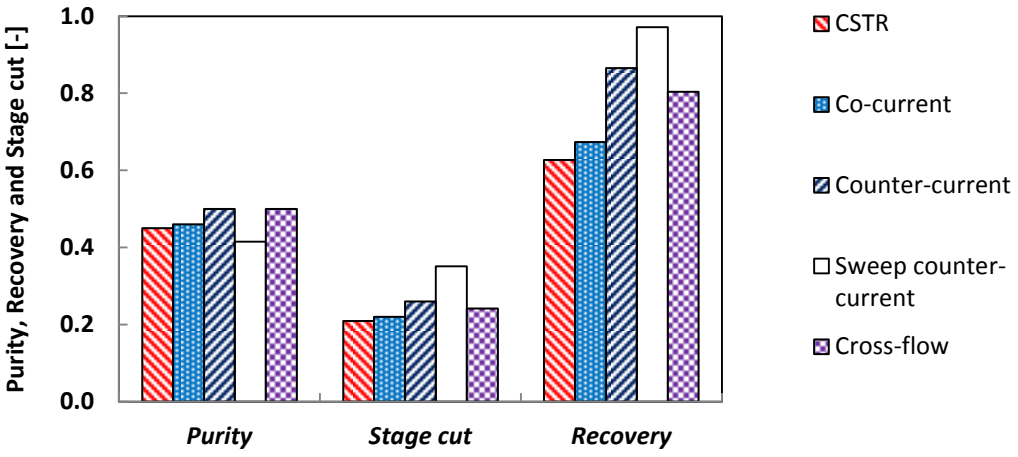

Figure 4.5: Overall comparison among the models – fixed membrane area. CO_2 permeance = 5000 GPU, CO_2/N_2 selectivity = 50, CO_2/O_2 selectivity = 15 and CO_2/H_2O selectivity = 1.

According to the results reported in Figure 4.5, counter-current simulations predict a higher purity and recovery than co-current: this result can be expected in analogy with heat exchanger design [138]. Cross-flow results in a slightly higher purity than counter-current but with a lower recovery and stage cut. In order to have an additional comparison among the models, an analysis carried out by fixing the stage cut to 0.3 is presented in Figure 4.6, where the areas are dimensionless with respect to the well-mixing case.

Considering the overall performances in Figure 4.5 and Figure 4.6, counter-current/sweep and cross-flow give the most promising results in terms of, respectively, recovery and purity. In the case of counter-current, the potential of modifying an additional design parameter - the sweep stream, both in terms of composition and flow rate - makes it ideal for high-recovery stages, due to the decrease in area compared to the dead-end case (configuration where no permeate sweep is used).

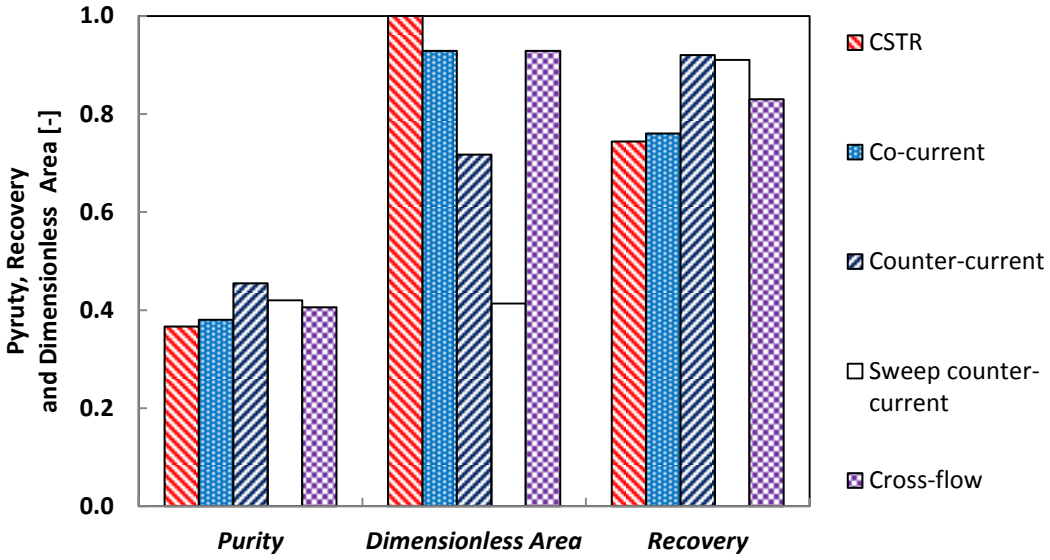

Figure 4.6: Overall comparison among the models - fixed stage cut. CO_2 permeance = 5000 GPU, CO_2/N_2 selectivity = 50, CO_2/O_2 selectivity = 15 and CO_2/H_2O selectivity = 1.

After identifying the two optimal flow patterns, a comparison between cross-flow and counter-current is now presented. An analysis of Figure 4.5 shows that the cross-flow model predicts a lower recovery than counter-current and approximately the same purity. Considering the same membrane area, the counter-current configuration has the opportunity to increase the recovery by increasing the sweep flow despite achieving lower purity than cross-flow. The aim is to achieve high separation performances in terms of both recoveries and purities by keeping relatively small membrane areas, not to penalise the capital cost contribution and to minimize the footprint of the separation. Two limiting cases are chosen: a high recovery and a high purity application. This analysis is important in terms of multi-

stage designs where different module configurations - therefore different flow patterns - can be chosen to optimise the overall performances.

In Figure 4.7 CO_2 recovery is fixed at 90 % and the effect on area and purity is investigated. Since the aim is to achieve high recoveries keeping low areas, it is evident that the sweep option is the best one, despite predicting a lower purity.

Figure 4.8 shows the results of simulations carried out by keeping CO_2 purity fixed to 65 %, which corresponds to a high-purity stage considering the membrane characteristics and the feed composition. In this case cross-flow is the best option in terms of membrane area (approx. - 30 %), despite a slightly lower recovery (- 3 %) compared to counter-current. The sweep option, despite having the smallest area, is not optimal in terms of final purity: the sweep flow rate reduces to zero and the stage results in a dead-end counter-current. Therefore, it is not shown in the plot.

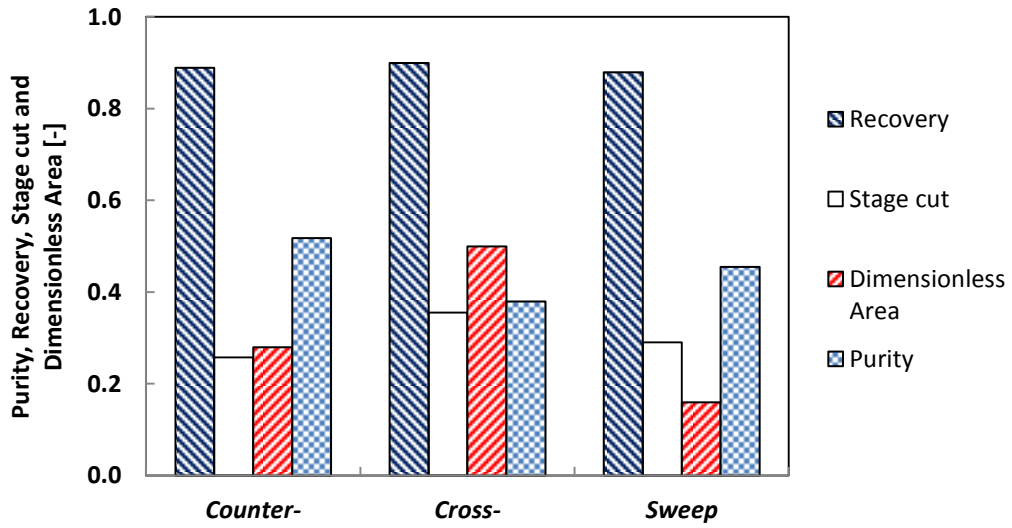

Figure 4.7: Cross-flow vs. counter-current - high recovery. Membrane area is dimensionless with respect to the well-mixing case. CO_2 permeance = 5000 GPU, CO_2/N_2 selectivity = 50, CO_2/O_2 selectivity = 15 and CO_2/H_2O selectivity = 1.

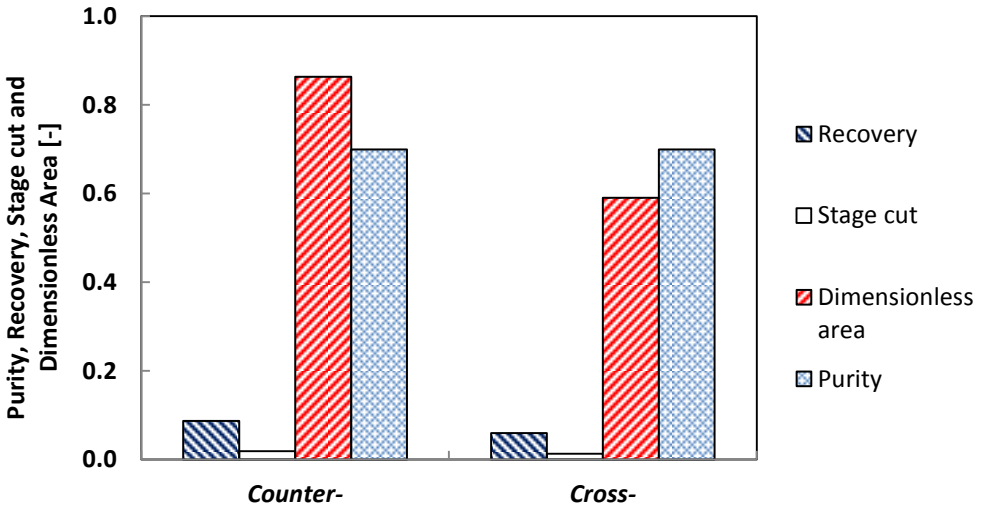

Figure 4.8: Cross-flow vs. counter-current – high purity. Membrane area is dimensionless with respect to the well-mixing case. CO_2 permeance = 5000 GPU, CO_2/N_2 selectivity = 50, CO_2/O_2 selectivity = 15 and CO_2/H_2O selectivity = 1.

In conclusion, the strategy in a multi-stage scheme will be cross-flow for high-purity stages and sweep counter current for high-recovery ones.

4.2 Hollow-fibre simulations

In Table 4.2 the module characteristics chosen for the hollow-fibre simulations are reported and they correspond to the ones presented by Coker et al. [105]. This is one of the few cases in the literature where it is possible to replicate the simulations since all the required data are reported. These module parameters give an area density of 6640 m^2/m^3, in line with standard commercial hollow-fibre modules which are in the range 4000 - 10000 m^2/m^3 [29, 86]. A value of 0.5 for Δ is reported in the original paper and radius and porous support thickness can also be considered as realistic for commercial permeators.

Fibre internal radius $\mathbf{r_{in}}$	75 μm
Fibre external radius $\mathbf{r_{out}}$	150 μm
Fibre fraction **Δ**	0.5
Area density **σ**	6640 m^2/m^3
Module length **L**	0.8 m
Module width **W** and height **H**	0.266 m

Table 4.2: Hollow-fibre module characteristics [105].

It is also important to point out the criteria adopted in the simulations. Coker et al. [105] present the results in terms of Flow rate/Membrane Area (F/A), expressed in $[m^3(STP)/(m^2 \cdot h)]$. These units will be used in the plots presented in this thesis to be consistent with the original publication (1 $m^3(STP)/(m^2 \cdot h)$ = 0.012 $mol/(m^2 \cdot s)$). Depending on the inlet flow rate – and consequently velocity – the separation behaves differently. High values of F/A correspond to higher inlet velocities, lower specific area available for the separation and this consequently leads to low recovery stages. On the other hand, a low F/A corresponds to high-specific areas and, therefore, a high-recovery application. However, this might lead to higher non-isothermal effects due to the high separation efficiency of the module. Due to the Joule-Thomson effect during permeation, temperatures which are below the dew point of the mixture can be achieved, causing undesirable condensations inside the module [108].

To be able to compare with the literature data and validate the models, the results are reported in terms of F/A and natural gas separation is initially simulated in order to validate the 1D model. Carbon capture applications and parameters of a CO_2-selective membrane are then considered.

4.2.1 1D model validation: natural gas separation

Membrane separation is widely adopted for natural gas separations, where gases as CO_2, H_2O and impurities are separated from the gas stream in order to achieve the required specifications for pipeline delivery. This separation is characterized by feed pressures above 30 bar and the enriched methane stream is at the retentate side in order to avoid its recompression [26]. Therefore, membranes are selective with respect to CO_2 and other components to be separated.

The first step in this analysis consists in the simulation of a simple Joule-Thomson expansion. An inlet pressure in the range 2 - 6 MPa bar and a temperature of 323 K are set and the discharge pressure is fixed to 0.1 MPa. The results for a gas containing 90 % CH_4 and 10 % CO_2 (mol/mol) are compared with Honeywell UniSim® Design using the same EOS (Peng Robinson). In Figure 4.9 the outlet temperature with respect to the inlet pressure is shown and a good agreement is reported between the in-house simulations and the commercial software.

For CO_2/CH_4 separation the two different models are run and the results are compared with the available literature. Considering the module assumptions previously discussed, the isothermal results are presented in Figure 4.10. The feed gas (shell-side feed) contains 10 % CO_2 and 90 % CH_4, feed pressure is 5.8 MPa bar and permeate pressure is 0.2 MPa [139]. The membrane has a CO_2 permeance of 22.7 GPU and a CH_4 permeance of 0.7 GPU. The simulations carried out in this study show good agreement with the original simulations of Coker et al [105].

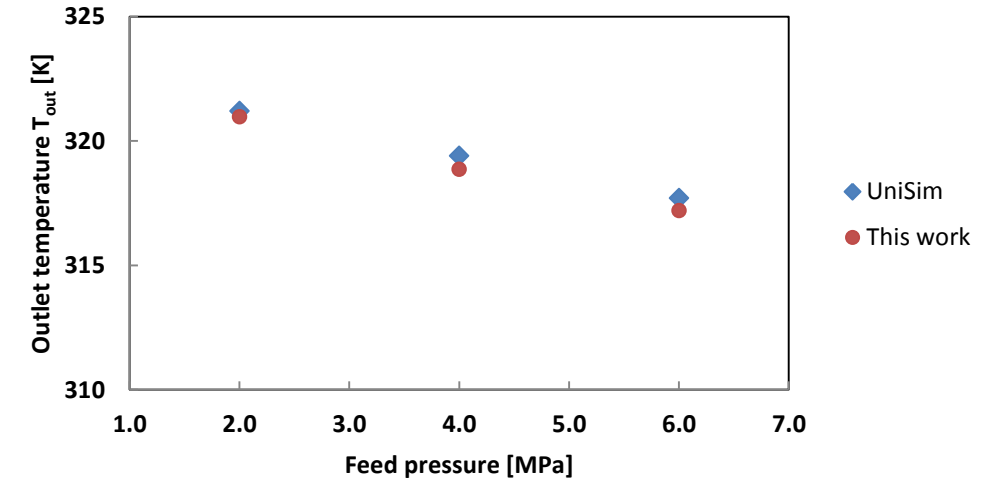

Figure 4.9: Joule-Thomson expansion - outlet temperature vs. feed pressure.

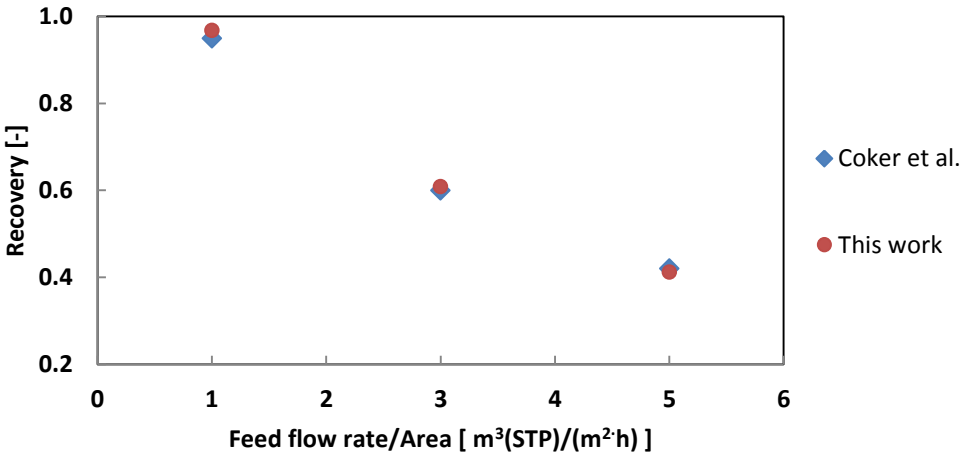

Figure 4.10: Isothermal validation for hollow-fibre one-dimensional model. CO_2 permeance = 23 GPU, CO_2/CH_4 selectivity = 32.

In Figure 4.11 simulations under the same process conditions using the non-isothermal model are also presented and the results show good agreement. It has to be pointed out that shell-side pressure drops are not considered in order to be consistent with the original analysis.

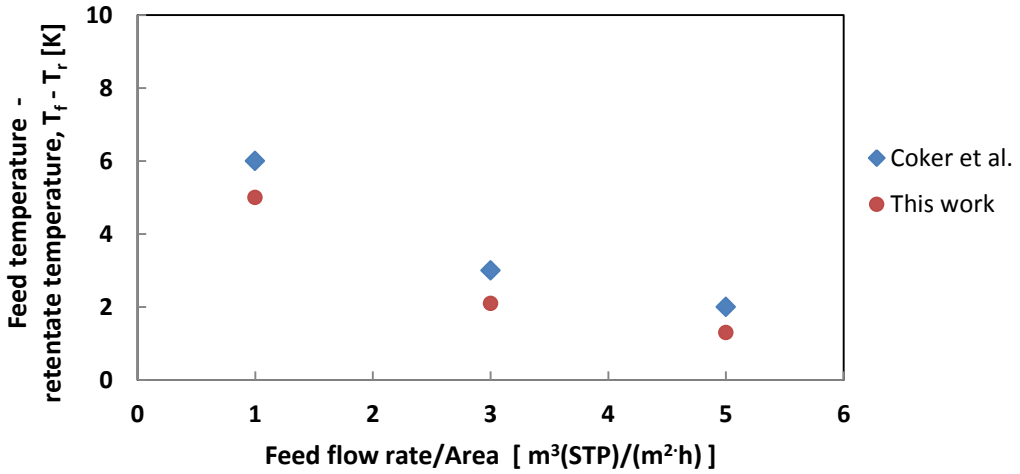

Figure 4.11: Non-isothermal validation for hollow-fibre one-dimensional model. CO_2 permeance = 23 GPU, CO2/CH4 selectivity = 32.

In Figure 4.12 a temperature profile inside the module is presented. The gas expands while permeating through the membrane and it consequently cools down due to the Joule-Thomson effect. A decrease in temperature of the retentate stream is also encountered because of the heat exchange between the two sides.

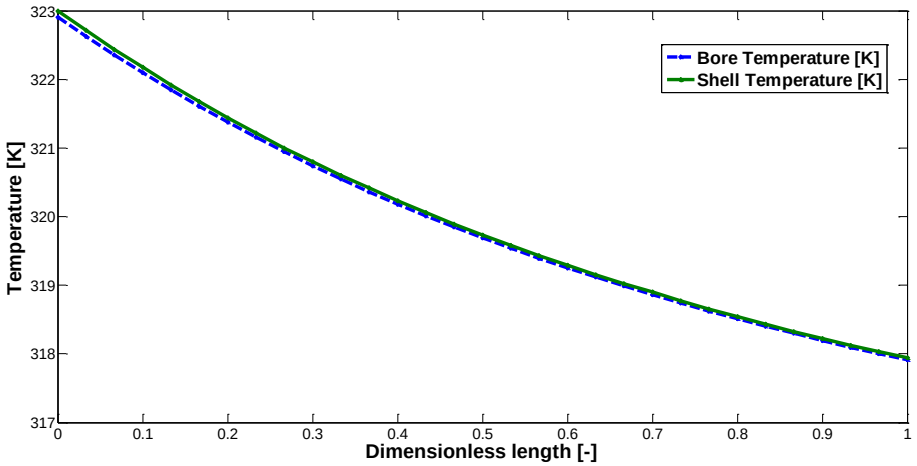

Figure 4.12: Temperature profile along the module length for both shell (retentate) and bore (permeate) sides. CO_2 permeance = 23 GPU, CO_2/CH_4 selectivity = 32.

4.2.2 Carbon capture 1D simulations

The attention is now focused on carbon capture applications. The module parameters are assumed from Coker et al. [105] and single-stage simulations are run in order to carry out a comparison with the previously implemented non-dispersed plug-flow models. In particular, the difference in prediction among the different models is under investigation, identifying the possible effect of pressure drops and non-ideal/non-isothermal behaviour.

A bi-component mixture 15 % CO_2/ 85 % N_2 (mol/mol) is assumed, the membrane properties are the same as the carbon capture simulations in Paragraph 3.1 and the feed pressure is 200 kPa. Permeate pressure is fixed to the permeate side outlet (at 20 kPa): therefore, a higher pressure is expected at the sweep side due to pressure drops.

Simulations are carried out with the same criteria as the ones presented in Figure 4.10 and Figure 4.11: non-dispersed plug-flow (base model) is included and the one-dimensional hollow-fibre simulations are run with and without pressure drops. The results are reported in Figure 4.13 in terms of CO_2 purity and recovery for dead-end counter-current case in order to be consistent with the original analysis.

First of all, non-dispersed plug-flow and hollow-fibre simulations with no pressure drops give very close predictions. This is an important indication in terms of process simulations: membrane area is sufficient to have an initial indication of the performances for a certain module. If more realistic simulations are run and pressure drops are considered, a difference in purity is encountered for low F/A, consequently for a high-recovery application. On the other hand, a dramatic difference in recovery is shown for high F/A ratios. Pressure drops for both sides are reported in Figure 4.14, where it is possible to identify a maximum in permeate pressure drops which corresponds to the F/A value where the velocity inside the fibres is higher. A comparison between Figure 4.14 and Figure 4.13 shows that for low F/A the predominant effect is related to the bore-side contribution, while for higher F/A also shell-side pressure drops become significant.

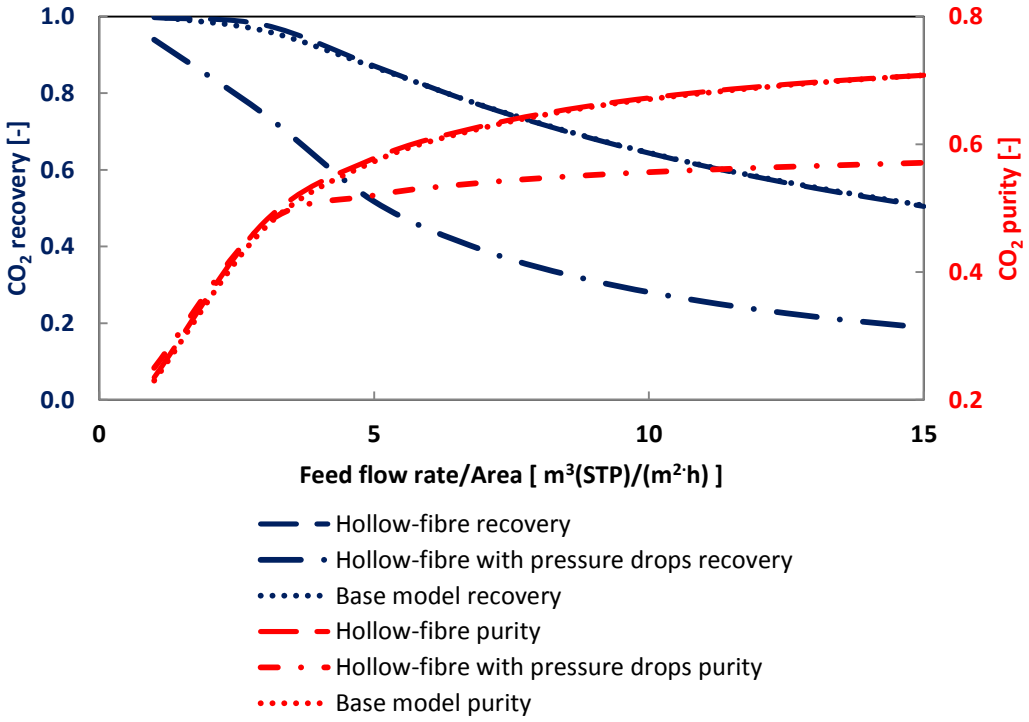

Figure 4.13: Purity and Recovery vs. Feed flow rate/area. CO_2 permeance = 5000 GPU, CO_2/N_2 selectivity = 50.

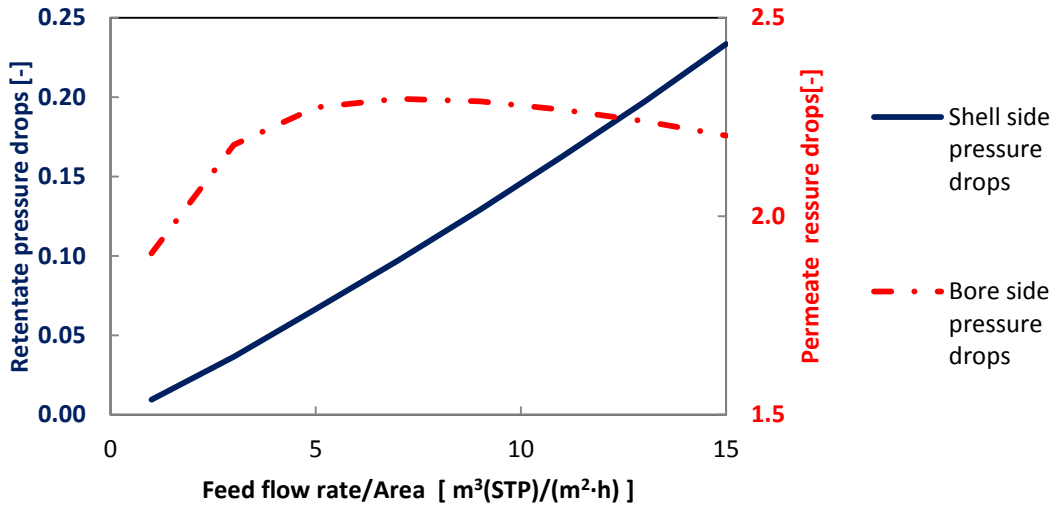

Figure 4.14: Pressure drops on retentate and permeate sides for the pressure drops cases. CO_2 permeance = 5000 GPU, CO_2/N_2 selectivity = 50.

Due to their higher area density compared to other module configurations, hollow-fibre modules can be adopted for high-recovery stages which represent the largest areas in a multi-stage design. Considering a low F/A in Figure 4.13 which corresponds to a high-recovery application, no significant effects should be expected in terms of purity compared to the relevant difference in CO_2 recovery. It should be pointed out that a low F/A - and therefore a relatively low inlet flow rate - is also required not to have significant shell-side pressure drops, as shown in Figure 4.14. For example, assuming that a recovery of 90 % is required, simulations using non-dispersed plug-flow model (base model in Figure 4.13) achieve this target at approximately F/A = 5. If pressure drops are considered, a value of F/A = 2 is required: assuming the same flow rate, this implies an effective membrane area 2.5 times higher than the base-case simulation.

An interesting point of discussion is the asymptotic trend encountered in Figure 4.13 for CO_2 purity, particularly for the case with pressure drops. Permeate conditions remain constant even though the inlet flow rate is increased and this leads to a limiting case. In particular, a difference of approximately 10 % in CO_2 purity is obtained when pressure drops are included. Considering the simulations with momentum balance, a lower effective pressure ratio is expected due to pressure drops. The asymptotic trend suggests that for high F/A the module is expected to work under pressure ratio limited regime. This is a limiting case in membrane separations if the pressure ratio is significantly lower than the selectivity, as in the reported simulations. Therefore, the maximum achievable permeate composition can be related to the pressure at both sides [26]. Assuming low stage cut, no significant change in retentate composition, permeation through the membrane can happen only if the partial pressure in the retentate is higher than the partial pressure in the permeate, as reported in Eq. (4.1). Rearranging Eq. (4.1) and using the pressure ratio $\boldsymbol{\theta}$ as ratio between retentate and permeate pressure, Eq. (4.2) needs to be satisfied. Therefore, the maximum achievable purity in this limiting case is strictly related to the pressure at both sides.

$$P_r \cdot x_{if} > P_p \cdot x_{ip} \tag{4.1}$$

$$x_{ip} < \theta\, x_{if} \tag{4.2}$$

Despite the assumed pressure ratio of 10 did not seem to lead to this case, pressure drops are expected to reduce the effective pressure ratio of the system and, therefore, to affect the separation behavior. This is particularly important for carbon capture applications since the maximum achievable purity of the first stage - which has to cope with the lower CO_2 composition - can be affected by the process conditions. Merkel et al. [39, 56] reported that membranes for carbon capture are expected to work under this regime since a pressure ratio in the range 5 – 10 is required to achieve an optimal compromise between membrane area and energy consumption. It is shown here that pressure drops should be carefully taken into account in terms of process simulations and this analysis can be a useful tool to estimate the optimal feed flow for a given module to achieve a target purity and/or recovery.

A modelling approach using the base model (non-dispersed plug-flow) might lead to an under-estimation of the required membrane area. It is also evident from Figure 4.14 that shell-side pressure drops have to be taken into account for high F/A ratios. This will be discussed further in the 2D compartmental analysis, where more detailed correlations are used.

All the simulations have been run assuming Virial EOS in order to achieve more realistic predictions. However, no significant effect is identified compared to ideality due to the low-pressure applications. In Figure 4.15 the difference between feed and retentate temperature is also reported in analogy with Figure 4.11: this confirms that no significant temperature changes are expected in carbon capture applications, even for high recoveries (low F/A in the plot).

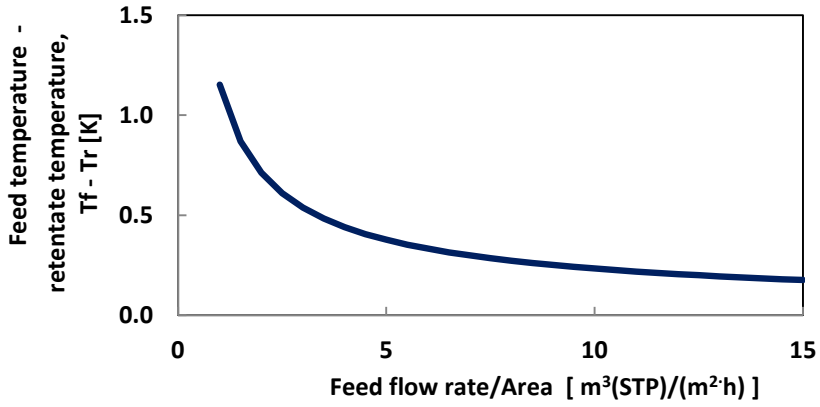

Figure 4.15: Feed temperature – retentate temperature (T_f-T_r) for hollow-fibre simulations for carbon capture simulations. CO_2 permeance = 5000 GPU, CO_2/N_2 selectivity = 50.

Simulations using sweep are also considered, since it guarantees high recoveries by keeping relatively low membrane areas. In Figure 4.16 CO_2 purity is reported using 10% of retentate flow rate as sweep, in analogy with the results reported in paragraph 3.1. The trend in product recovery is similar to Figure 4.13, while in the case of purity a trend with a maximum is identified. This can be attributed to the predominant contribution from bore-side pressure drops (Figure 4.14) which is higher due to the increased velocity compared to the base case.

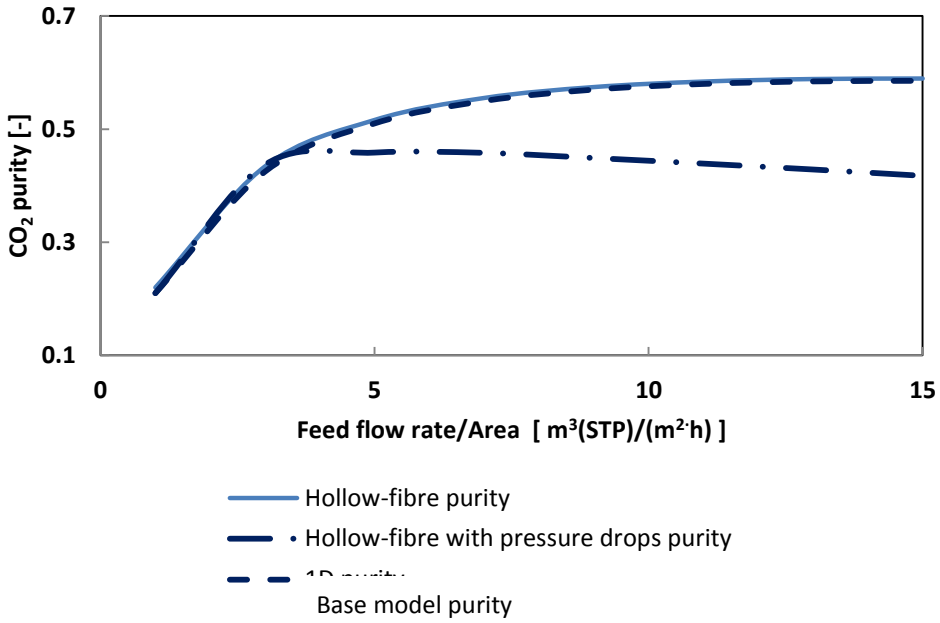

Figure 4.16: Purity vs. Feed flow rate/Area - simulations with 10 % retentate flow rate as sweep. CO_2 permeance = 5000 GPU, CO_2/N_2 selectivity = 50.

4.2.3 Compartmental modelling

Simulations for the bi-dimensional compartmental approach are run both with and without pressure drops and they are compared to the one-dimensional analysis.

In Figure 4.17 an example of partial pressure profile for the shell (feed) side is reported. Two baffles are simulated and, consequently, three equally sized compartments. The discontinuity on the y direction is due to the mixing between adjacent sections.

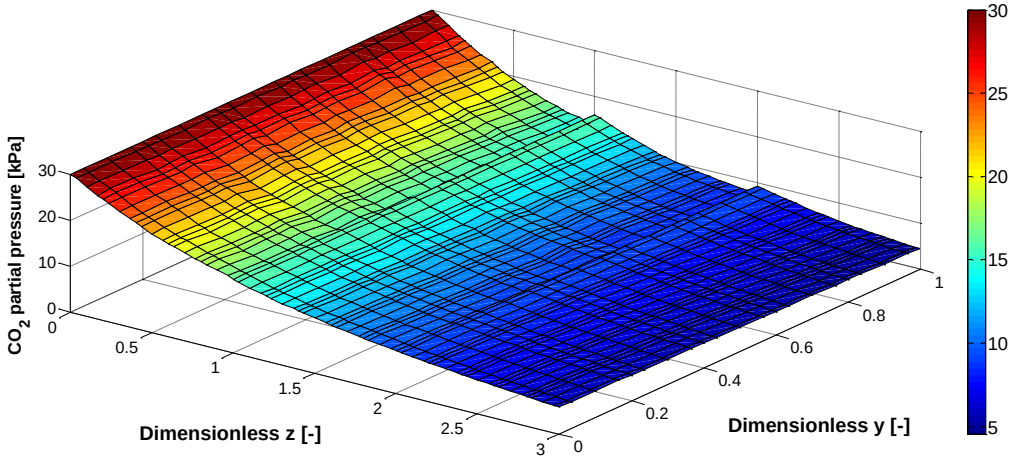

Figure 4.17: Example of shell-side CO_2 partial pressure profile - compartmental model.

Simulations are run considering the same module characteristics as the previously discussed 1D hollow-fibre results. A feed flow rate of 10 mol / s is chosen, corresponding to a high-recovery application in Figure 4.13. The pressure ratio is fixed to 10 as in the simulations reported in the previous section (200 kPa at the retentate side and 20 kPa the permeate side). However, feed inlet and outlet are now perpendicular to the bore-side y direction. The same shell side length path as the 1D case is assumed (0.8 m) but divided into three compartments and same cross-sectional area for the feed side is also considered in this comparison.

Initial simulations are carried out considering the dead-end case in overall co- and counter-current flow patterns assuming no pressure drops. The results in terms of recovery, purity and stage cut are reported in Figure 4.18, where 1D hollow-fibre and 1D cross-flow results are also included to evaluate the different prediction among single and combined flow patterns. As expected, 2D counter-current results in a better overall recovery than co-current. The 1D cross-flow simulations present an intermediate recovery between 1D and 2D counter-current cases and a slightly higher overall purity. No significant differences in stage cut are encountered among the different cases. Both a lower recovery (-10 %) and purity (- 5 %) are shown in the 2D hollow-fibre counter-current compared to the 1D case.

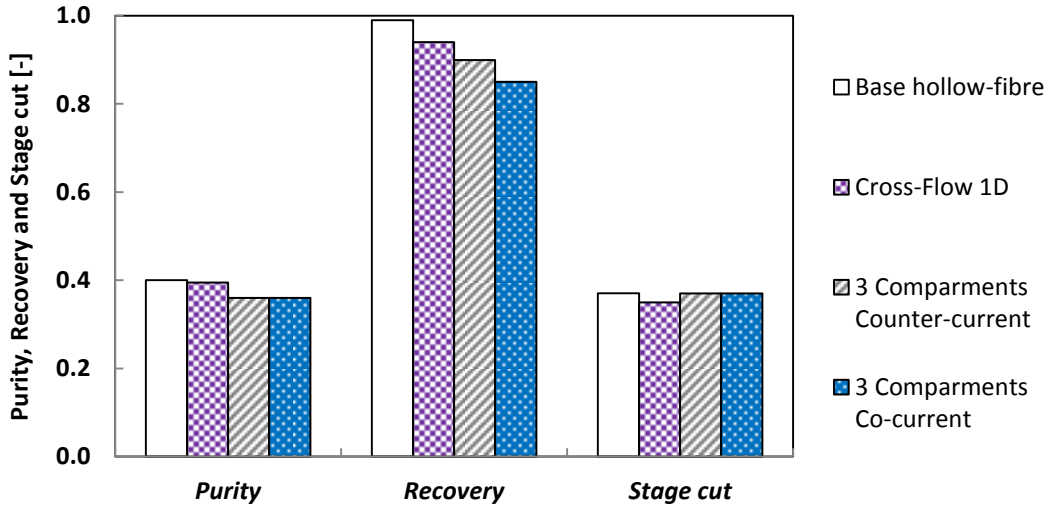

Figure 4.18: Comparison among 1D and 2D hollow-fibre simulations with NO pressure drops. CO_2 permeance = 5000 GPU, CO_2/N_2 selectivity = 50.

An important point of discussion is the analysis of the results with pressure drops. As presented in Chapter 2, the selected approach starts from the available correlations from heat-exchangers design: assuming a square tube layout, Kern and Bell-Delaware methods are adopted. The idea is to identify the effects of such a key contribution which is expected to significantly affect the performances.

In Table 4.3 the results assuming pressure drops on both sides are presented, where a square tube layout is assumed. Hagen-Poiseuille, Kern and Delaware correlations are adopted for the shell side and the 1D case is also included. First of all, it is important to point out the dramatic difference in recovery (at least – 18 %) among 1D and 2D predictions, even when shell side pressure drops are approximately the same as in the first two lines, where Hagen-Poiseuille dependence is assumed. This is mainly due to the combined flow pattern and it confirms the results with no pressure drops in Figure 4.18, where the 2D simulation showed lower recovery than the 1D cases. Therefore, assuming the same shell path length and a realistic cross-flow flow pattern, the 1D counter-current is expected to underestimate membrane area for a certain recovery. Additionally, no significant effect in purity is encountered (maximum – 2 %) and this is probably due to the cross-flow contribution. A dramatic difference in pressure drops is encountered among the three different methods

adopted in the bi-dimensional simulations. Kern method is expected to overestimate pressure drops in heat exchanger design and it consistently gives the higher value. On the other hand, Hagen-Poiseuille relationship predicts significantly lower pressure drops than the other cases, but it is also based on flow inside a pipe which is not encountered on the shell side. Bell-Delaware is generally considered as more realistic indication for heat exchanger design [125] and it is assumed as a consistent correlation for the reported simulations. Therefore, it is likely to expect pressure drops in the range 10 – 15 kPa (100 - 150 mbar), which are 5 - 10 % the feed pressure. It is also important to point out that the increased shell side pressure drops (from Hagen-Poiseuille to Bell-Delaware methods) do not seem to significantly affect the performances in terms of separation. Therefore, the main repercussion of shell side pressure drops can be identified in increased energy consumption for additional recompression of the feed. This also suggests that shell-side pressure drops for low F/A can be significantly higher than the values reported in Figure 4.14.

	Recovery [-]	**Purity [-]**	**Shell side pressure drops [kPa]**
1D Hollow fibre with pressure drops	0.881	0.429	5.0
2D Hollow-fibre, Hagen-Poiseuille shell side	0.705	0.409	4.3
2D Hollow-fibre, Bell-Delaware shell side	0.701	0.413	13.3
2D Hollow fibre, Kern shell side	0.666	0.421	35.6

Table 4.3: Simulations with pressure drops using different correlations. Comparison among 1D model and 2D model with different shell-side pressure drop correlations. Bore side pressure drops follow Hagen-Poiseuille relationship for all cases. CO_2 permeance = 5000 GPU, CO_2/N_2 selectivity = 50.

Module design is also analysed and different tube layouts are considered, following heat exchanger correlations. A square, 30° and 45° tube layouts are simulated assuming the same membrane area and, therefore, the same number of fibres. A schematic representation is reported in Figure 4.19

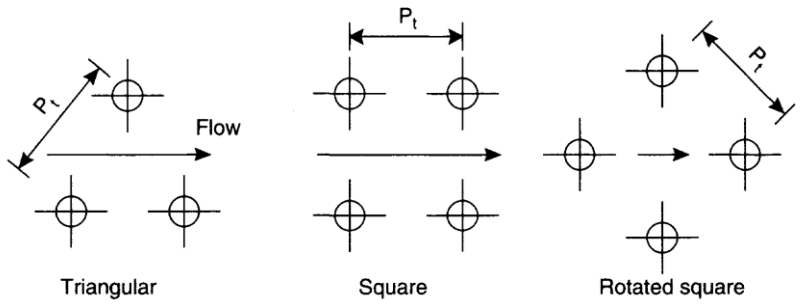

Figure 4.19: Representation of different tube layouts from Sinnot et al. [117]. From left to right: 30°, 90° (square layout) and 45°. Legend: P_t is the tube pitch.

Since the total number of tubes is dependent on the tube geometry, if the same membrane area is assumed a decreased shell side equivalent diameter is expected from the 30° case and, consequently, lower shell path length (70 % the base case). This also affects the values of σ and Δ which are dependent on the tube geometry as well. In analogy with heat exchanger operation where pressure drops are fixed, simulations are now run assuming a value of 10 kPa (100 mbar) of shell side pressure drops for all cases. The results are reported in Figure 4.20 in terms of purity, recovery and ratio between the CO_2 separated and membrane area (Permeate CO_2/Membrane Area in the plot), a parameter which gives an idea of the module separation performances. The higher this value, the better exploitation of the area is achieved; considering a set of modules working in parallel, additional units should be expected for the lower F_{PCO_2}/A cases. It is possible to identify the 30° case as the worst overall performances in terms of F_{PCO_2}/A since a lower flow rate is required not to increase pressure drops. As expected, opposite trends in recovery vs. purity are also encountered. These simulations are an example of evaluation of different module configurations and they confirm the best overall performances of a square tube layout in terms of overall separation efficiency.

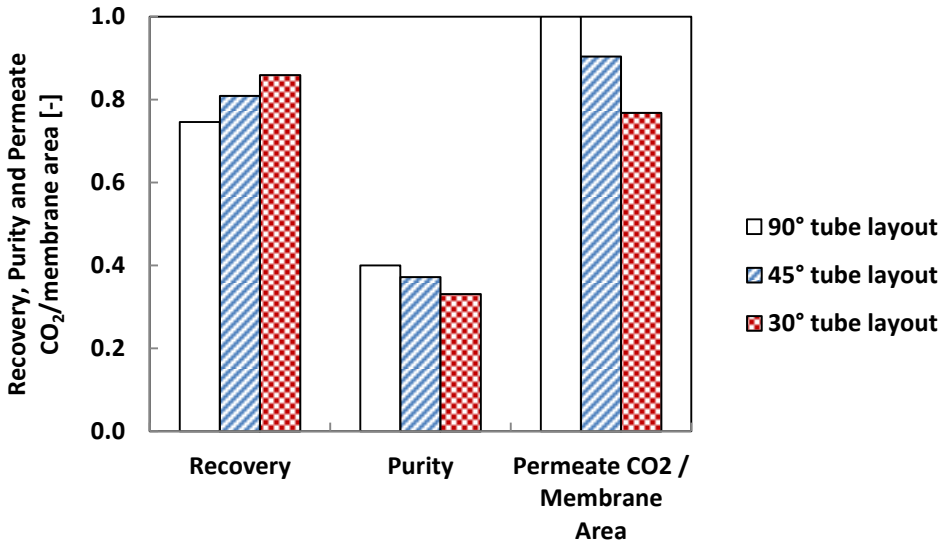

Figure 4.20: comparison of the results with different tube layouts assuming the same pressure drops (10 kPa = 100 mbar) and same membrane area. Permeate CO_2/membrane area is dimensionless with respect to the 90° tube layout case. CO_2 permeance = 5000 GPU, CO_2/N_2 selectivity = 50.

A final sensitivity analysis is also conducted with respect to fibre radius. This parameter is chosen since it is a key contribution for pressure drops, particularly on the bore side. Total area and fibre void fraction are kept constant, a feed flow rate of 10 mol/s is assumed and Bell-Delaware correlation is adopted for the shell side. Since membrane area is fixed, the external dimensions are dependent on the assumed fibre radius which is considered in the range 100 - 250 μm. These values have been chosen since they give realistic area densities in the range 4000 - 10000 m^2/m^3. In Figure 4.21 the results are reported in terms of purity, recovery, shell side pressure drops and module volume (dimensionless with respect to the 250 μm case). Purity is not affected by the different fibre radius while a dramatic change in recovery is observed, due to the lower permeate pressure drops and, therefore, higher overall flow. Despite a higher fibre radius guarantees a higher recovery, Figure 4.21 shows also an increase in shell side pressure drops. This is due to the lower area density, higher volume and, therefore, a longer shell path length.

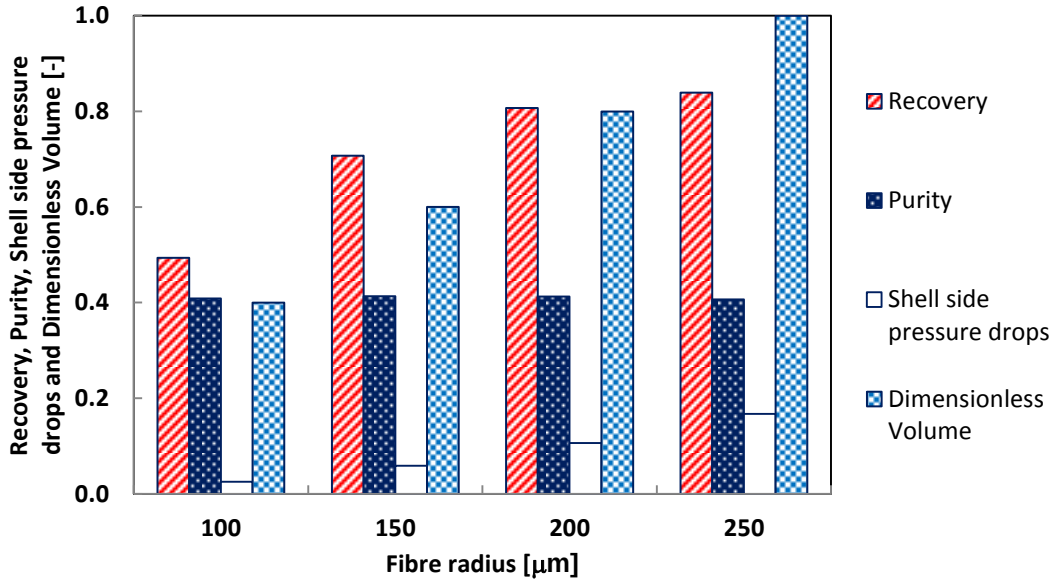

Figure 4.21: Sensitivity analysis with respect to fibre radius. CO_2 permeance = 5000 GPU, CO_2/N_2 selectivity = 50.

Simulations have also been run under different process conditions and material characteristics and – considering the 90° tube layout using Bell-Delaware correlation as the 2D base case – some common trends can be identified:

- Purity is not significantly affected comparing 1D and 2D simulations, while a difference in recovery is encountered. This is important to point out since hollow-fibre modules can be adopted for high-recovery stages where a higher membrane area is required and - due to the higher area/volume ratio than spiral-wound permeators - they can guarantee a more compact separation apparatus. Simulations assuming different fibre radius suggest that bore side pressure drops are not expected to affect purity, which seems to be more dependent on the membrane area, kept constant in the simulations in Figure 4.21.
- Bore side pressure drops are comparable in the 2D model and the one-dimensional analysis, while the shell-side contribution is dramatically increased. This is important in terms of energy consumption for recompression of the retentate stream. In the case of low pressure

applications such as carbon capture, a blower can be adopted at the feed side and its duty needs to be carefully evaluated. Therefore, a realistic indication of shell-side pressure drops is essential. Fibre layout should be also taken into account since it has been shown that it can be an important design parameter.

No experimental data are available for the validation of the results, which would be required to identify the level of accuracy of the implemented models. However, the reported simulations give important indications on the effect of a combined flow pattern which is realistic in hollow-fibre modules.

4.3 Spiral-wound simulations

The separation through spiral-wound modules is now under investigation. In order to carry out more detailed simulations, the geometry of the module needs to be considered. Due to the difficulty in finding detailed module dimensions in the literature, some assumptions are taken. An important parameter is the W/L ratio: a spiral-wound module with a diameter of 25 cm and a length 1 m is assumed. This can be considered a realistic assumption considering commercially available modules. Assuming that for spiral-wound modules an area density (membrane area/volume) of 1000 m^2/m^3 is a realistic value [26, 29] and considering a value of 1 m for L, a value of 25 m for W can be calculated considering a double selective layer around the feed compartment. The assumed channel thickness is 1 mm.

The criteria adopted for the simulations are similar to the ones chosen for hollow-fibre modelling in Figure 4.13. The parameter F/A (Inlet flow rate / module area) is used and different values are tested in order to analyse the behaviour of the separation. The one-dimensional cross-flow model is also included (reported as 1D cross-flow in the plots) in order to have a comparison among models with different levels of accuracy. The results are reported in Figure 4.22 terms of CO_2 purity and recovery. Process and membrane parameters are analogous to the assumptions taken in paragraph 3.2.2. It should be also pointed out that the inlet flow rates adopted in

this analysis correspond to conventional inlet conditions for spiral-wound membrane skids [26, 27, 140]. These also correspond to Reynolds numbers lower than 2000 for which the adopted pressure drop correlations are valid.

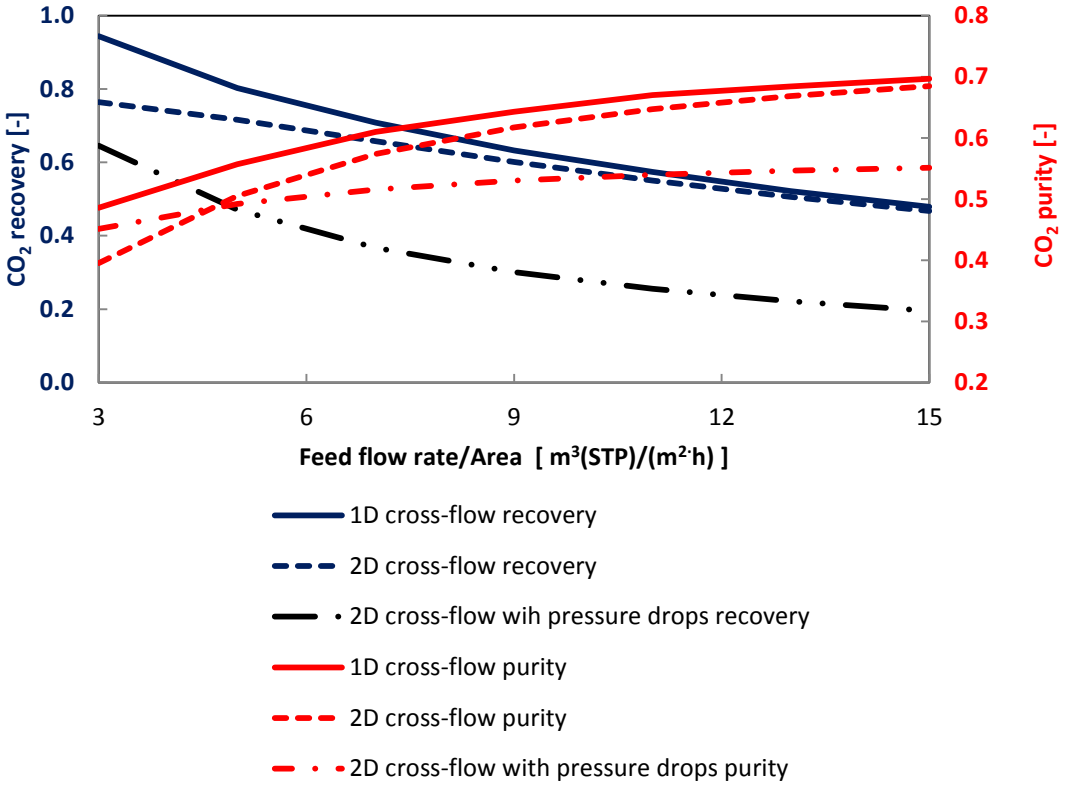

Figure 4.22: CO_2 purity and recovery vs. Feed flow rate/area - carbon capture simulations. CO_2 permeance = 5000 GPU, CO_2/N_2 selectivity = 50.

It is important to identify the similar prediction between 1D and 2D model with no pressure drops in the range of high F/A: these values correspond to uniform profiles on both sides, which can be approximated by a 1D trend. When specific area and module recovery are higher, both directions become significant and the predictions between the two approaches become different. This can also be linked to the 1D partial pressure profile reported in Figure 4.3: for low recovery the trend is linear for both sides, no significant difference is encountered between feed and retentate conditions and this leads to a similar approximation between 1D and 2D cases.

First of all, the simulations confirm that relevant pressure drops are expected only for the permeate side, due to the longer width path compared to module length. Therefore, since retentate pressure drops are not as significant as for hollow-fibre modules, it is expected that high F/A can be adopted for spiral-wound modules and this corresponds to high-purity stages. However, a significant difference in prediction for both recovery and purity is encountered in Figure 4.22 when pressure drops are considered. In particular, it is possible to point out an asymptotic trend in purity for high F/A compared to the base simulations with no pressure drops: this confirms the discussion on hollow-fibre results in Figure 4.13 where a pressure ratio limited regime was encountered. The asymptotic purity is related to the lower pressure ratio due to pressure drops, in this case only at the permeate side. This example underlines that the choice of the operating conditions is expected to significantly affect the performances, particularly in terms of maximum achievable permeate concentration.

Apart from giving an idea of the optimal operating conditions for a given module geometry, this analysis can give also guidelines in terms of module design. In the perspective of having highly permeable materials, channel spacer and its thickness should be carefully considered. As for hollow-fibre permeators, module characteristics should be designed with respect to both materials and applications.

The reported simulations are run assuming non-ideal behaviour: however, no relevant changes are encountered considering ideal gas law. Simulations in non-isothermal case have also been run and, as expected, no significant temperature differences are encountered due to the low operative pressure for carbon capture applications.

This analysis confirms that operating conditions should be carefully chosen and that pressure drops play a key contribution on module performances. A pressure profile for permeate side is presented in Figure 4.23, where it can be observed that pressure drops are more significant at the beginning of the leaf ($l = 0$) and at feed side inlet, where the flux through the membrane is higher. Permeate pressure drops of approximately 20 kPa have been encountered in this analysis, which are in line with

recent data from MTR Inc. from their pilot plant tests for post-combustion carbon capture using spiral-wound modules [54].

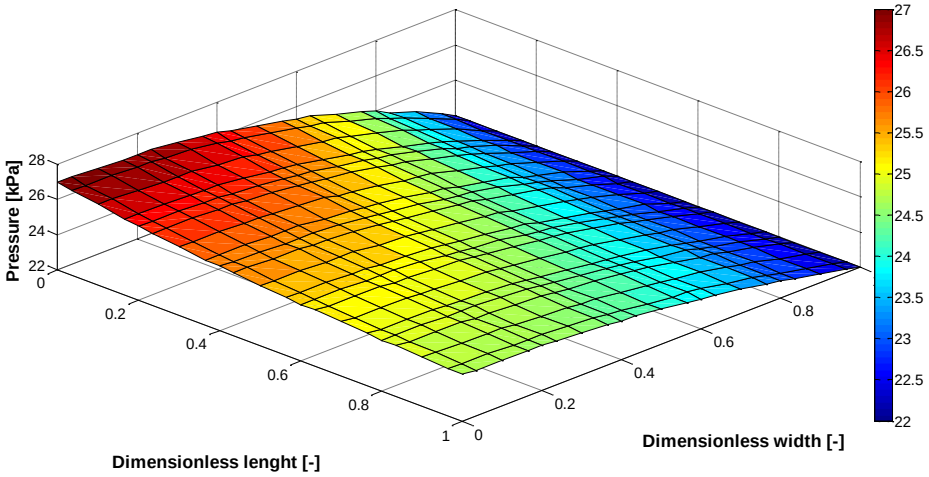

Figure 4.23: Example of permeate pressure profile with pressure drops for the 2D cross-flow model.

In analogy with the hollow-fibre analysis, the attention is also focused on natural gas separation to test the non-isothermal formulation. The simulations are run under the process conditions reported by Coker et al. [105] for their hollow-fibre analysis. The feed stream is a bi-component mixture containing 10 % CO_2 and 90 % CH_4 at a pressure of 5.8 MPa; the permeate pressure is 0.2 MPa. In Figure 4.24 the results in terms of difference between retentate and feed temperature are reported with respect to F/A. A similar trend to the counter-current flow pattern is identified [141], with the expected cooling down of the retentate stream when recoveries are higher. However, Figure 4.24 also presents the results in terms of difference between permeate and feed temperature, which in hollow-fibre simulations is negligible. Due to the different flow pattern compared to counter-current case, a cooling down of the permeate stream is also encountered. In counter-current case retentate and permeate streams exchange heat along all the available area, while for cross-flow in a spiral-wound module the separated species at the permeate side for each l coordinate are in contact with the retentate side along the width direction, before ending in the central compartment. The temperature profiles have also been analysed: differently from the

partial pressure profiles, the trend is only dependent on the flow coordinate, l for feed and w for permeate sides.

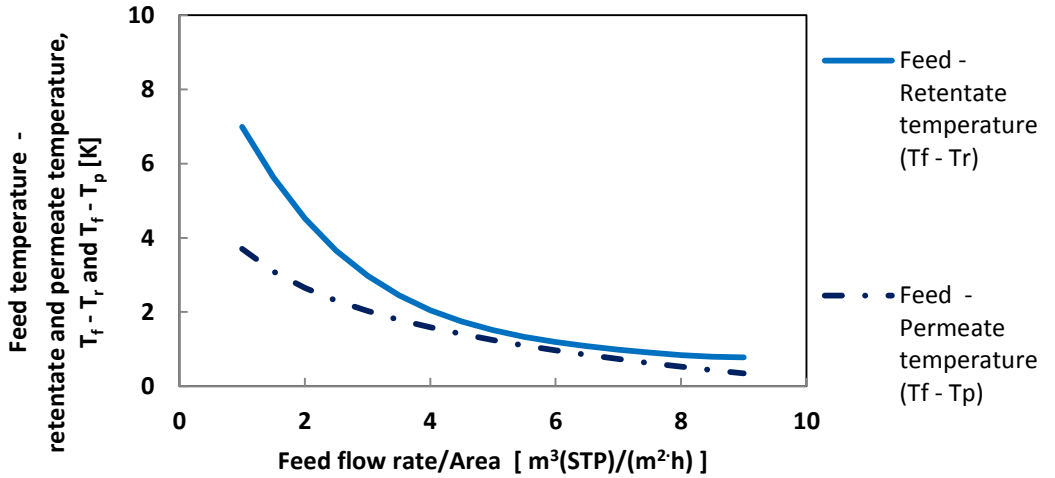

Figure 4.24: Non-isothermal simulations for natural-gas separation. CO_2 permeance = 23 GPU, CO_2/CH_4 selectivity = 32.

Consequently, in spiral-wound modules with high-pressure separations where Joule-Thomson coefficients of the treated species are high, more significant temperature changes in the permeate side might be expected compared to hollow-fibre counter-current case.

4.4 Statistical analysis for hollow-fibre and spiral-wound modules

The possible effects of module defects on the performances are discussed in this section. Initially, the statistical approach previously presented is applied to the 2D hollow-fibre case. It is assumed that the fibre population is non-uniform. The average and standard deviation of a desired property are set as inputs. Multiple simulations are run (250 runs per point) and the data are analysed with a Matlab® script which calculates maximum, minimum and average for a 95 % level of confidence. The

error bars in the plots included in this paragraph indicate the standard deviation of the simulations.

No variation of the porous support thickness is assumed, but only of the external diameter. Consequently, the velocity inside and outside the fibres is dependent on the position. The total number of fibres is assumed constant as well as the total membrane area: therefore, area density σ and fibre fraction Δ are dependent on the fibre radius for each coordinate. The same feed flow rate as the previous 2D simulations (10 mol/s) is assumed, three compartments are considered and simulations are run in ideal and isothermal mode. Shell-side pressure drops are expressed according to the Bell-Delaware method. The results in terms of CO_2 recovery and purity are reported, respectively, in Figure 4.25 and Figure 4.26. It can be observed from Figure 4.25 that the product recovery is affected for standard deviations higher than 10 % and a difference in recovery of approximately 7 % can be achieved for higher standard deviations. On the other hand, no significant effects on purity are encountered as evident from Figure 4.26.

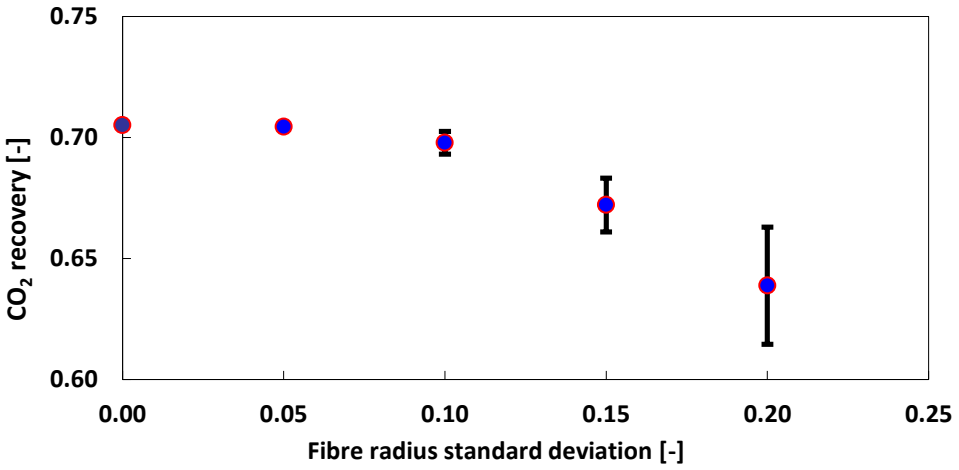

Figure 4.25: Effect of fibre radius standard deviation on CO_2 recovery. CO_2 permeance = 5000 GPU, CO_2/N_2 selectivity = 50.

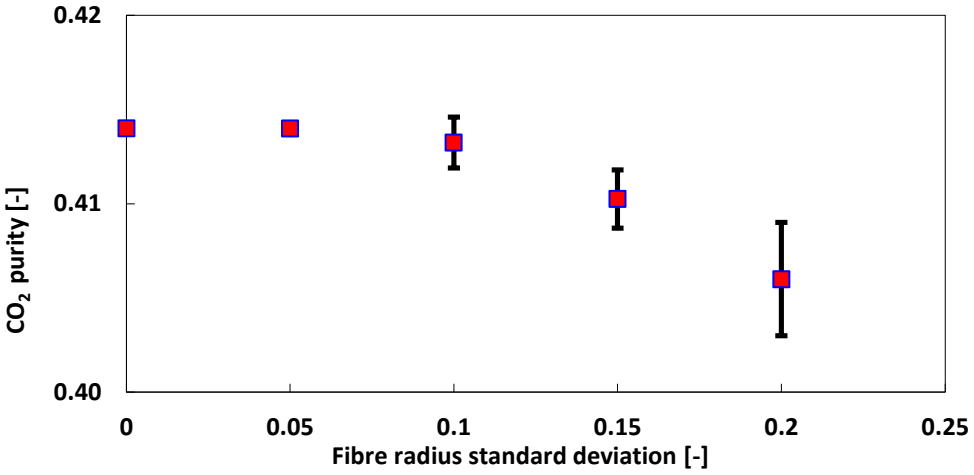

Figure 4.26: Effect of fibre radius standard deviation on CO_2 purity. CO_2 permeance = 5000 GPU, CO_2/N_2 selectivity = 50.

This observation underlines the importance of a uniform population of fibres and it shows the possible effects of module defects on its performances. The behaviour in Figure 4.26 can also be linked to the parametric study carried out and presented in Figure 4.21, where no relevant effect on purity was shown with respect to fibre radius. On the other hand, simulations results show a significant effect on recovery and this is an important point of discussion. A variable cross-sectional area for both sides, due to the non-uniform radius distribution, leads to a variable velocity inside and outside the fibres with respect to their position in the module. This directly affects pressure drops and, therefore, the driving force for the separation. Simulations have been carried out with different feed flows and it has been confirmed that the effect on product recovery is more significant in the area of F/A lower than 5, where the separation efficiency of the module is higher and the bore side gives the most significant contribution in terms of pressure drops. This can also be linked to the permeate pressure drops trend reported in for the 1D model. This trend is expected to be similar since the fibre direction is the same for both 1D and 2D compartmental models. In Figure 4.14 it is shown that bore side pressure drops increase with increasing F/A (in the lower range, up to F/A = 7 m^3(STP)/(m^2·h)) which is related to a higher permeate velocity due to increasing permeate flows. If a non-uniform population of fibres is present, the contribution of the fibres with lower fibre radius

than the average value - where the velocity will be higher and therefore pressure drops will be higher - are expected to significantly affect the performances. Despite not being as significant as the bore side effect in the simulated case, a higher fibre radius than the average value reduces the cross-sectional area for the shell side and this directly affects retentate pressure drops. Consequently, the flow distribution in both sides of the module is affected by increasing fibre radius standard deviation. It is also suggested that the effects of module defects can be related to the operating conditions of the separation. Carefully and accurately designed modules are therefore of particular importance.

This simple approach can be used to analyse data from tests on membrane permeators, where a lower recovery than the value predicted by simulations might also be due to flow mal-distributions inside the module.

The statistical approach is applied to spiral-wound modules and simulations using the 2D cross-flow model are presented. Particular focus has been dedicated to permeate channel thickness, a key parameter in terms of pressure drops. A non-uniform thickness is assumed and the effect on the performances is investigated, similarly to the approach followed for hollow-fibre simulations. Channel thickness average and standard deviation are set as input and the results are analysed. The simulations are run for a low-recovery/high purity, corresponding to F / A = 15 in the previous plots. This application is also related to the negligible retentate pressure drops encountered in the spiral-wound simulations previously carried out which allow the deployment of this module configuration for higher inlet velocities and, therefore, high-purity stages.

The results are reported in Figure 4.27 and Figure 4.28 in terms of CO_2 purity and recovery, respectively. It can be observed that, despite not significantly affecting the recovery, a change in CO_2 purity might be encountered. For permeate channel thickness standard deviations lower than 10 %, the performances are not generally affected while a difference in CO_2 purity of approximately 4 % might be achieved for standard deviations of 20 %.

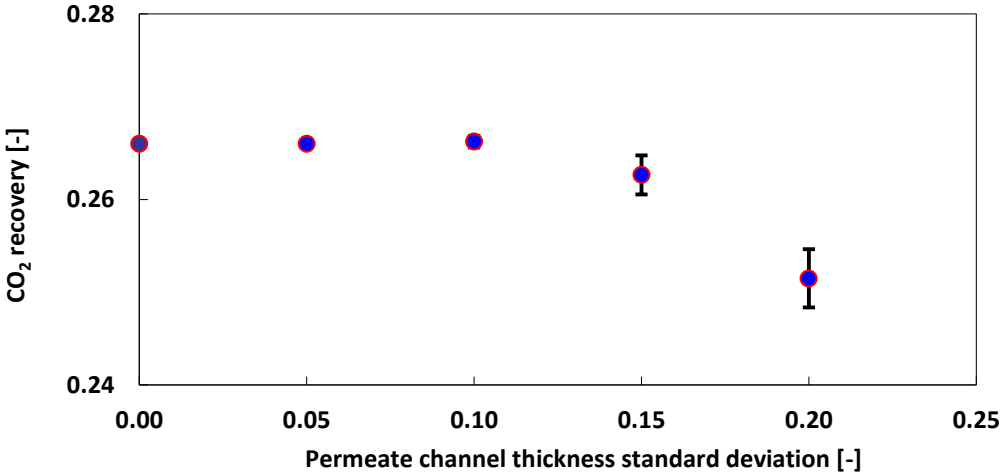

Figure 4.27: Effect of permeate channel thickness standard deviation on CO_2 recovery. CO_2 permeance = 5000 GPU, CO_2/N_2 selectivity = 50.

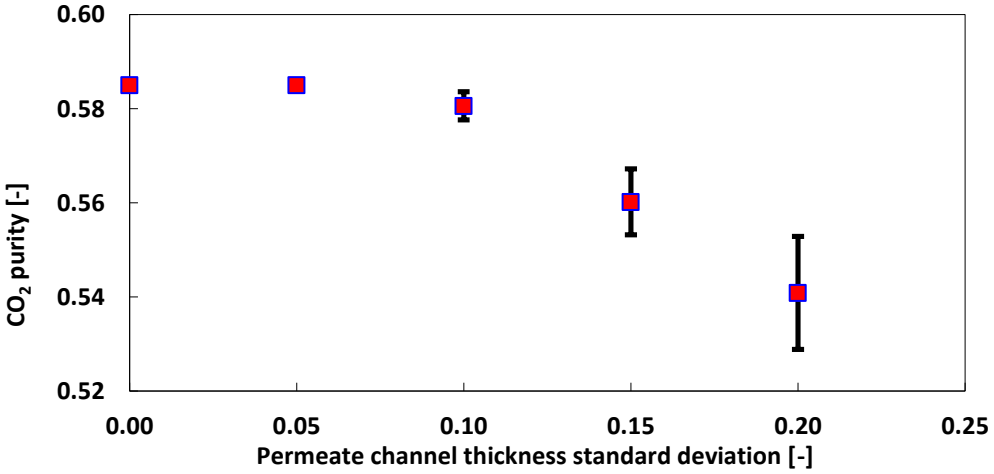

Figure 4.28: Effect of permeate channel thickness standard deviation on CO_2 purity. CO_2 permeance = 5000 GPU, CO_2/N_2 selectivity = 50.

In spiral-wound simulations, permeate side pressure drops were the main contributors to the drop in performances and it can be suggested that a pressure ratio limited regime could be encountered for high flow applications. A non-uniform channel thickness is expected to affect pressure drops, particularly in the first section of the module (see Figure 4.23) and this might lead to the difference in purity which is encountered. The effect on purity compared to the hollow-fibre case can be also

due to the different module configuration. While for a hollow-fibre module all the permeate stream is flowing along the z direction **(**Figure 3.8**)**, in a spiral-wound unit the permeate exchanges gas only along the width direction before mixing in the central compartment **(**Figure 3.10**)**. This analysis is particularly important as the investigation of the optimal channel thickness can lead to practical conclusions able to guarantee that the separation requirements are met even in presence of fabrication defects.

Both spiral-wound and hollow-fibre simulations have also been run assuming a standard deviation of CO_2 permeance, which can account for variable thickness of the membrane selective layer. However, no significant difference in prediction is encountered confirming the investigation carried out by Lemanski and Lipscomb [135].

In conclusion, the results obtained by the simulations shown in this section underline the importance of module defects for an effective evaluation of module performances.

4.5 Dynamic simulations

Membrane separation is a modular and flexible operation and, thanks to the developed models presented in Chapter 2, preliminary simulations can be run to investigate its behaviour under dynamic conditions.

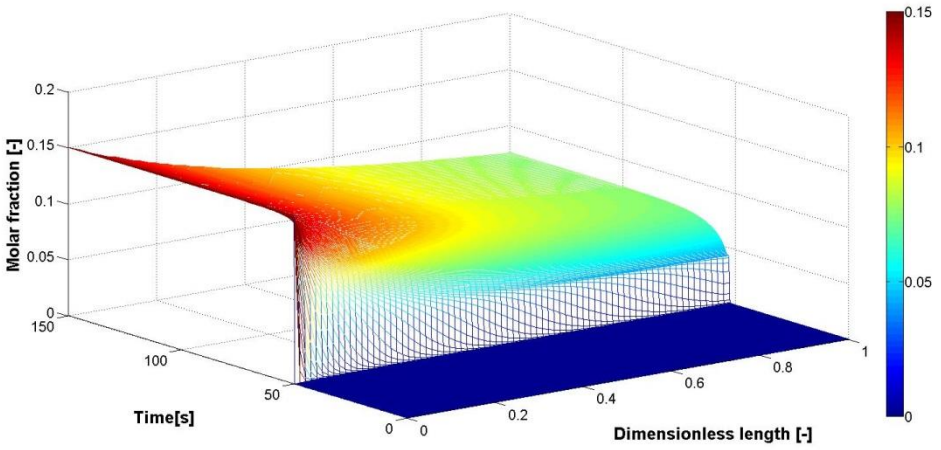

Figure 4.29: Example of CO_2 molar fraction profile - dynamic 1D hollow-fibre model. CO_2 permeance = 5000 GPU, CO_2/N_2 selectivity = 50.

In Figure 4.29 a CO_2 molar fraction profile with respect to time and module length is reported using the 1D hollow-fibre model (dead-end counter-current, no pressure drops and ideal behaviour). Module parameters are the same reported in Table 4.1 and the simulation is run for a high-recovery stage (10 mol/s as feed, 15 % CO_2/ 85 % N_2 mol/mol). A step change in inlet conditions is assumed at t = 50 s: the code also includes the possibility of implementing valve equations which can be realistic in the case of dynamic conditions.

In Figure 4.30 the trends in stage cut, CO_2 purity and recovery for a 2D cross-flow simulation are presented (no pressure drop, ideal behaviour, step change in inlet conditions at t = 10 s, 10 mol/s as feed, 15 % CO_2/ 85 % N_2 mol/mol and high-purity application).

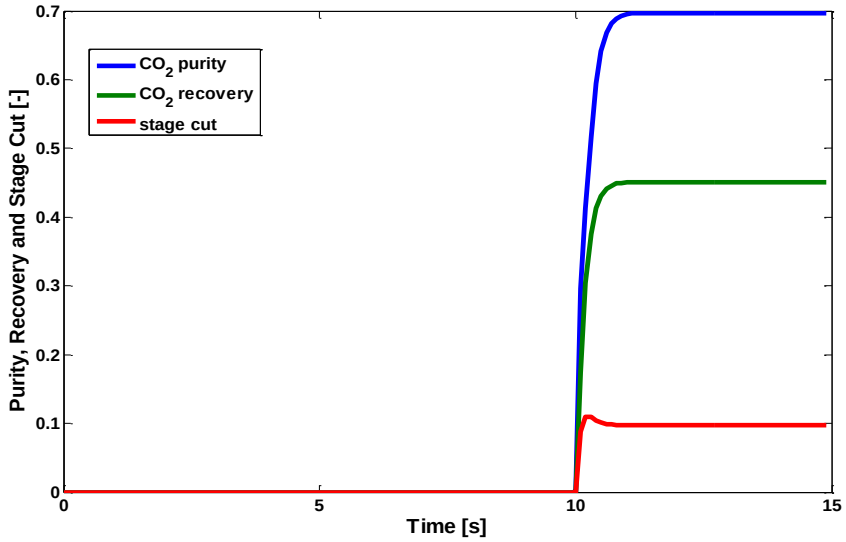

Figure 4.30: Example CO_2 purity, recovery and stage cut profile – 2D cross-flow dynamic model. CO_2 permeance = 5000 GPU, CO_2/N_2 selectivity = 50.

For both Figure 4.29 and Figure 4.30 it is possible to identify an approximately immediate response to a change in process conditions. In the case of counter-current, the transient is lower than 10 s while for the cross-flow case it reduces to less than 5 s.

Even though a detailed dynamic analysis is not a target of this thesis, these examples show the potential of a fast response for the membrane units, essential for future flexible applications. Therefore, in the perspective of running dynamic simulations of the whole process, it is not expected to have a significant contribution from the membrane separation system.

In conclusion, the preliminary dynamic simulations shown in this section confirm that a detailed steady-state analysis can already give important indications in terms of feasibility for membrane separation applied to carbon capture applications. Steady-state process simulations will be carried out in Chapter 5 and they will also be linked to the economic analysis reported in Chapter 6.

Chapter 5: Multi-stage designs

The aim of this Chapter is to present the multi-stage analysis carried out on the basis of the single-stage simulations reported in Chapter 4.

The attention is initially focused on simulation assumptions before presenting the different flowsheets. Material and process parameters are under investigation and the performances are expressed in terms of membrane area and energy consumption.

The stream properties for the membrane designs reported throughout this Chapter are reported in Appendix C.

5.1 Base case power plant

A schematic representation of the base case power plant assumed in this work is reported in Figure 5.1. It is a 550 MW coal-fired power plant with a sub-critical steam cycle (16.7 MPa/838.8 K/838.8 K) simulated by Ahn et al. [20] and based on the assumptions reported in the 2007 DOE report, Case 9 [24].

The flue gas, after the flue gas desulphurisation (FGD) unit, is at 330 K and 117 kPa and saturated with water. The characteristics of the flue gas exiting the FGD are reported in Table 5.1.

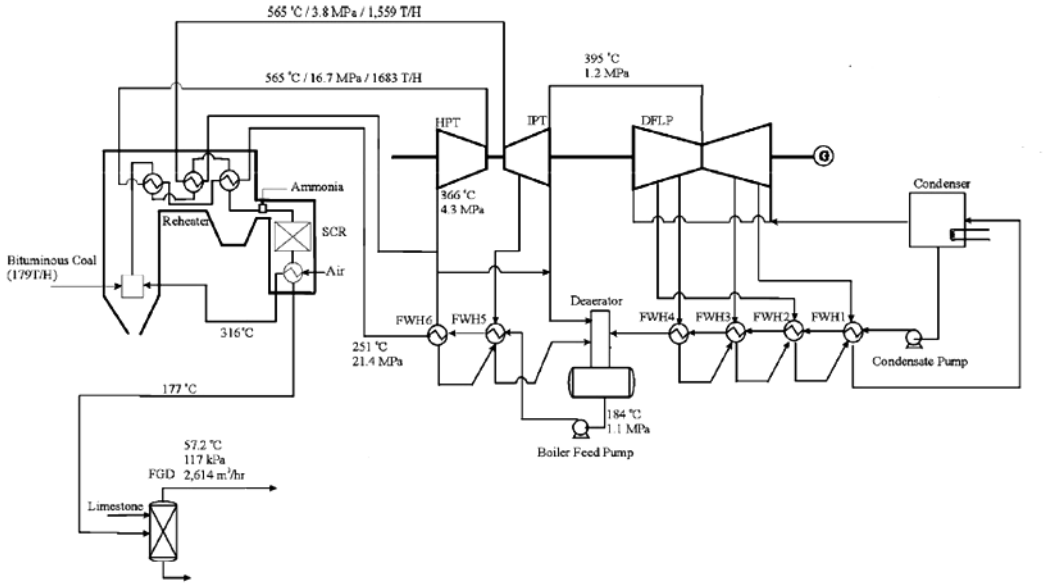

Figure 5.1: Base case 550 MW subcritical coal-fired power plant simulated by Ahn et al. [20].

Molar Flow rate	$2.02 \cdot 10^4$ mol/s
Molar fractions	0.15 CO_2, 0.74 N_2, 0.02 O_2, 0.09 H_2O
T and P	330 K and 117 kPa

Table 5.1: flue gas conditions [20] for the design in Figure 5.1.

This flowsheet has been simulated in Honeywell UniSim® Design (version R400) by Ahn et al. [20] and has been the starting point for the developed multi-stage designs.

5.2 UniSim® Design and its customisation

UniSim® Design is the software adopted for the process simulations which are presented in this thesis. However, the commercial software does not include a membrane unit operation into the simulation environment. Therefore, a key aspect of the work presented in this thesis has been the customisation of UniSim® with a new unit operation, Membrane_UoE.

The implemented models have been kept in the original formulation and a C++ interface has been developed to allow the communication between the simulation environment and the in-house software. The general approach to the calculation consists in taking the inlet stream conditions from UniSim®, calculating the outlet status and then putting it into the outlet streams properties.

The simulations in this Chapter are based on non-dispersed plug-flow (Membrane_UoE 1.0, counter-current flow pattern with sweep) and 2D cross-flow models (Membrane_UoE 2.0). The UniSim® icons have also been customized as shown in Figure 5.2. These unit operations use the membrane area as a design parameter; no pressure drops and ideal behavior are assumed. The membrane parameters (membrane area, key component permeance and its selectivity over the other components) are set by the user in the interface, which is similar to the other unit operations available in the simulation environment. A detailed description of this integration is reported in Appendix B.

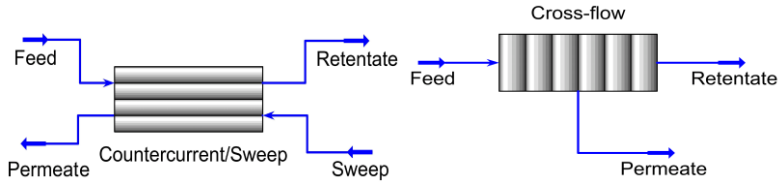

Figure 5.2: Membrane_UoE 1.0 (left) and 2.0 (right).

Thanks to the developed interface, process simulations have been carried out including the customised membrane unit operations. An example of UniSim® flowsheet is reported in Figure 5.3. For the proposed multi-stage designs in the following paragraphs, schematic drawings using Microsoft Visio will be adopted.

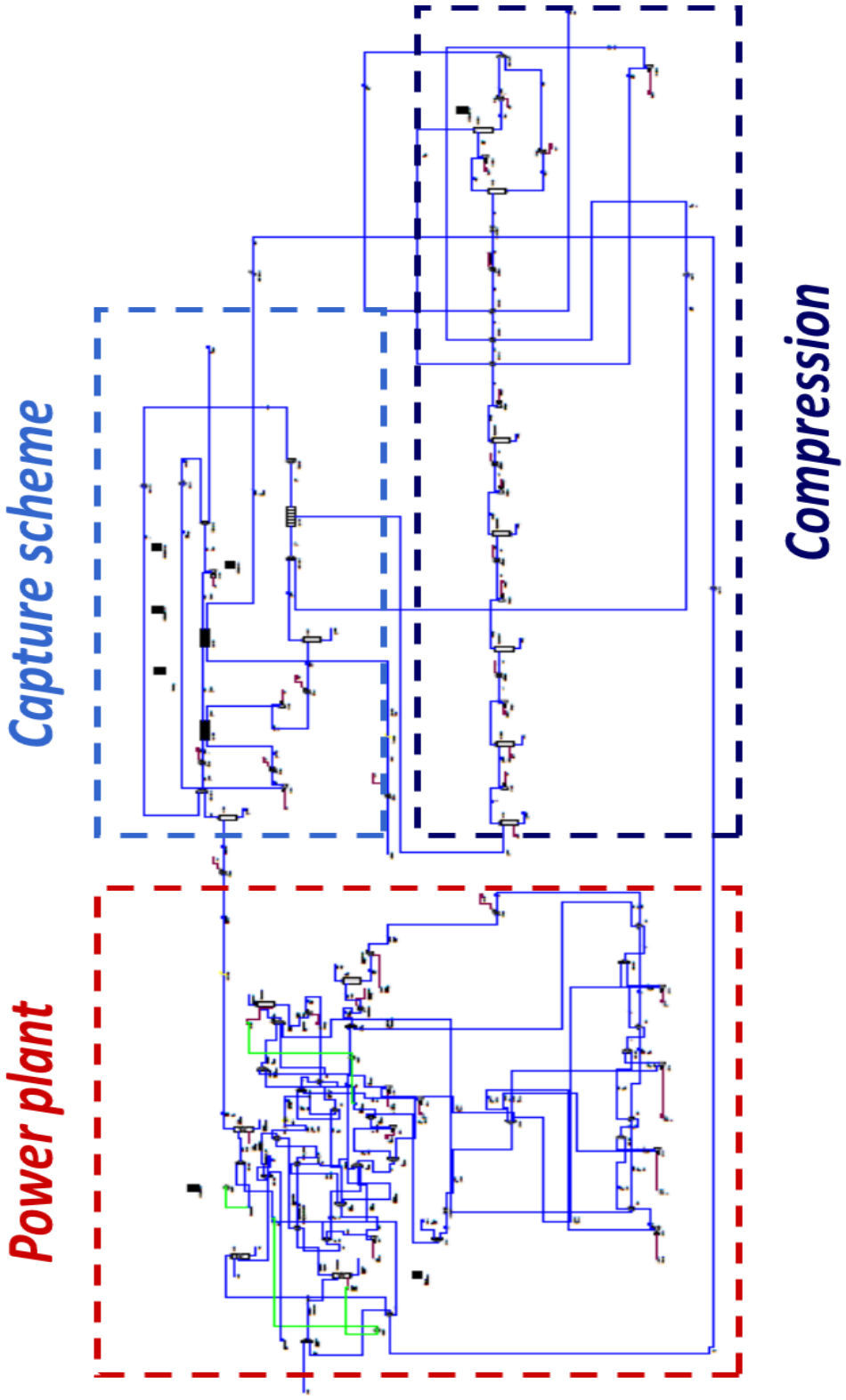

Figure 5.3: Example of UniSim® flowsheet including the power plant.

5.3 Multi-stage approach

On the basis of the simulations carried out and presented in Chapter 3, high-recovery counter-current stages with sweep are simulated using the non-dispersed plug-flow model and the 2D cross-flow model is adopted for high-purity stages. No pressure drops are initially assumed.

The process assumptions for the simulations presented in this thesis are:

- 117 kPa at the feed side and vacuum of 22 kPa (220 mbar) [39] at the permeate side;
- Compressor/pumps/expander efficiency of 80 %;
- Inlet temperature of 298 K;
- Final multi-stage compression train based on the DOE guidelines [24] with intercooling at 318 K.

The reported analysis is based on data from polymers. For the purpose of the presented simulations, a material with a CO_2 permeance of 12000 GPU is assumed. This might correspond to a membrane with a permeability of 12000 Barrer (a value which can be achieved by PIM 1 [142]) and a thickness of 1 μm. CO_2 selectivities over Nitrogen, Oxygen and water are assumed, respectively, 50, 15 and 1. This choice is related to the assumption of a hypothetical material with optimal properties in terms of CO_2 permeance and selectivity over the other components. These properties are in line with the research targets for Polaris™ advanced membrane as shown in Figure 5.4 (CO_2/N_2 selectivity of 50 and a CO_2 permeance ~10^4 GPU).

It also needs to be underlined that in this work optimal material characteristics are assumed and then studied in the parametric analyses which will be presented in both Chapter 5 and Chapter 6. For example, the effect of CO_2 permeance and its selectivity with respect to Oxygen and Nitrogen will be investigated in the parametric analysis.

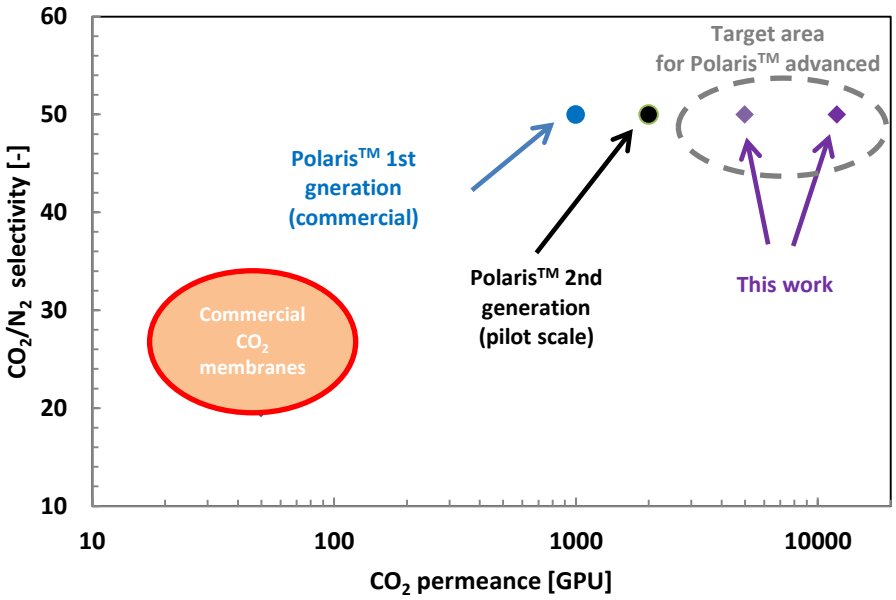

Figure 5.4: CO_2 permeance and CO_2/N_2 selectivity assumed in this work (CO_2 permeance of 5000 GPU in Chapter 4 and CO_2 permeance of 12000 GPU Chapter 5) in comparison with Polaris™ membrane properties.

5.4 Results

In this section the results are presented according to the classification adopted in Chapter 1: retrofit, hybrid and selective exhaust gas recycling designs.

5.4.1 Retrofit configuration

The dual-stage retrofit configuration proposed in this thesis is reported in Figure 5.5: a counter-current stage with retentate as sweep is followed by a cross-flow high-purity stage. The resulting stream from stage 2 contains approximately 90 % CO_2 and it is sent to the compression train. At this stage of the analysis, no drying unit at the end of the compression system is included into the design; the results in terms of

energy consumption and membrane area are shown in Figure 5.6. Energy consumptions of 300 - 400 kWh_e/t_{CO_2} are identified with a membrane area in the range of 3.0 - 3.6x10^5 m^2 depending on the final purity. The results are reported for different final purities in order to evaluate its effect on the overall performances: an exponential trend is identified for purities higher than 95 %.

The results from this initial design represent the baseline for modifications in the process flowsheets presented in the next paragraphs.

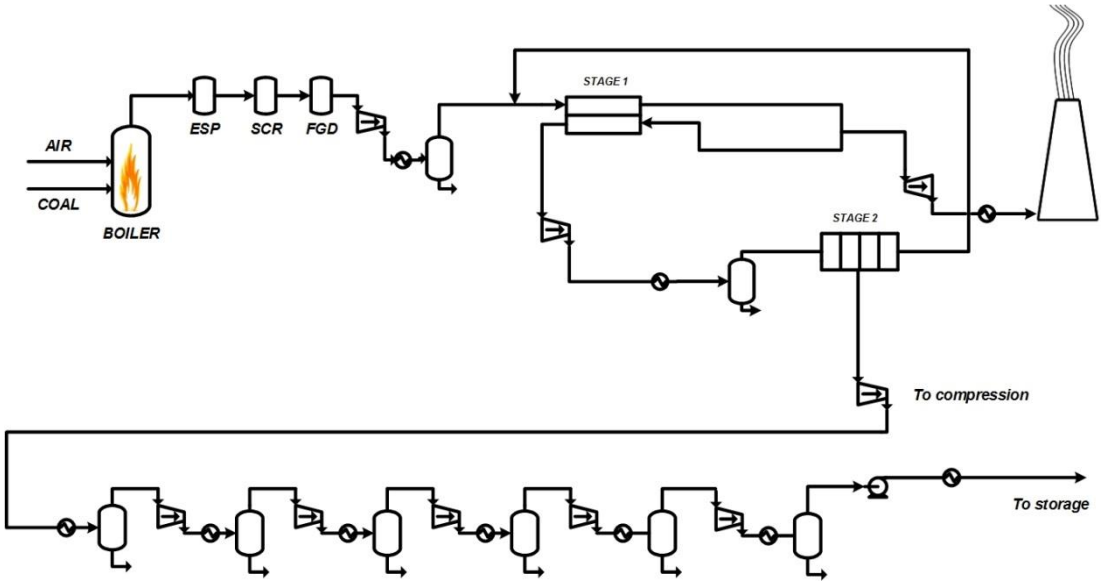

Figure 5.5: Proposed Retrofit configuration. Stream properties reported in Appendix C.

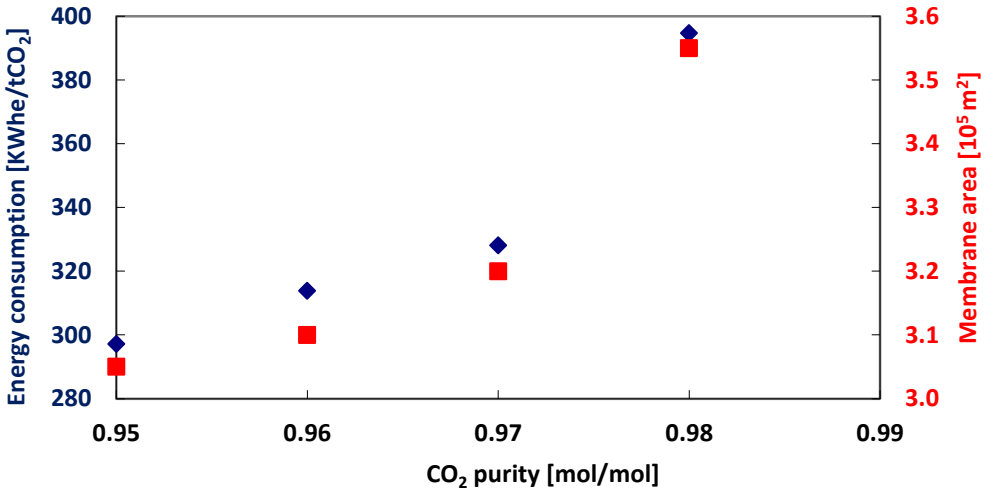

Figure 5.6: Dependence of membrane area and energy consumption on final CO_2 purity for the proposed Retrofit design. CO_2 permeance = 12000 GPU, CO_2/N_2 selectivity = 50, CO_2/O_2 selectivity = 15 and CO_2/H_2O selectivity = 1.

5.4.2 Hybrid configuration

The hybrid configuration proposed in this work, under the same assumptions as the retrofit option, is shown in Figure 5.7. The CO_2-rich stream is compressed and intercooled to 318 K in three stages from atmospheric to 3.0 MPa bar. In contrast to the original design, the last compression stage is removed and the stream is cooled to 253 K. A Joule-Thomson valve is included and, as a result of the expansion, the temperature is reduced to 238 K. Two separators in series are then included and the resulting gas stream is sent as recycle to inlet of Stage 2 to increase its entering CO_2 composition. By using this option, liquid CO_2 is produced after the refrigeration stage and then a pump is placed in order to reach a pressure of 15.0 MPa required for storage. An efficiency of 50% for the refrigeration cycle is assumed in order to estimate the overall energy consumption. By fixing CO_2 purity at 98 %, an energy consumption of 321 kW_e/t_{CO_2} and a membrane area of $3.0x10^5$ m^2 are achieved. A

comparison with the results in Figure 5.6 shows the benefit of this process configuration in terms of energy consumption, for the same final CO_2 purity. This design is chosen for the economic evaluation due to its improved overall performances and it will be elaborated in Chapter 6.

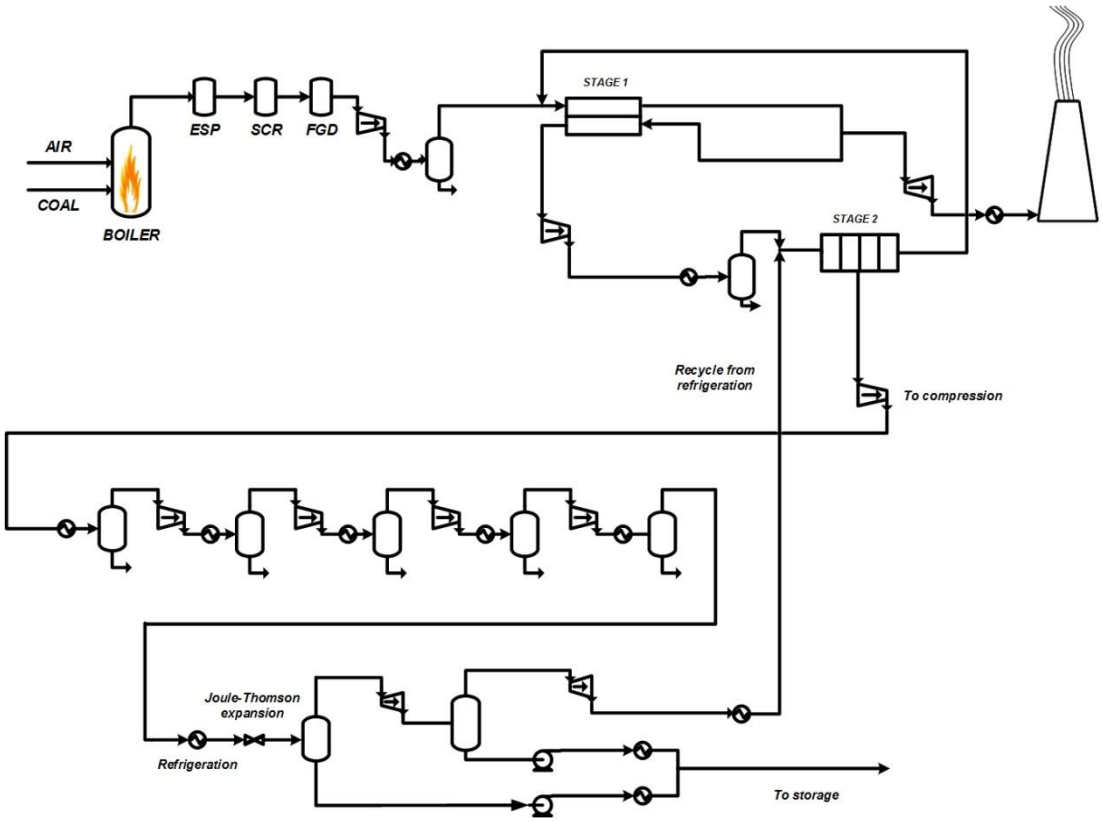

Figure 5.7: Proposed Hybrid design. Stream properties reported in Appendix C.

5.4.3 Selective exhaust gas recycling configuration

Figure 5.8 shows the selective exhaust gas recycling configuration proposed in this thesis. The flue gas is sent to a first counter-current stage: its permeate is sent to a cross-flow stage in order to achieve higher CO_2 purities while the retentate is sent to a high-recovery counter-current stage with air as sweep at atmospheric pressure. The permeate stream from the 2nd stage contains 3 % of CO_2 and 19% of Oxygen, which is directly sent to the boiler. CO_2 is recovered in both stage 1 and 2 due to the

additional counter-current-sweep stage. Consequently, the permeate stream from stage 1 has a lower flow rate and higher CO_2 concentration. This justifies the lower energy consumption compared to retrofit and hybrid options. However, by keeping the same air flow rate as the base plant and sending it completely to stage 2 as sweep, 7% of the total Oxygen is lost via back-permeation in the retentate side of stage 3.

CO_2/O_2 selectivity is a key parameter: this is demonstrated looking at the lower CO_2 content in the stream to the boiler compared to the design by Merkel et al. [39], due to the lower CO_2/O_2 selectivity assumed in this work. Fixing the CO_2 content to 8 % with the assumed membrane CO_2/O_2 selectivity in this thesis would mean Oxygen content lower than 17 % to the boiler and, consequently, conditions in the combustor would be dramatically affected. The benefit of this design is significant in terms of membrane area (-24 %) but also of reduction in energy consumption (-7%). In Table 5.2 a comparison with the hybrid option is presented terms of energy requirement and membrane area.

	En. Consumption **[kWh_e/t_{CO_2}]**	**Area** **[10^5 m^2]**	**Purity** **[mol/mol]**
Hybrid	321	3.0	0.98
Selective Exhaust Gas Recycling	296	2.3	0.98

Table 5.2: Results for Hybrid and Selective Exhaust Gas Recycling options.

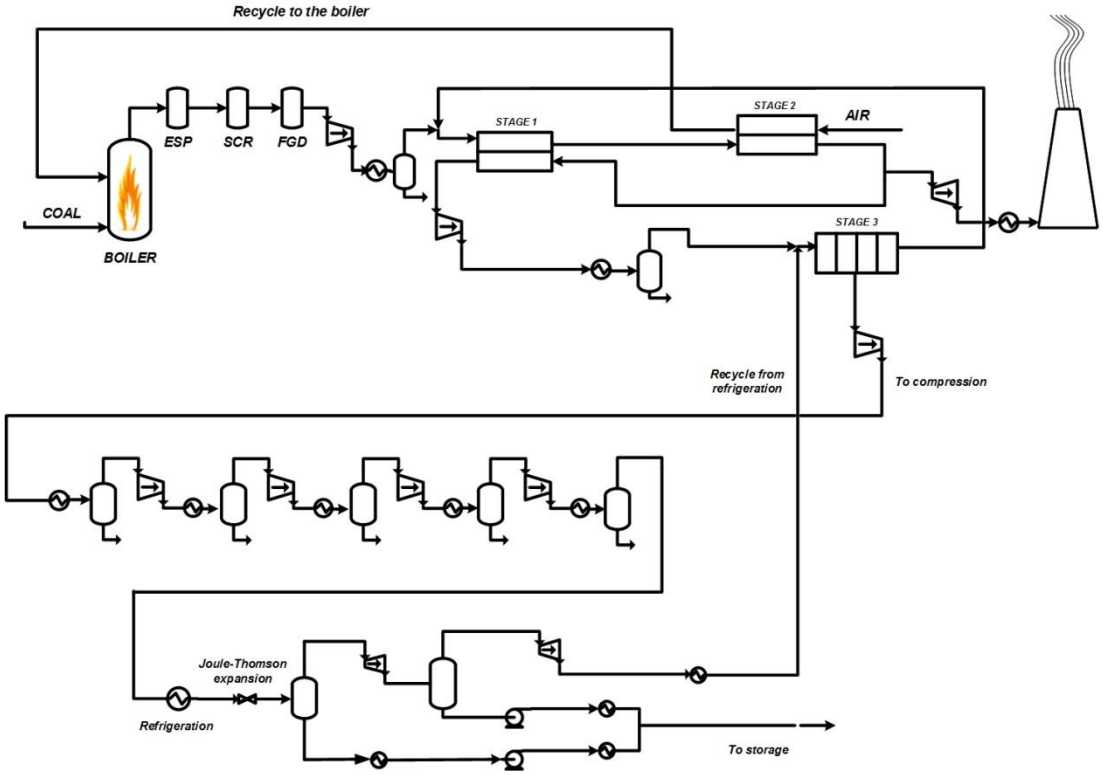

Figure 5.8: Selective Exhaust Gas Recycling design. Stream properties reported in Appendix C.

The main benefit of this option compared to the hybrid design is a reduction in the consumption (-10 %) for the vacuum pumps after both Stage 1 and 3: this is due to the lower recovery that can be set in Stage 1. The additional counter-current stage (Stage 2 in Figure 5.8) can compensate for the lower recovery of the first stage, achieving the targeted final recovery. On the other hand, the difference in blower consumption does not give a significant contribution to the overall difference in energy requirement. The reduction in membrane area is achieved due to the increased CO_2 content in the flue gas and to the additional driving force provided by the counter-current stage with air as sweep.

In Table 5.3 the total energy consumption for vacuum pumps, the area for the counter-current stages (Stage 1 for hybrid and Stage 1 + Stage 2 for selective exhaust gas recycling option) and the CO_2 content of the flue gas are reported as representative comparison between hybrid and selective exhaust gas recycling designs.

	Vacuum Pumps Energy Requirement [MW]	Area counter-current stages [10^5 m^2]	CO_2 flue gas [mol/mol]
Hybrid	77	2.8	0.148
Selective Exhaust Gas Recycling	69	2.0	0.171

Table 5.3: Comparison between hybrid and selective exhaust gas recycling option in terms of total vacuum pump energy requirement, area for stage 1 and CO_2 inlet in stage 1.

The distribution of the specific energy consumptions from the different contributions is reported in Figure 5.9, where it is evident that, in the selective exhaust gas recycling design, the specific energy requirement for the membranes is reduced.

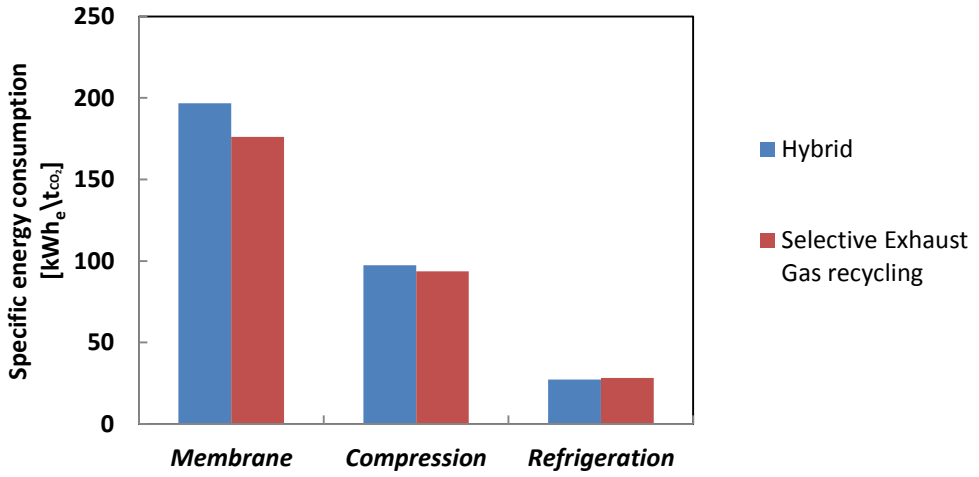

Figure 5.9: Distribution of specific energy consumption for Hybrid and Selective Exhaust Gas Recycling cases. CO_2 permeance = 12000 GPU, CO_2/N_2 selectivity = 50, CO_2/O_2 selectivity = 15 and CO_2/H_2O selectivity = 1.

A lower area required for the separation unit would also mean a more compact separation apparatus. In Table 5.4 a volume estimation for the membrane modules for the hybrid and the selective exhaust gas recycling design is reported, based on packing density data available in the literature [26, 29, 86]. Counter-current stages are considered as hollow-fibre and cross-flow as spiral-wound modules.

Packing density range		**Estimated volume range**	
Spiral-wound [m^2/m^3]	Hollow fibre [m^2/m^3]	**Hybrid [m^3]**	**Selective Exhaust Gas Recycling [m^3]**
1000 - 1600	4600 - 10000	**40 - 80**	**27 - 54**

Table 5.4: Volume estimation for Selective Exhaust Gas Recycling and Hybrid options. CO_2 permeance = 12000 GPU, CO_2/N_2 selectivity = 50, CO_2/O_2 selectivity = 15 and CO_2/H_2O selectivity = 1.

5.5 Parametric analysis

5.5.1 CO_2/N_2 selectivity

Among membrane properties, CO_2 permeance is directly related to membrane area and, consequently, capital cost. This aspect will be carefully discussed in the next Chapter where the economic performances will be also considered.

Selectivities of CO_2, over the other components present in the flue gas, directly affect not only their content in the final stream but also the energy consumption. A more selective membrane implies less impurities in the permeate stream, lower power requirement for vacuum pumps and the compression system, and therefore lower capital costs. To show this, simulations using the hybrid design have been run assuming a CO_2/N_2 selectivity of 25, which is the value reported for PIM 1 by Budd et al. [142]. A CO_2/N_2 selectivity of 25 is in line with commercial natural gas separations polymers [28, 47, 143]. Other process and material parameters are kept constant. These data are compared to the base-case selectivity of 50 in Figure 5.10, where membrane area and power consumption are dimensionless with respect to the base simulation. As expected, membrane area and final CO_2 purity are not significantly affected, while a significant change in energy consumption is

encountered. This is due to the additional energy for vacuum pumps but also for the final compression/refrigeration train, since more impurities are present.

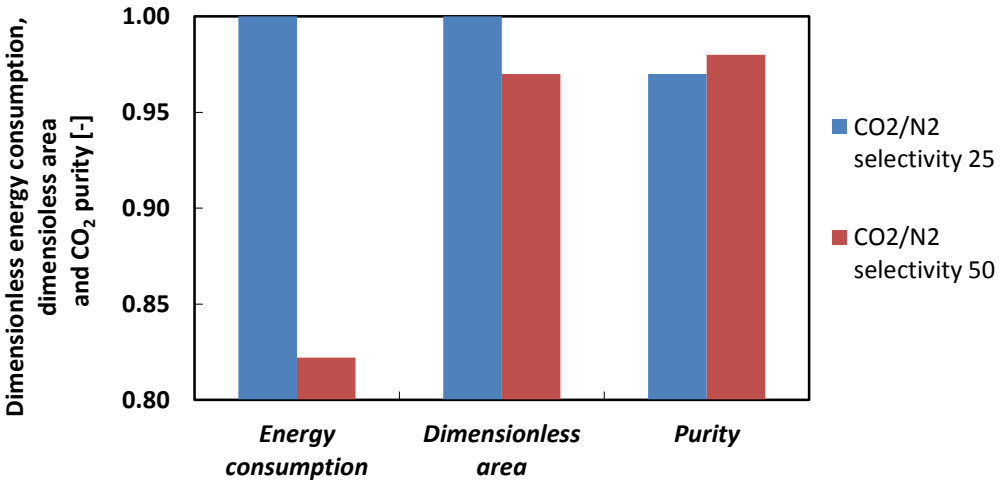

Figure 5.10: Effect of different CO_2/N_2 selectivities on process performances (Hybrid case). CO_2 permeance = 12000 GPU, CO_2/O_2 selectivity = 15 and CO_2/H_2O selectivity = 1.

5.5.2 CO_2/O_2 selectivity

CO_2/O_2 selectivity has also been examined and a sensitivity analysis for the hybrid design is shown in Figure 5.11. It can be observed that values lower than 15 affect both energy consumption and final CO_2 purity. For higher values, the effect on the final purity is most significant. For this analysis, a dryer is used before compression of the high-purity stream to 15 MPa: it has been simulated as component splitter into UniSim® Design and its energy consumption is added to the power requirement, despite not being a significant contribution. This assumption can be considered as consistent with the choice of a drying unit (e.g. silica bed) [65]. It is also important to point out that a CO_2/O_2 selectivity of 50 guarantees a final Oxygen content of 200 ppm which meets the requirements for storage [34].

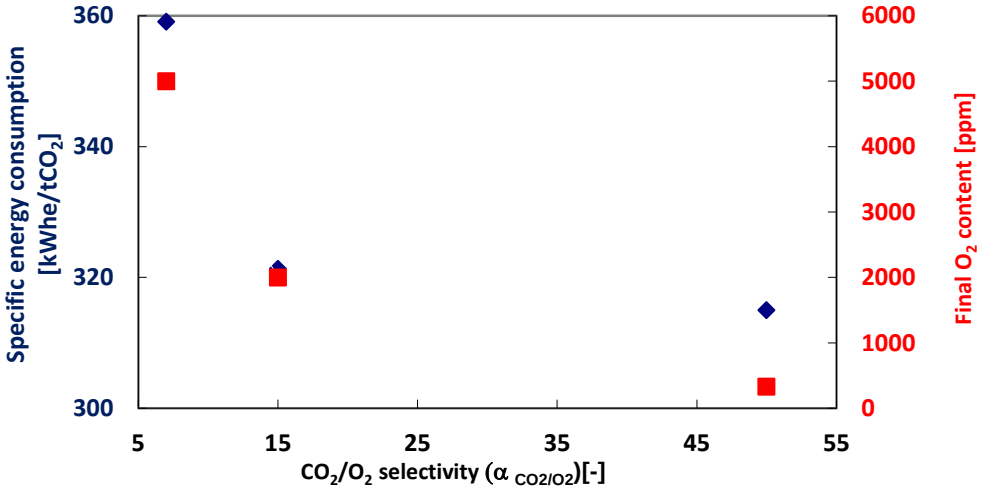

Figure 5.11: Effect of CO_2/O_2 selectivity on the performances, Hybrid design. CO_2 permeance = 12000 GPU, CO_2/N_2 selectivity = 50 and CO_2/H_2O selectivity = 1.

The possible Oxygen loss was underlined in the case of selective exhaust recycling configuration, due to its back-permeation in the counter-current stage with air as sweep. An analysis on the selective exhaust recycling configuration, considering membranes with different CO_2/O_2 selectivities, has been also performed. Since for values higher than 15 there is no significant effect on energy consumption, two materials are assumed:

- Membrane A: CO_2/O_2 selectivity of 15
- Membrane B: CO_2/O_2 selectivity of 50.

The other properties remain constant according to the material assumptions. Three cases have been considered:

- Case 1: membrane A for all the stages.
- Case 2: membrane A for (high-recovery) stage 1 and membrane B for (high-purity) stage 2 and 3. This option can avoid Oxygen losses from the combustion air and a higher CO_2/O_2 selectivity in stage 3 lowers the amount of Oxygen to the compression train.
- Case 3: membrane B for all the stages.

The results for the different cases are reported in Figure 5.12: it can be observed that a higher selective membrane in stage 2 and 3 can guarantee both an Oxygen content of approximately 20 % in the flue gas and a lower O_2 content in the final stream. The selectivity in stage 1 does not appear to affect the performances. This can be an indicator for the use of membranes with different characteristics in the multi-stage design. Additionally, considering that stage 2 and 3 represent 35 % of the total membrane area as reported in Figure 5.13, no significant changes are expected in capital costs, even if materials with lower CO_2 permeances (and therefore higher selectivities) are considered. The effect of lower Oxygen content to the boiler is not discussed in detail in this thesis; however, it is evident that, particularly for case 2 – 3, the effect of lower Oxygen content in the boiler should be investigated. This is an important point of discussion since transport and storage requirements should be taken into consideration. Consequently, the Oxygen content in the final stream is one of the key parameters.

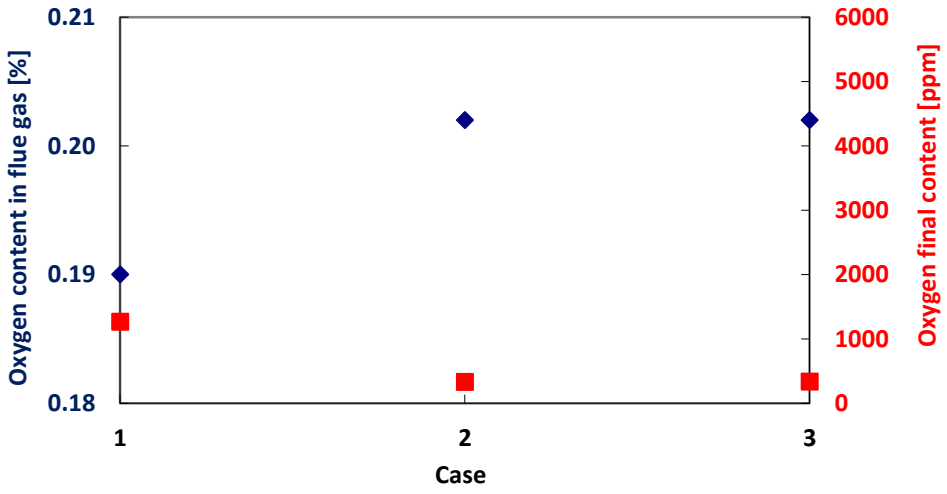

Figure 5.12: Oxygen to the boiler and final Oxygen content in the Selective Exhaust Gas Recycling design for the different cases. CO_2 permeance = 12000 GPU, CO_2/N_2 selectivity = 50, CO_2/O_2 selectivity = 15 and CO_2/H_2O selectivity = 1.

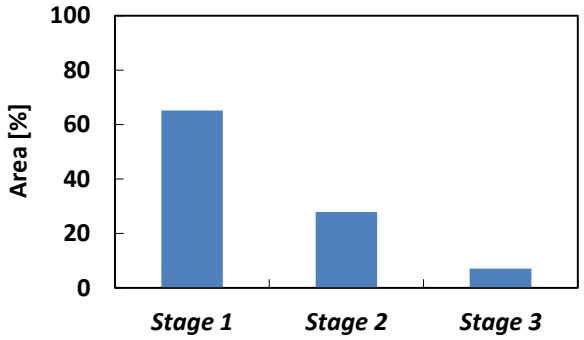

Figure 5.13: Area distribution among the three membrane stages (Figure 5.8) for the Selective Exhaust Gas Recycling design.

5.5.3 Water content in the flue gas

One of the assumptions in the process design is an inlet temperature to the membrane modules of 298 K. A parametric analysis is conducted here considering different water molar fractions in the flue gas, directly related to the inlet temperature [48]. In addition to the base case (298 K and 3 % water content), a water molar fraction of 9 %, corresponding to an inlet temperature of 323 K and a dry feed, have been simulated. The last option corresponds to the assumption of a drying unit before the capture system.

In Figure 5.14 the results for the hybrid design are presented in terms of energy consumption and membrane area. According to Merkel et al. [39], water is identified as an internal sweep because of its high permeability. Due to the high permeance assumed in this study, even at high concentration its effect does not appear to significantly affect the required membrane area for the hybrid design (± 2 %). The lower power required for lower water concentrations is justified by the vacuum/compression duty, since water permeates through the film due to the assumed high permeance. However, additional heat requirement and heat exchanger costs are expected for the 298 K case compared to the simulation at 323 K. Preliminary calculations did not show a significant drawback in capital cost between

298 K and 323 K cases compared to the benefit in terms of reduced energy requirement. Despite not being investigated in this study, the dry option should take into account the additional capital cost due to drying unit as shown in Hasan et al. [36].

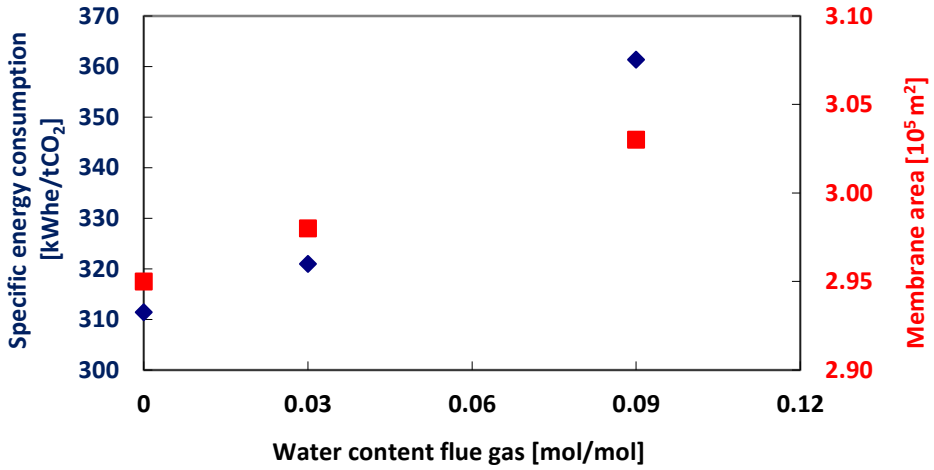

Figure 5.14: effect of inlet water composition on the performances for the Hybrid case. CO_2 permeance = 12000 GPU, CO_2/N_2 selectivity = 50, CO_2/O_2 selectivity = 15 and CO_2/H_2O selectivity = 1.

5.5.4 Conclusion

In this Chapter different process designs have been presented and the results have been expressed in terms of membrane area and energy consumption.

In particular, the importance of both CO_2/N_2 and CO_2/O_2 selectivities has been discussed and optimal material characteristics have been suggested. It has been shown that a CO_2/N_2 selectivity of 50, which is commonly adopted in the literature, can also be beneficial in terms of overall energy consumption compared to lower values. The importance of CO_2/O_2 selectivity has also been demonstrated and a value comparable to CO_2/N_2 selectivity would guarantee Oxygen content in the final

stream of 200 ppm. Additionally, the importance of Oxygen selectivity was also shown for the selective exhaust gas recycling option where a value of 50 would reduce Oxygen losses in the counter-current stage with air as sweep. The effect of water content in the flue gas has also been studied and no significant effect on membrane area was observed due to the high water permeance assumed in this work. However, the resistance of the material to humid conditions is a key requirement as this would also avoid the installation of a drying unit before the membrane skids.

In order to have more detailed simulations, it is important to achieve better predictions of module behaviour. Drawbacks as pressure drops are expected to affect the overall performances as evident from the single-stage simulations reported in Chapter 3. Therefore, the economic analysis presented in the next Chapter will also include a parametric analysis considering the possible effects of pressure drops.

Chapter 6: Economic Analysis

The aim of this Chapter is to link the previously presented process simulations to a rigorous economic analysis.

Initially, the methodologies proposed in the literature are analysed, with particular attention to the available reports on CCS from different international organisations and governments. The attention is then focused on Levelised Cost of Electricity (LCOE) and its complete evaluation is presented, focusing on the key process and membrane parameters.

6.1 Introduction: parameters and main indicators

Once a robust process simulation is obtained, an economic analysis is essential to evaluate the feasibility of membrane separation in comparison with different technologies. Several international organisations report detailed methodologies for carbon capture requirements and cost targets [63-65, 144].

The most common parameter used in CCS process analyses is the capture cost and typical values for amines are in the range 40 - 100 $/t$_{CO_2}$. The formulation from Merkel et al. [39] is reported in Eq. (6.1), where **C** is the capital cost, **E** is the energy cost and $\mathbf{F_{CO2}}$ is the annual CO_2 captured flow rate. **T** is the annual operating time **E** the cost of energy and **P** is the nominal output.

$$CC = \frac{P \cdot T \cdot E + 0.2 \cdot C}{F_{CO2} \cdot T} \tag{6.1}$$

Considering membrane capture evaluations, Merkel et al. [39] report a capture cost of 39 $/t$_{CO_2}$ and 23 $/t$_{CO_2}$ for hybrid and selective exhaust recycling option, respectively. Alsehri et al. [60] propose an optimisation with respect to the capture

cost from Merkel et al. [39]. It is shown that values lower than 18 $/t$_{CO_2}$ can be achieved if CO_2 permeances higher than 2000 GPU and CO_2/N_2 selectivities higher than 50 are considered. According to Ramasurbramainan et al. [61] a capture cost lower than 24 $/t$_{CO_2}$ is achievable. A more conservative value of 42.1 $/t$_{CO_2}$ is reported by RTI international [70] for the proposed three-stage boiler design.

A more complete capture cost estimation can be found in Zhao et al. [45] who present a formulation including also Operation and Maintenance (O&M) costs. The formulations are reported in Eq. (6.2) - (6.5), where:

- Suffixes *O&M* and *en* refer respectively to Operation and Maintenance and Energy contributions;
- $\mathbf{I_c}$, $\mathbf{I_{vp}}$, $\mathbf{I_{ex}}$, $\mathbf{I_{he}}$, $\mathbf{I_m}$ and $\mathbf{I_{mf}}$ are respectively the costs of compressors, vacuum pumps, expanders, heat exchangers, membranes and membrane frames;
- **a** and $\mathbf{a_m}$ represent annualised factors for equipment and membrane contribution;
- **T** and **P** are the annual operative time and power output.

$$CC = \frac{C + C_{O\&M} + C_{en}}{F_{CO2} \cdot T} \tag{6.2}$$

$$C_{cap} = a\ (I_c + I_{vp} + I_{ex} + I_{he}) + a_m\ I_m \tag{6.3}$$

$$C_{O\&M} = 0.036\,(I_c + I_{vp} + I_{ex} + I_{he}) + 0.01\,(I_m + I_{mf}) \tag{6.4}$$

$$C_{en} = T\ P\ E \tag{6.5}$$

As a result of their analysis, Zhao et al. [45] evaluate a capture cost of 24 €/t$_{CO_2}$ but for a CO_2 recovery of 70 %. This methodology represents the starting point for the economic analysis carried out in this thesis.

Another cost parameter used in gas separations is the Gas Processing Cost *(*GPC*)*, described by Hao et al. [145]. Estimated values for amines are 1.71 $/MSCF (~ 30

$/t_{CO_2}$) for capture and 0.42 $/MSCF (~ 13 $/$t_{CO_2}$) for compression and drying process [59]. Hussain and Hägg [59] report a value for the capture system lower than 1 $/MSCF (~ 18 $/$t_{CO_2}$) achievable for their multi-stage membrane design.

In order to have an idea of the repercussion of the capture system on the plant performances, the Levelised Cost Of Electricity (LCOE) is chosen for this analysis among the different indicators presented in the literature. LCOE represents the ratio of the net present value of total capital and operating costs of a particular plant to the net present value of the net electricity generated by that plant over its operating life [64, 65]. The formulation is reported in Eq. (6.7), where $\mathbf{F_t}$ is the fuel cost and **r** is the discount rate [64].

$$LCOE = \frac{\sum_{t=1}^{n} \frac{I_t + M_t + F_t}{(1+r)^t}}{\sum_{t=1}^{n} \frac{C_f \cdot E_t}{(1+r)^t}} \tag{6.7}$$

The results for LCOE estimations are commonly reported in terms of relative increase. If base and capture cases are estimated under the same assumptions, its relative increase can be considered as a consistent parameter.

Different estimations are proposed in the literature for amine capture [64, 144, 146]. It needs to be pointed out that these are based on an already commercial technology and, therefore, a higher accuracy can be considered in comparison to candidate alternative technologies as membrane separation. ZEP (Zero Emission Platform [63]) calculates a base LCOE for coal-fired power plants of 45 €/MWh, while for Mono Ethanol Amine (MEA) capture a base of 75 €/MWh (state-of the-art) and an optimal of 70 €/MWh are identified. IEA [144] reports an increase in LCOE of 63 % (calculated as average among OECD countries) and UK DECC [147] evaluates an increase from 95.8 £/MWh (no capture) to 108.3 £/MWh (capture) including carbon cost.

Cost of electricity calculations are also reported for membranes. Considering DOE-funded projects [78], an increase in the range 73 - 82 % is reported by RTI international [70], and Kulkarni et al. [68] calculate a potential increase in LCOE of 48 - 53 %. Ramasurbramanian et al. [61] - assuming a membrane price of 27 \$/m^2, a CO_2 permeance of 3000 GPU, a CO_2/N_2 selectivity of 140 and blower at the feed side – calculate a relative increase in COE is 33 % and a capture cost lower than 24 \$/t_{CO_2}. Zhai et al. [43] evaluate a relative increase in LCOE of 97 % (Retrofit) and 65 % (Selective Exhaust Gas Recycling) but the same net power output compared to the base case is assumed.

6.2 LCOE evaluation

For the purpose of this analysis, an LCOE evaluation based on the methodologies from UK Department of Energy and Climate Change [64, 147] and European Zero Emission Platform [63] is carried out. The main idea is to integrate the available methodology for amines with a rigorous calculation which includes membrane capture contribution.

Cost parameters, such as capture cost, can give important indications but their calculation is on an annual basis. In the case of LCOE, a rigorous evaluation can give important guidelines for long-term applications such as plants with CCS.

Eq. (6.7) is consequently modified into Eq. (6.8), where suffix **CC** refers to carbon capture contribution; storage costs ($I_{storage}$) are also added.

$$LCOE = \frac{\sum_{t=1}^{n} \frac{I_t + M_t + F_t + I_{tCC} + M_{tCC} + I_{storage} + I_{\text{carbon cost}}}{(1+r)^t}}{\sum_{t=1}^{n} \frac{C_f \cdot E_t}{(1+r)^t}} \tag{6.8}$$

The cost parameters for the base case plant are assumed as n^{th} of a kind (NOAK) coal-fired power plant [147]. The choice of using NOAK parameters implies that the technology in the field is already mature and a number of plants are built. This is a reasonable assumption in the case of a coal-fired power plant with FGD. Capital costs include contributions of pre-licensing, regulatory, EPC (Engineering and Procurement costs) and Infrastructure costs. Operation and Maintenance costs include fixed and variable fees, accounting for an annual escalation factor of 2 % and an average fuel cost estimation is assumed [146].

A list of the main parameters used in the calculation is reported in Table 6.1. It is important to point out that the calculation is made assuming 2013 as base year and the Euro as the base currency. If not referred to 2013, the values for capital and O&M costs in Table 6.1 are updated to the base currency assuming an annual inflation rate of 3 % [148]. The average exchange rate for 2013 [149] is adopted if the reference is based on a different currency.

GENERAL	**BASE**	**CCS**	
Plant life [147]	40		[years]
Discount rate [147]	0.1		[-]
FUEL			
Fuel cost [146]	2.4		[€/GJ(LHV)]
Fuel escalation cost (year) [146]	0.015		[-]
CAPITAL COSTS			
Pre-licensing costs [147]	25	25	[£/kW]
Regulatory + licensing [147]	0.2	1.5	[£/kW]
EPC cost [146]	1555	2450	[€/kW]
Infrastructure cost [147]	22.5	22.5	[£/kW]
O&M (*Operation and Maintenance*)			
O&M fixed fee [147]	35000	35000	[£/MW/y]
O&M variable fee [147]	1	2.5	[£/MWh]
O&M escalation cost (year) [147]	0.02	0.02	[-]
Insurance [147]	2500	4400	[£/MW/y]
Connection and Use of System charges [147]	5050	5050	[£/MW/y]
STORAGE			
CO_2 transport and storage [147]	0	7.8	[£/MWh]

Table 6.1: Parameters used for the LCOE calculation.

The calculation of capital and O&M contributions to LCOE follow Eq. (6.3) - (6.4) and membrane parameters are taken from the capture cost estimation from Zhao et al. [45]. A membrane price of 50 €/m^2 is considered and it is also assumed that the membranes are changed every 5 years [45], while the skids and the equipment twice in the life of the plant (an average life of 25 years for the membrane skids is assumed [45]). The costs for compressors, expanders and vacuum pumps are taken from Zhai et al. [43]. In order to have a conservative estimation, the refrigeration cost is assumed three times the vacuum pump cost. In Table 6.2 examples of rotating equipment costs from the literature are presented (if not specified, the same reported value is for compressor, vacuum pumps and expanders). In the presented analysis it has been observed that compression equipment cost does not have a significant impact on the final capital cost. As discussed in Chapter 2, the most important assumption in terms of compressor equipment is the adiabatic efficiency which has a dramatic impact on the calculated energy consumption. However, compression cost has been identified as an important assumption by Kulkarni et al. [70] due to the high compression power required in their hybrid option. A difference in LCOE – relative increase from 53 % to 48 % - was achieved when considering the scale factor for compressors.

Ref.	Equipment cost
[39, 41, 44]	500 $/kW
[61]	620 $/KW
[43]	Compressor 671 $/kW, Vacuum Pump 1341 $/kW, Expander 500 $/kW
[70]	330 – 867 $/kW

Table 6.2: Example of compressor equipment cost from the literature.

Since the capture cost calculation in Zhao et al. [45] is on an annual basis, an O&M escalation factor of 1.5 % equal to the base case is applied in the proposed LCOE methodology. In the case of unknown parameters for the membrane capture case (e.g. insurance and licensing costs) they are taken from the amine analysis as 1st of a kind (FOAK). In this case, the assumption of FOAK parameters is justified since LCOE is predicted for a new-built plant with carbon capture.

A Levelised Cost Of Electricity estimation using amine technology – based on DOE case 9 (subcritical coal-fired power plant [24]) using Mono Ethanol Amine (MEA) capture as retrofit, developed by Ahn et al.[20], has been adopted to conduct a comparison with membranes. The cost parameters for the calculation are considered as 1st of a kind amine technology [64]. Transport and storage costs are assumed equal for both amine and membrane technology according to UK DECC guidelines [64].

The calculation reported in this thesis takes into account the possible contribution of carbon cost, which is expected to play a key role for future energy scenarios [64, 147]. A carbon cost scenario is assumed in line with the UK DECC evaluations [64, 147, 150]: an emission cost of 20 €/t_{CO_2} has been assumed for 2020 with an escalation factor of 1 €/year.

6.3 Results and discussion

Under the previously discussed assumptions, the results are now presented. The membrane designs included in this evaluation are hybrid and selective exhaust gas recycling configurations.

As a starting point for the analysis, capture costs are evaluated. The reference calculation and methodology is based on Eq. (6.2) - (6.5) with the modifications previously discussed for LCOE, assuming an energy cost updated to the current

European price [151]. As a result of the calculation, a capture cost of 26 €/t_{CO_2} is identified for the hybrid option and a value of 23 €/t_{CO_2} for the selective exhaust gas recycling configuration. It is important to point out that second design has the benefit of reducing the capture costs of 10% compared with the retrofit case. In order to evaluate the different cost contributions, in Figure 6.1 capital, operation and maintenance and energy costs are presented. The main difference between the two options is the energy cost contribution which is higher for the hybrid case due to the additional energy consumption. On the other hand, the difference in capital cost between the two designs (approximately 5 %) is less remarkable.

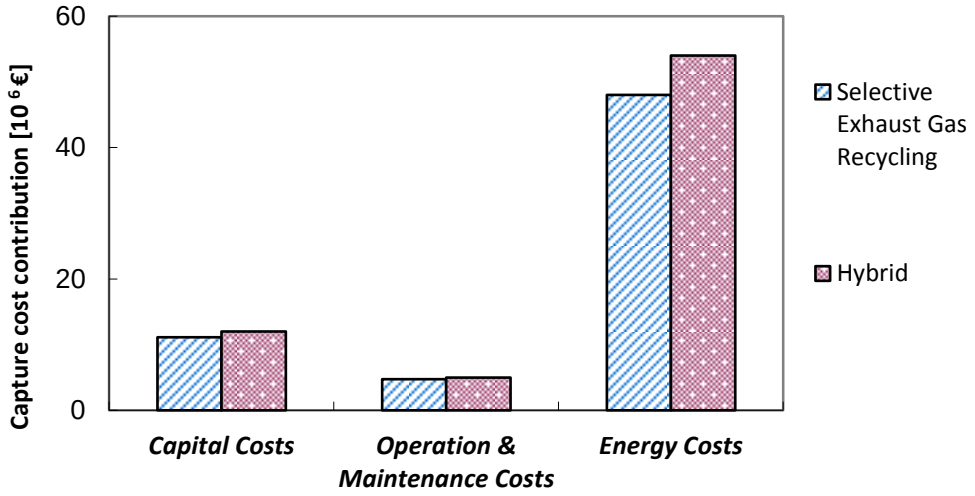

Figure 6.1: Distribution of the capture costs for Hybrid and Selective Exhaust Gas Recycling options. Membrane properties: CO_2 permeance = 12000 GPU, CO_2/N_2 selectivity = 50, CO_2/O_2 selectivity = 15 and CO_2/H_2O selectivity = 1.

In Figure 6.2 the LCOE evaluation is presented for hybrid, selective exhaust gas recycling and amine simulations. Assuming no carbon cost contribution, the increase in LCOE compared to the base-case for membrane separation ranges from 91 % (selective exhaust gas recycling) to 100 % (hybrid), which is consistent with calculations using amines previously carried out [63, 147]. Additionally, the cost without accounting for transport and storage is consistent with the values reported by IEA [144] with an increase of 65 %. If a carbon tax scenario is assumed, a relative

increase of 24 - 30 % for membranes is calculated. Additionally, a reduction for both membrane cases in terms of LCOE difference compared to amine capture (including carbon cost) is also shown (7 - 13 %).

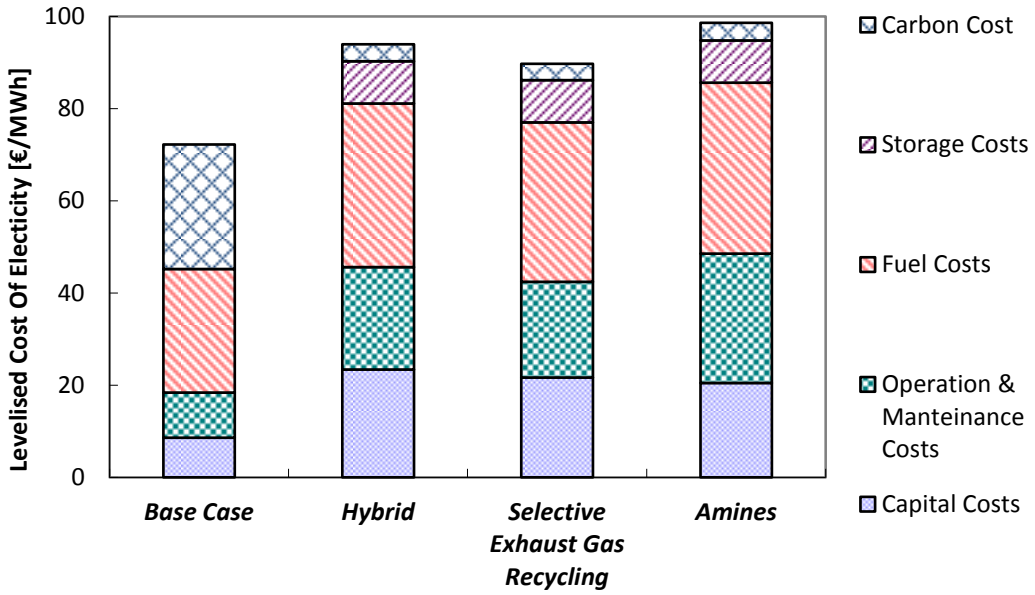

Figure 6.2: Levelised Cost Of Electricity (LCOE) comparison for the simulated cases. Membrane properties: CO_2 permeance = 12000 GPU, CO_2/N_2 selectivity = 50, CO_2/O_2 selectivity = 15 and CO_2/H_2O selectivity = 1.

As already pointed out in the capture cost analysis, the main benefit for the selective exhaust gas recycling option compared to the hybrid case is the reduced energy consumption which implies a higher power output for this design. This directly affects the denominator of the LCOE calculation reported in Eq. (6.8). On the other hand, the reduction in membrane area compared to the hybrid configuration accounts for approximately 5 % reduction in capital cost. Apart from the improved results in terms of LCOE, the reduced footprint for the selective exhaust gas recycling option should be underlined, as already discussed in Chapter 5.

In conclusion of this section, in Figure 6.3 LCOE calculation for membranes is shown, assuming the same net output (550 MW). This evaluation can be a realistic scenario considering a new-built power plant with CCS and it is consistent with the

analysis from Zhai et al. [43]. The difference in LCOE calculated in this work is 56 - 62 % without carbon cost and 14 - 18 % assuming a carbon cost scenario. The improved results for all the designs compared to Figure 6.2 are due to the higher power output in the denominator in Eq. (6.9), which lowers the different contributions to LCOE.

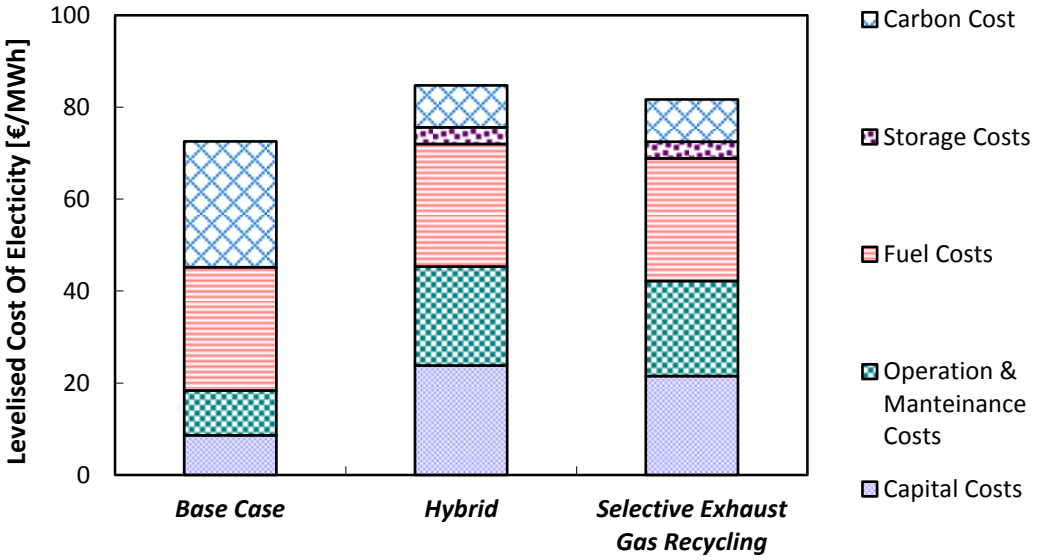

Figure 6.3: Levelised Cost Of Electricity (LCOE) evaluation - same net power output. Membrane properties: CO_2 permeance = 12000 GPU, CO_2/N_2 selectivity = 50, CO_2/O_2 selectivity = 15 and CO_2/H_2O selectivity = 1.

Despite relying on the assumption of optimal material characteristics, the simulated membrane designs show promising results in terms of LCOE. In particular, the improved performances of the selective exhaust gas recycling option compared to the hybrid case are mainly related to the lower energy consumption and resulting higher power output. On the other hand, the reduction in capital cost (approximately - 5 %) does not appear to have a significant contribution despite the 24 % lower area. This is evident from both capture cost and LCOE calculations. However, both CO_2 permeance and membrane price are two key assumptions and these parameters will be discussed in the next section.

6.4 Parametric analysis

For the parametric analysis presented in this section, membrane permeance and its price are chosen among membrane properties. Pressure drops are selected as a process parameter. The following parametric analysis is carried out on the basis of the results shown Figure 6.2, assuming same gross power output.

Considering membrane properties, CO_2 selectivities over the other components in the flue gas play a key role, since they directly affect the energy consumption. A more selective membrane implies less impurities in the permeate stream, therefore lower power requirement for vacuum pumps and compression system and higher final CO_2 purity. In the previous chapter the importance of CO_2/O_2 selectivity was underlined and its effect on the final Oxygen content was investigated. It was found that an Oxygen permeance similar to Nitrogen (and therefore similar CO_2/N_2 and CO_2 selectivities) is required to achieve an Oxygen level of 200 ppm in the final high-purity steam. In this section the attention is focused on membrane CO_2 permeance. In Figure 6.4 the combined effect of CO_2 permeance and membrane price is shown for the hybrid design. It can be observed that with a CO_2 permeance of 5000 or higher, which is in line with current research targets, the capital cost is not significantly affected by membrane price. If a membrane with a CO_2 permeance higher than 10000 GPU is adopted, this effect appears even less significant: the membrane area is so low that its contribution to the overall capital cost is not relevant. This also explains the previous results for both carbon cost and LCOE, which were not significantly affected by the difference in membrane area between selective exhaust gas recycling and hybrid designs.

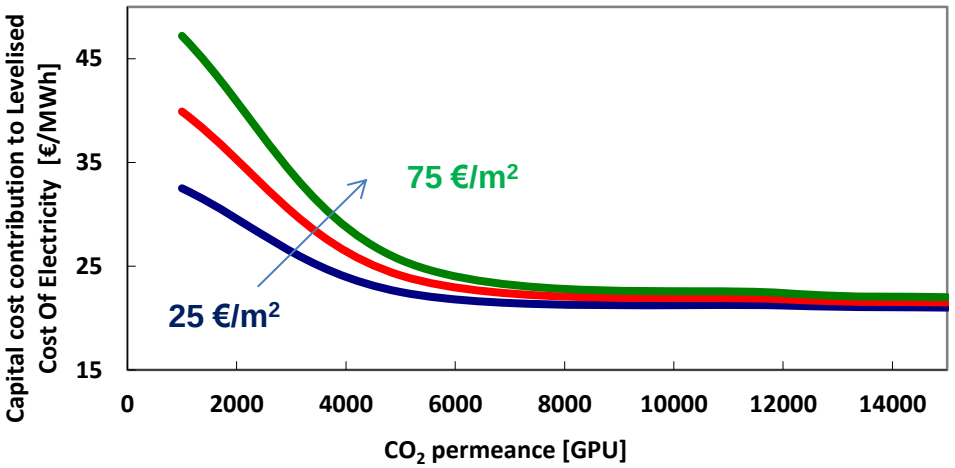

Figure 6.4: Capital cost contribution with respect to membrane CO_2 permeance and price for the hybrid design. Membrane properties: CO_2/N_2 selectivity = 50, CO_2/O_2 selectivity = 15 and CO_2/H_2O selectivity = 1.

Pressure drops have been identified as an important parameter to be taken into account in Chapter 3, where it was shown that module parameters should be carefully designed according to membrane properties. In the case of hollow-fibre simulations, it is realistic to expect a higher membrane area due to pressure drops compared to the simulations based on non-dispersed plug-flow models. The effect on LCOE from increased membrane area of the counter-current stage for the hybrid design is shown in Figure 6.5, where the area for stage 1 is reported on the x axis. Simulations assuming a CO_2 permeance of 5000 GPU are also reported, consistently with the analysis in Chapter 3 and to confirm the results shown in Figure 6.4. The cost contribution is less affected in the case of high CO_2 permeance and this is confirmed by the different slope of the two trends. In the realistic case of increased membrane areas compared to the base-case simulation, an additional relative increase in LCOE should be expected.

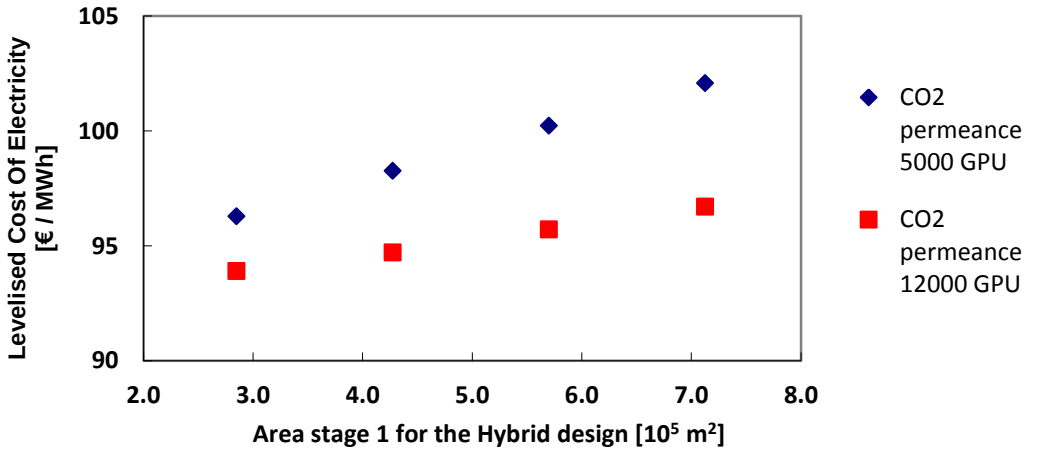

Figure 6.5: Effect of stage 1 area on Levelised Cost Of Electricity for different CO_2 permeances. CO_2 permeance = 12000 GPU and 5000 GPU, CO_2/N_2 selectivity = 50, CO_2/O_2 selectivity = 15 and CO_2/H_2O selectivity = 1.

Not only membrane area is expected to be affected by pressure drops, but also energy consumption. In particular, simulations are run considering pressure drops on the shell side of stage 1 in the hybrid case: this implies additional compression of the feed to allow its flow through the module. Consequently, the energy penalty compared to the base case is the increased duty for compression. In Figure 6.6 the effect of stage 1 retentate pressure drops on energy consumption and LCOE is shown: an almost linear trend can be observed for both LCOE cost and energy consumption. In particular, for pressure drops of 10 % (12 kPa) there is a penalty of approximately 2 % on LCOE.

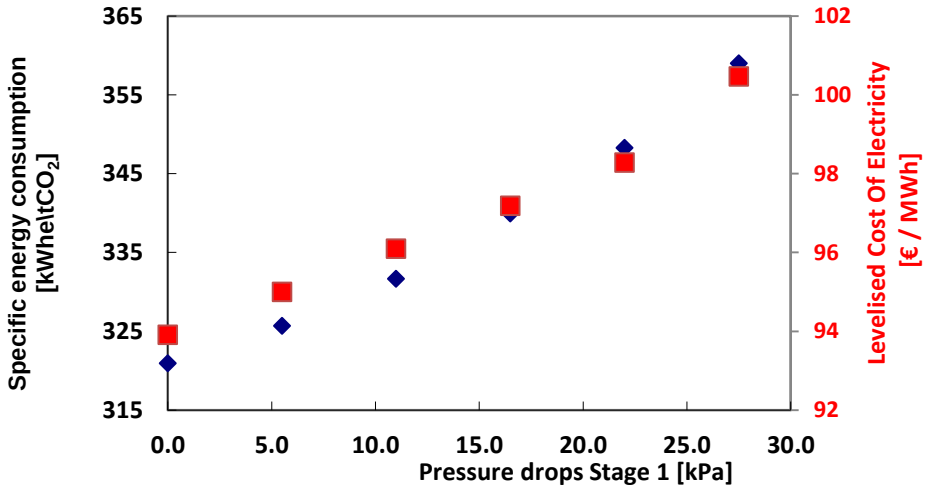

Figure 6.6: Effect of stage 1 shell-side pressure drop on LCOE and energy consumption. CO_2 permeance = 12000 GPU, CO_2/N_2 selectivity = 50, CO_2/O_2 selectivity = 15 and CO_2/H_2O selectivity = 1.

In Figure 6.7 a 3D plot which combines the effect on LCOE of increased membrane area and energy consumption for stage 1 in the hybrid case is shown. This can give more realistic indications in terms of membrane performances and repercussion on the economic parameters. For example, if pressure drops in the range 10 - 20 kPa are encountered, and an increase of at least 50 % membrane area is assumed compared to the base case simulations, an additional LCOE relative increase of approximately 5 % can be a more realistic prediction. Therefore, this analysis can give guidelines for the tolerable pressure drops and its consequences on the overall plant performances.

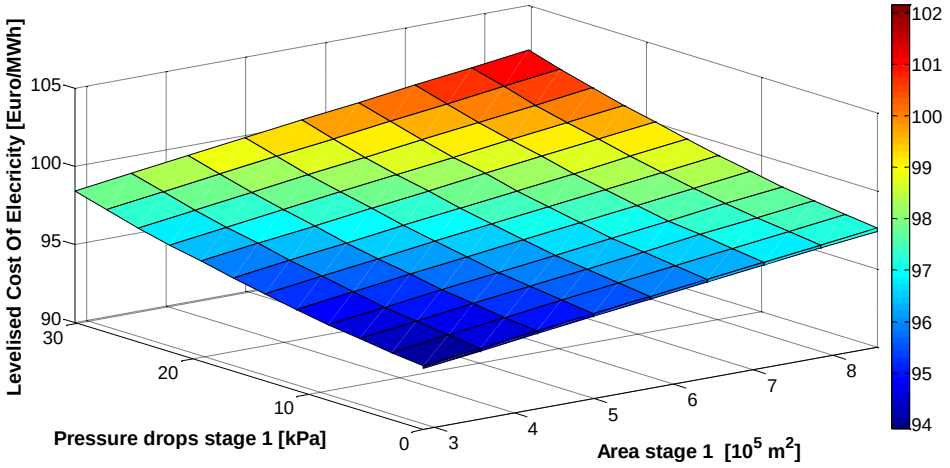

Figure 6.7: Combined effect of shell side pressure drop and increased membrane area for stage 1 on Levelised Cost Of Electricity for the hybrid case. CO_2 permeance = 12000 GPU, CO_2/N_2 selectivity = 50, CO_2/O_2 selectivity = 15 and CO_2/H_2O selectivity = 1.

From the reported analysis, the importance of a rigorous and detailed economic evaluation is evident. Despite still being dependent on process assumptions and market basis, the proposed LCOE evaluation aims at having a realistic and consistent prediction compared to the available literature.

6.5 Targets for carbon capture applications

In both Chapter 5 and 6, key material and process parameters have been investigated in the parametric analyses to evaluate the feasibility of membrane technology for post-combustion carbon capture.

First of all, it should be underlined that the calculations carried out in this thesis are based on optimal material characteristics which do not yet correspond to commercially available polymers.

However, some indications can be given:

- CO_2 permeance has been widely investigated in the literature and a value of 1000 GPU is commonly used as benchmark. It has been shown that a membrane with a CO_2 permeance of at least 5000 GPU would already guarantee a feasible separation in terms of capital cost for the membrane skids. However, since a higher area estimation compared to the base simulations is expected if pressure drops are considered, this will affect the economic performances in terms of LCOE. This effect will be less remarkable if a CO_2 permeance of 10000 GPU or higher is achieved, for which the membrane cost does not appear to significantly affect LCOE.
- A CO_2/N_2 selectivity of 50 is the base selectivity for Polaris^{TM} 1st generation. It has been shown here that this value can guarantee better overall performances in terms of energy consumption compared to lower CO_2/N_2 selectivities. Additionally, considering that membranes for carbon capture applications are expected to work under pressure ratio limited regime, this value can be considered as a consistent benchmark.
- The effect of CO_2/O_2 selectivity is not widely investigated in the literature. Here a parametric analysis has been conducted and its importance for the final Oxygen content has been shown. In particular, a value above 15 is required not to penalise the energy consumption, but also a comparable selectivity to CO_2/N_2 is required if a target value of 200 ppm in the final stream is assumed. Additionally, the importance of CO_2/O_2 selectivity in the selective exhaust gas recycling design has been demonstrated since the Oxygen content to the boiler is a key parameter for this design.

Therefore, it appears that the targets for Polaris^{TM} advanced (CO_2 permeance above 5000 GPU and CO_2/N_2 selectivity of 50) have the potential to achieve competitive performances in terms of LCOE. A material with these characteristics would guarantee a reduction in membrane area by keeping low energy consumptions. However, durability and resistance to humid conditions are key factors for material development and pilot projects with real flue gas conditions are essential for this

evaluation. In fact, one of the main assumptions is that membranes are changed every 5 years which is a lifetime achievable by commercial natural gas separation membranes [26].

It is also suggested that process conditions need to be carefully taken into account and this is strictly related to an effective modelling analysis. Particular attention should be focused on pressure drops in terms of process design as the compression/blower system needs to be able to cope with pressure drops along the membrane skids. In Chapter 4, it was shown that optimal module geometries also need to be tailored to specific material characteristics. This is particularly important for carbon capture applications, where a CO_2 permeance 10 times or even higher than commercial materials need to be achieved. Additionally, the conditions in the first stage need to be carefully considered since a pressure ratio limited regime is expected due to the low CO_2 inlet composition and the low pressure ratio adopted in the presented simulations. Therefore, significant pressure drops are expected to affect the maximum achievable purity in this stage.

In conclusion, it is evident that further research effort is needed to achieve membrane characteristics, such as CO_2 permeance higher than 5000 GPU, CO_2/N_2 selectivity of 50 and comparable CO_2/O_2 selectivity. A stable material with these characteristics, assembled in modules designed to minimise pressure drops, would guarantee competitive performances with the conventional absorption solutions.

Chapter 7: Conclusion

The work carried out in this thesis focused on different topics: mathematical modelling, software customisation, process simulations and economic analysis.

A detailed modelling investigation of membrane gas separation has been developed and an analysis from stage to module performances has been carried out. Simulations with different levels of accuracy have been run and the bi-dimensional models can be an important starting point for improved module design. The implemented models can also be a useful tool to evaluate module performance, defects and flow mal-distributions, which can also be taken into account. For example, the effect of channel thickness on pressure drops for spiral-wound modules can be studied, as well as fibre diameter and layout for hollow-fibre permeators. Therefore, optimal operating conditions can be calculated to guarantee tolerable pressure drops and optimised module geometries with respect to material characteristics can be studied.

Typical high-pressure conditions for membrane separations have also been simulated, in order to test the implemented models. For example, important indications in terms of Joule-Thomson effects can be obtained and this can avoid undesirable condensations inside the modules. While each of these effects may appear to have a small impact on the separation performance, taken overall they become very important in CCS applications, where the requirements imposed on the process include both high purity and high recovery. The advanced membrane module simulators developed in this work capture all the major effects and can be embedded in a fully integrated process simulation of the power plant and capture unit.

The preliminary dynamic simulations showed promising results in terms of a fast response of the membrane units to a change in process conditions. This represents a key aspect in terms of future flexible CCS applications.

The customisation of UniSim® Design has been a key step in this process and the developed integration offers the possibility of adding new unit operations to the commercial simulator.

Thanks to the developed interface between in-house models and UniSim® Design, a complete overview of post-combustion carbon capture feasibility for membrane gas separation has been carried out. Starting from the available literature, different multi-stage process configurations have been designed, with the aim of reducing both membrane area and energy consumption. A wide range of options has been investigated: a retrofit configuration where only membranes are considered, a hybrid option with a refrigeration stage and a possible modification of the whole power plant scheme including recycle of part of the CO_2 to the boiler.

The simulations presented in this thesis aim at highlighting the key contributions and evaluating their effect on the overall plant performances towards a complete feasibility study for CCS applications. The attention has been focused on the final composition of the CO_2-rich stream, particularly in terms of Oxygen content due to different CO_2/O_2 selectivities. If a CO_2-N_2 selectivity of 50 is assumed (a value which is commonly adopted in the literature), the same value for CO_2/O_2 would guarantee Oxygen content lower than 200 ppm in the final stream. Considering the selective exhaust gas recycling design, the possibility of using membranes with different properties has also been considered. In fact, a key contribution is played by CO_2/O_2 selectivity in the counter-current stage with air as sweep since it directly affects the conditions in the boiler.

As expected, the main contribution for carbon capture applications is played by pressure drops. In particular, hollow-fibre simulations showed that shell-side pressure drops can be significant as they are expected to dramatically affect energy consumption and, therefore, the overall performance. The effect of a combined flow pattern has been studied in the direction of having more realistic simulations compared to the available one-dimensional plug-flow models. The investigation carried out started from the available correlations on heat exchanger design and it

represents an innovative aspect compared to the available literature on hollow-fibre modelling.

The economic evaluation enabled a more complete analysis of the membrane designs and promising results for LCOE compared to amine absorption have been shown. However, it should be pointed out that the reported simulations are based on optimal material characteristics. Parametric analyses have been carried out and, despite the optimistic assumption of the materials taken initially, it was shown that a CO_2 permeance in line with the current research targets – a CO_2 permeance of 5000 GPU or higher - already has the potential of giving promising results. Capture cost has been evaluated and compared with the available literature. Pressure drops have also been taken into account and an additional difference in 5 % in LCOE relative increase can be a realistic indication. If a carbon cost scenario is assumed, the potential of achieving a difference in LCOE lower than 35 % is shown, as stated by US DOE guidelines. In fact, a relative increase in LCOE of 24 - 30 % has been identified for a 550 MW coal-fired power plant, assuming the same gross power output.

Promising perspectives for CCS applications have been shown and constant attention has also been dedicated to international and national publications, in order to achieve a complete and rigorous economic analysis. However, more detailed models accounting for the transport through the membrane film are needed to give more realistic predictions. This, in addition to a more detailed economic evaluation, could provide additional insight into carbon capture feasibility. In this direction, studies on real flue gases and pilot plant tests will be a key part of the research in the next few years. The results currently achieved show promising perspectives for membrane application to post-combustion carbon capture from coal-fired power plants.

Appendix A: List of symbols

Table III: List of abbreviations used throughout the thesis – Part 1.

ASU	Air Separation Unit
Barrer	Unit for permeability
CC	Carbon Capture
CCS	Carbon Capture and Storage
CHP	Combined Heat Power
CO2CRC	Cooperative Research Centre for Greenhouse Gases Technologies
DECC	(UK) Department of Energy and Climate Change
DOE	US Department of Energy
EOS	Equation Of State
EP	Electrostatic Precipitator
EPC	Engineering and Procurement
ETS	(European Union) Emission Trading Scheme
EUAs	Emission Unit Allowances (for EU ETS scheme)
FD	Finite Differences (method)
FGD	Flue Gas Desulphurisation
FOAK	First Of A Kind
GHG	Greenhouse Gases
GPU	Gas Permeation Unit (unit for permeance)
IEA	International Energy Agency
IGCC	Integrated Gasification Combined Cycle Power Plants
IPCC	Intergovernmental Panel on Climate Change
LCOE	Levelised Cost Of Electricity
MEA	Mono-Ethanol Amine
MMMs	Mixed Matrix Membranes
MMscfd	Million Standard Cubic Feet per Day
MTR	Membrane Technology Research Inc.
NCCC	National Carbon Capture Center
NETL	US DOE National Energy Technology Laboratory
NOAK	N^{th} Of A Kind
O&M	Operation & Manteinance
OCFEM	Orthogonal Collocations on Finite Elements Method
PEBAX	Polyether block amide
PIM	Polymers of Intrinsic Microporosity
PMM	Porous Medium Model
PPO	Poly Prophylene Oxide
PR	Peng-Robinson
PVDF	Poly-Vinilydene Fluoride

Table IV: List of abbreviations used throughout the thesis – Part 2.

SCR	Selective Catalytic Reaction
s-PEEK	sulphonated poly(ether etherketone)
SSP	System Selling Price
STP	Standard Temperature and Pressure (273.1 K and $1.013 \cdot 10^5$ Pa)
SUNDIALS	SUite of Nonlinear and DIfferential/ALgebraic equation Solvers
TEG	Triethylene glycol
TR	Thermally Rearranged
ZEP	Zero Emission Platform

Table V: Parameters used in the economic analysis with relative units.

CC	Capture cost	[€/t_{CO_2}, \$/t_{CO_2}]
C	Capital cost	[€, \$]
P	Nominal power output	[MWh]
T	Annual operating time [s]	[s]
E	Specific energy cost	[€/kWh]
$\mathbf{F_{CO2}}$	Annual CO_2 captured [kg/s]	[t/y]
$\mathbf{C_{O\&M}}$	Operation and Maintenance Cost	[€]
$\mathbf{C_{en}}$	Energy cost	[€]
a	Annualised factor for compression and heat exchange equipment	[-]
$\mathbf{a_m}$	Annualised factor for membrane and membrane skids	[-]
$\mathbf{I_c}$	Compressor cost	[€]
$\mathbf{I_{vp}}$	Vacuum Pump cost	[€]
$\mathbf{I_{ex}}$	Exchanger Cost	[€]
$\mathbf{I_{he}}$	Heat Exchanger Cost	[€]
$\mathbf{I_m}$	Membrane Cost	[€]
$\mathbf{I_{mf}}$	Membrane Frame cost	[€]
LCOE	Levelised Cost Of Electricity	[€/MWh]
$\mathbf{I_t}$	Total overnight cost	[€]
$\mathbf{M_t}$	Sum of fixed and variable operating costs	[€]
$\mathbf{F_t}$	Fuel cost	[€]
r	Discount rate	[-]
$\mathbf{C_f}$	Capacity factor	[-]
$\mathbf{E_t}$	Annual output at 100 % capacity	[MWh]
Suffix CC	Carbon Capture contribution	[-]
$\mathbf{I_{storage}}$	Storage costs	[€]
$\mathbf{I_{carbon\ cost}}$	Carbon Cost contribution	[€]

Table VI: Symbols and parameters in the modelling analysis – Part 1.

F	Molar Flow rate	[mol/s]
μ	Absolute viscosity	[Pa s]
a	Channel thickness	[m]
A	Membrane area	[m^2]
$\mathbf{A_{j,k}}$	Orthogonal Collocation matrix for first derivatives	[-]
B	Permeability coefficient for Darcy`s relationship	[m2]
b	Solution vector for generic system of nonlinear equations	[-]
C	Concentration	[mol/m^3]
D	Dispersion coefficient	[m^2/s]
$\mathbf{d_0}$	Outer fibre diameter	[m]
$\mathbf{d_e}$	Equivalent diameter for shell side	[m]
$\mathbf{D_s}$	Shell diameter	[m]
f	Friction factor for Eq. (2.35)	[-]
$\mathbf{F_{inertial}}$	Inertial contribution in Eq. (2.33)	[$kg/(m^3\ s)$]
$\mathbf{F_{viscous}}$	Viscous contribution in Eq. (2.33)	[$kg/(m^{3.75}\ s^{0.25})$]
H	Height of the module	[m]
$\mathbf{H_i}$	Enthalpy of component i	[J/mol]
$\mathbf{H_m}$	Enthalpy of the permeating mixture	[J/mol]
$\mathbf{h_m}$	Heat transfer coefficient between the two sides of the membrane	[$J/(m^2K)$]
$\mathbf{h_w}$	Heat transfer coefficient with the environment	[$J/(m^2K)$]
J(b)	System Jacobian	[-]
$\mathbf{j_f}$	Friction factor for Kern relationship	[-]
K	Friction factor for Eq. (2.34)	[-]
L	Length of the module (used for both hollow-fibre an spiral-wound modules)	[m]
$\mathbf{L_b}$	Length of each compartment	[m]
M	Mass velocity with respect to cross sectional area	[$kg/(m^2\ s)$]
NC	Number of components	[-]
ND	Number of discretisation points for FD method	[-]
NE	Number of elements for OCFEM resolution	[-]
$\mathbf{N_f}$	Number of fibres	[-]
$\mathbf{N_i}$	Flux through the membrane for component i	[$mol/(m^2\ s)$]
NP	Degree of the polymer	[-]
$\mathbf{N_r}$	Geometrical parameter for Eq. (2.35)	[-]

Table VII: Symbols and parameters in the modelling analysis – Part 2.

$\mathbf{N_{t,cc}}$	Number of tube rows crossed between baffle tips in one baffle section	[-]
Nu	Nusselt number	[-]
P	Pressure	[Pa]
Pr	Prandtl number	[-]
$\mathbf{p_t}$	Fibre pitch	[m]
r	Retentate flow per unit of width (cross-flow model)	[mol/(m s)]
$\mathbf{r_{avg}}$	Average radius	[m]
$\mathbf{R_B}$	Bypass correction factor	[-]
Re	Reynolds number	[-]
$\mathbf{r_{eq}}$	Equivalent radius for shell side	[m]
$\mathbf{R_L}$	Leakage correction factor	[-]
$\mathbf{r_{out}}$	Outer radius of the fibres	[m]
s	Standard deviation	[-]
S	Generic cross-sectional area of a fibre	[m^2]
Sc	Schmidt number	[-]
T	Temperature	[K]
t	Variable for student t distribution	[-]
U	Velocity	[m/s]
V	Permeate molar flow per unit of length (cross-flow model)	[mol/(m s)]
W	Width of the module (used for both hollow-fibre an spiral-wound modules)	[m]
x	Molar fraction	[-]
Δ	Fibre void fraction	[-]
δ	Scalar added to the solution vector u during the resolution	[-]
Δ*	Void fraction for the shell side for the compartmental model	[-]
$\mathbf{\Delta P_{bi}}$	Ideal tube bank pressure drops	[Pa]
$\mathbf{\Delta P_c}$	Cross-flow pressure drops	[Pa]
$\mathbf{\Delta P_e}$	End-zone pressure drops	[Pa]
$\mathbf{\Delta P_{total}}$	Total pressure drops	[Pa]
$\mathbf{\Delta P_w}$	Window pressure drops	[Pa]
$\mathbf{\Delta y_e}$	Dimensionless length of elements for OCFEM method	[-]
ΔL	Step for the finite different resolution in the dynamic model, Eq. (2.97)	[m]
θ	Pressure ratio (Retentate pressure/permeate pressure)	[-]
$\mathbf{\mu_w}$	Viscosity of the fluid at the wall	[Pa s]

Table VIII: Symbols and parameters in the modelling analysis – Part 3.

ξ	Friction coefficient for Eq. (2.61)	[-]
π_i	Permeance of component i	[mol/(m^2 s Pa)]
ρ	Density	[kg/m^3]
σ	Module area density	[m^2/m^3]
φ_i	Fugacity coefficient of component i	[-]
λ	Thermal conductivity	[J/(m K)]
Suffix r	Retentate side	[-]
Suffix p	Permeate side	[-]
Suffix f	Feed side	[-]

Despite SI units are used throughout the thesis, it has been chosen to report membrane permeability and permeance using the most common units in the literature, which are respectively, Barrer and GPU. These are converted to SI units when they are used in the model, following the conversion factor reported in Table IX. The F/A (Flow rate/membrane area, used in Chapter 4) conversion to SI units is also included.

Table IX: Conversion into SI units for permeability, permeance and F/A (Feed Flow/Membrane Area).

Variable	Base unit	SI conversion
Permeability	1 Barrer	$3.35 \cdot 10^{-16}$ mol/(m·s·Pa)
Permeance	1 GPU	$3.35 \cdot 10^{-10}$ mol/(m^2·s·Pa)
F/A	1 m^3(STP)/(m^2 h)	0.012 mol/(m^2·s)

Appendix B: Membrane_UoE

In this Appendix the creation of a completely automated steady-state unit operation for Honeywell UniSim® Design is investigated. This integration has been carried out since the commercial software does not include a membrane unit operation and the customisation of the simulation environment represents an essential requisite for carrying out multi-stage membrane process designs.

The main steps in building the interface are analysed and the exstension is presented. This work is not only important for the membrane case, since the created interface offers the possibility to add new unit operations to the simulation environment.

1. UniSim® Design and its customisation

In Chapter 2 the modelling strategy was introduced: the codes are written in *C* linked to the SUNDIALS libraries [132] in order to solve the set of differential equations. The main idea of this integration is to keep the original code formulation and to link it to the process simulation environment. In order to do this, the key step is the creation of an interface between UniSim® and the code.

The typical strategy to customise UniSim® consists in a *Visual Basic* script which can be directly accessed using the tab menu in the simulator. A complete guide is available in the manual from Honeywell [152] which also includes examples of user-defined unit operations. *Visual Basic* can also be used to create an external project which should be built as a *Dynamic Link Library* (*.dll*) in order to be registered into UniSim®. The software libraries are included into the project and the user can obtain the desired parameters from the simulator and manipulate them.

The customisation process starts from the creation *.edf* file, which is the graphical interface in the simulation environment. It can be built by using both the *UniSim View Editor* and a text editor [152].

The two key points of this file are:

1. **Variables**: the main input/output variables and their type are defined in this interface. They can be either *user* variables (real, text, scalar, vectors…) or *attachments* which are containers of all the physical and chemical properties of the object they are related (usually streams).

2. **CLASS_ID**: the CLASS_ID is an alfa-numeric sequence which can be generated by the Windows GUIDGEN application. Each CLASS_ID corresponds to a particular *.dll* and *.edf* files.

The creation of the *.edf* file is the first step common to another way of writing the user defined unit operation which is the development of a *C++* code. This is the strategy chosen for the integration carried out in this PhD project: its main aim is the creation of an exstension similar to the unit operations available in the simulation environment. In the case of this study, the goal is to perform membrane single and multi-stage process simulations using the in-house models. General information on how to build a *C++* interface is reported in the *Customisation Guide* [152] and a *C++* exstension (a property calculator) was given by the UniSim® support. However, additional effort was required since the available example behaves like a controller, taking the value form the connected stream and showing the calculated properties in the interface. In the case of a general unit operation, the exstension requires both inlet and outlet connections and, consequently, a two-way communication between interface and simulator needs to be set up.

In the next paragraphs the main steps in the creation of the interface are presented: the attention will be focused on the innovative aspects compared to the traditional *Visual Basic* implementation.

2. *Membrane_UoE*

Membrane_UoE is the presented exstension unit operation: the original in-house membrane simulator is included into a *C++* interface with the UniSim® environment.

The project (its name is generalised as *Main*) consists in:

- *Header files:*
  - exstdk.hpp
  - ***Main.hpp***
- *Source files:*
  - ***Main.cpp***
  - unisimdesign.hh
  - unisimdesignid.c
  - exstdk.cpp
  - guids.cpp
  - ***Main.def***
  - *solver*.c

The original membrane C code is included as *solver.c* using the original *UserData* structure, which is a *typedef* structure where input and output parameters for the simulation are stored. Apart from the *Main* files, the other ones are included in the *Exstension Development Kit* into the UniSim® directory.

The procedure for the implementation is given for *Visual Studio* complier which is the one adopted. However, a common C++ open-source compiler (e.g. DevC++) can be used for building the *dll*.

2.1 Creation of the project

The first action required is the creation of the project: this procedure is valid independently of the unit operation.

The required steps are:

- Creating a new *WIN32 console application project*, selecting *dll* as application type.
- Adding the standard files from the exstension development kit.
- Adding the files to the project (header and source files). Before adding the *Main* files, their names are changed to the desired name for the exstension. All the files are added except for the *.def* one.
- In the window source files, a *.def* file is added and the following code is required in order to access the UniSim® libraries:

```
LIBRARY  "MAIN"

DESCRIPTION     'UniSim Design-MAIN sys DLL'

EXPORTS

       DllGetClassObject       @2  PRIVATE

       DllCanUnloadNow         @3  PRIVATE

       DllRegisterServer       @4  PRIVATE

       DllUnregisterServer     @5  PRIVATE
```

- In the *properties* tab (into *project window*) *Use Unicode Character Set* is changed to *Use Multicode Character*: this prevents building errors associated to the *exstdk* files.

The source code can now be modified by the user.

2.1.1 Main.hpp

Main.hpp is the header file where the main class of the program is defined, including variables and functions. Differently from the *Visual Basic* implementation which requires only the name of the exstension, the C++ interface requires the information of the CLASS_ID associated to the exstension.

The declaration section includes fixed parts (*OLE* interface) and the customization part consists in:

- **Variables**: all the variables defined into the *.edf* file are declared, in addition to the other persistent variables required for the calculation. It is not needed to define them in the program since they can be called and modified in every subroutine.

- **Functions**: apart from the standard functions (e.g. *getEDFvariables* to take the parameters from the edf file) the ones containing the calculations are added.

- **Errors**: the number and the names of the errors are defined. Their description and output messages are then added into the *Status Query* subroutine in the *main*.cpp file.

2.1.2 Main.cpp

This is the most important file for the exstension: it contains both user-defined and standard functions. The main structure includes:

- *Definition* of the main variables.
- *Inizialisation*: check of the connections and variables associated to them.

- *Execution*: connections and variables are checked and the *solver* function is called. A final check on the status of the streams is then performed before calling *solvecomplete ()* command which, if errors are not present, gives the Unit Operation the blu colour.
- *Status Query*: definition of the errors and associated messages.
- User-defined functions.
- Std *OLE* implementation: standard functions required for the interface.

Apart from the structure of the functions, particular attention should be focused on the communication between the code and the process streams.
First of all, *Variant* variables are used: this feature is directly derived from the *Visual Basic* environment. A *Variant* is a variable which stores data of varying types such as integers, floating point numbers, strings and arrays. Internally a *Variant* is an object that contains two member variables: one member stores information on data type and the second one stores the values. Each array containing numbers or text is converted and called as a *Variant* type. In order to manipulate the values inside the arrays, the *SafeArray* structure is also required: it is a class that encapsulates an array of any data type and provides certain protective features.
An important difference between *VB* and *C++* approach consists in the way the user can access to stream properties and in the following pages two significant examples which focus on stream properties are reported.

In Example 1 both *Variant* and *SafeArray* are used to retrieve the molar fractions from the feed stream which are then stored into an array included into the *CompData* structure (a typedef structure analogous to UserData).

Example 1:

```
if( Feed ) // Confirming the feed interface is ok
{
        VariantInit(&x);
        if(SUCCEEDED(Feed->get_ComponentMolarFractionValue(&x))) {
        // Ask for the composition mole fraction VARIANT
                if(V_VT(&x) == (VT_ARRAY|VT_R8))
        // Confirm it is the expect array of doubles
                sa = V_ARRAY(&x);
        // Extract the SafeArray
                if(sa && SUCCEEDED(SafeArrayGetUBound(sa,1,&count)) ) {
        // Get size of it
                if( (count+1) == WCompCount &&  SUCCEEDED(SafeArrayAccessData(sa,
                (void**)&vv))   )
                 {
        // Check  the expected size and get a C++ pointer to the data
                        long i;
        // if that was successful
                        for(i=0, cptr=WBasis; i<=count; i++)
                         {
        // For each component retrieve the mole fraction into the component data cache
                                cptr->molefrac = *vv;
                                vv++;     // Increment pointers
                                cptr++;
                        }
                        SafeArrayUnaccessData(sa);
                        // Done with C++ pointer now
                }
                else
                eflag = TRUE;     // Wrong no of components is a problem
        }
        else
         eflag = TRUE; // Not finding the no of components
        }
        else
        eflag = TRUE;     //  Not finding molefracs values
        }
else       // Feed not ok
eflag = TRUE;
```

The second example focuses on obtaining the feed flow rate with the desired unit, in this case *gmole/s*. This is an important feature in order to pass the variables with the appropriate unit to the solver function.

Example 2:

```
if( Feed ) {
if(SUCCEEDED(Feed->DuplicateFluid(&FeedFluid))){
// Get a copy of the feed stream`s fluid and get an interface of it:
        if(SUCCEEDED(FeedFluid->get_MolarFlow(&FluidMolFlow))) {
        FlowIsKnown = VARIANT_FALSE;
// Check the molar flow is known:
if(SUCCEEDED(FluidMolFlow->get_IsKnown(&FlowIsKnown)) && FlowIsKnown ==
VARIANT_TRUE)
                {
                        VariantInit(&Unitf);
                        V_VT(&Unitf) = VT_BSTR;
                        Unistrf = SysAllocString(OLESTR("gmole/s"));
                        V_BSTR(&Unitf) = Unistrf;
                        FluidMolFlow->GetValue(Unitf, &F_Mol);
                        // Get the feed molar flow rate:
                        Ff = F_Mol;
                }
                else //pressure data is missing
                Errors[WNOBASIS] = TRUE;
        }
        else // Could not get pressure
        eflag = TRUE;
        FeedFluid->Release();
        }
else // Could not duplicate fluid
eflag = TRUE;
}
else // Didn`t get feed stream
eflag = TRUE;
```

The approaches reported above are needed to obtain process parameters before passing their values to the main solver. As a general approach, a function containing the calculation can be written directly in *C++* after being defined in the *Main.hpp* file.

Errors and flags are an important part in building the interface since an appropriate hierarchy and organisation is essential for the stability of the interface. No external windows are opened during the simulation and, therefore, it is not possible to debug the *dll*. Errors are associated to both missing parameters and problems in the interaction with the main solver: customised messages can be shown into the command window of the software. In the case of flags, a change in their boolean

value (from *false* to *true*) blocks the resolution and gives the yellow color to the unit operation.

2.1.3 Link between SUNDIALS and the dll

The previously created interface needs to be linked to the SUNDIALS libraries. This represents a further and unique step in the customisation process compared to the standard customisation procedure [152].

First of all, the output commands (screen and file) are removed from the source code. In order to pass the parameters, the original typedef structure (*UserData*) can be maintained and called every time a parameter is needed by the program. Once the results are calculated, they are put into the *UserData* structure as well. The same typedef structure should be declared in the header file of the *C++* interface (they have the same structure in both *C* and *C++*).

In order to allow the communication between the *dll* and SUNDIALS libraries, *CMake* is used to build the complete interface, similarly to the procedure for the standard *C* models. In the *CMakelists.txt* file, all the header and source files previously reported are included and the project is consequently created. As a default, *CMake* builds an executable file and some extra actions are required compared to the base case. In addition to what reported in paragraph 2.1, the configuration type in the main project directory is changed to *.dll* and in the linker menu the exstension of the output file is changed to *.dll* as well.

Once the project is created, it includes both interface and membrane source code. In order to link the two levels, a function is added to the class: it passes the variables to the *UserData* structure and it calls the solver. If the procedure is successful and no errors are encountered (see the hierarchy of flags to identify errors in the examples), the customized function is called into *Main.cpp* and the problem is solved. The

results are ready to be put into the outlet streams and a similar procedure to *Example 1* is applied.

Particular attention should also be focused on the molar fraction case: a *SafeArray* is created, the calculated values are stored inside it and then passed to the stream properties. This was a trivial process in the creation of the interface due to the *SafeArray* structure and the procedure is reported and commented in *Example 3* for molar fractions.

Example 3

```
// The vector of the molar fractions is a variant
	VARIANT x
// The safearray is a vector
	SAFEARRAYBOUND aDim[1];
// Null initialisation
	SAFEARRAY* sa = NULL;
// Vector where the molar fractions are stored
	double *vv;
// Vector with Ncomponents elements
	aDim[0].lLbound = 0;
	aDim[0].cElements = WCompCount;
// The safearray is created
	sa = SafeArrayCreate(VT_R8, 1, aDim);
// The calculated molar fractions are transferred into the Safearray
	if(sa && SUCCEEDED(SafeArrayAccessData(sa,    (void**)&vv)))
	{
		long j;
		for(j=0; j<WCompCount; j++)
		{
			*vv = xr[j];
			vv++;
		}
	}
// Passed to the variant x
	x.parray = sa;
// The safearray is destroyed
	SafeArrayDestroy(sa);
// Eventually, they are passed to the retentate stream
	if (Retentate)
	{
		Retentate->put_ComponentMolarFractionValue(x);
	}
```

If the above procedures occur without encountering errors, the resolution is carried out. The *.edf* file is designed in the same way as the VB strategy: it should have the same name and defined CLASS_ID as the *dll*. *Dll* and *edf* files should be stored in the same folder of the pc: the source code is not required once the *dll* is built.

Once the program is built and connected to the SUNDIALS libraries, it can be registered into UniSim®. Consequently, it appears as a common unit operation available in the user menu.

3. Models implemented and software integration

Once the implementation of the interface was completed, it has been tested by different users. Apart from the presented work, *Membrane_UoE* has been tested by undergraduate, Masters' and PhD students. In particular, simulations for pre-combustion [153] and cement plant [154] carbon capture evaluations have been performed.

The versions of *Membrane_UoE* used in Chapter 4 are, respectively, non-dispersed plug-flow (1.0, counter-current flow pattern with sweep) and 2D cross-flow model (2.0).

The possibility of using input and output files has been added. By using this feature, input parameters can be set by simply modifying a *.txt* file in the same folder as the *dll*. Partial pressure profiles can be obtained from the simulation as output files and the behaviour of the separation in the stages can be plotted.

With the aim of integrating the more detailed models into the software, interfaces including pressure drops have been designed to simulate hollow-fibre (3.0) and spiral-wound (4.0) modules. In order to facilitate the approach to the simulation, the first run can be done using input parameters from an input file: the user can de-select this option and carry out simulations with the desired variables.

4. Conclusion

In this Appendix the key points of the procedure in the creation of *Membrane_UoE* have been shown. It is important to point out that, thanks to the developed interface, the simulation environment can be customised with new unit operations.

However, there are aspects that need further investigation. In Chapter 3 simulations have been shown in both ideal and non-ideal behaviour identifying no effects on the performances due to the low pressure for carbon capture applications. However, non-ideality might play an important contribution in the case of high-pressure separations, typical for commercial membrane applications. Despite it is not possible at the moment to implement a customised fluid package, it might be included into the unit operation. This is a feasible option and its implementation starts from a creation of a database of constants (e.g. critical properties) which should be added to the main project. The properties should be inserted associated to the component *IDnumber*, which is the way UniSim® recognises the different species according to the classification ISO 6076. A similar procedure to what shown for molar fraction should be followed to retrieve the *IDnumber* of each component: the constants can be organised into appropriate arrays which can be stored into the *UserData* structure and called by the main solver.

The possibility of implementing dynamic unit operations is also an important point of discussion. The main challenge of this approach in both languages (VB and C++) is the creation of an interface between the customised code and the solver used by the dynamic simulator. An interface with the *Integrator* (the name of the dynamic solver) should be created and the simulation *time* of the solver should be passed to the exstension at each time step. This implementation has already been carried out in Visual Basic [155, 156]. The challenge of integrating *Membrane_UoE* would be the link between the two solvers and the modification of the steady state interface. This last aspect appears to be the most trivial since a complete and stable communication between SUNDIALS and the *Integrator* should be enabled.

Appendix C: Multi-stage designs

The schematic diagram of the Retrofit case with 95 % final purity is presented in Figure VIII. Since the flue gas is already at a pressure of 117 kPa, the first compression stage (C1) is not required. C1 is in this case a blower. However, it is kept in the design to demonstrate the general process scheme and allow for flexibility on the design as well as on the relevant assumptions. The main material streams are reported in Table X - Table XI and the energy streams are reported in Table XII.

The Hybrid case is reported in Figure IX. The stream properties are reported in Table XIII - Table XIV and energy streams/membrane area are shown in Table XV. Heat exchangers H10, H11 and H12 are reported as representative since these streams are used for heat integration before the refrigeration stage. Therefore, the energy requirement for refrigeration already takes this integration into account.

The Selective Exhaust Gas Recycling design is reported in Figure X. The stream properties are reported in Table XVI - Table XVII and energy streams/membrane area are reported in Table XVIII. The same consideration for heat exchangers H10, H11and H12 in the hybrid design applies here.

For all the designs, the energy consumption for the capture process is calculated with respect to the compression requirement (and refrigeration for hybrid and selective exhaust recycling cases) in line with the available literature [39, 45].

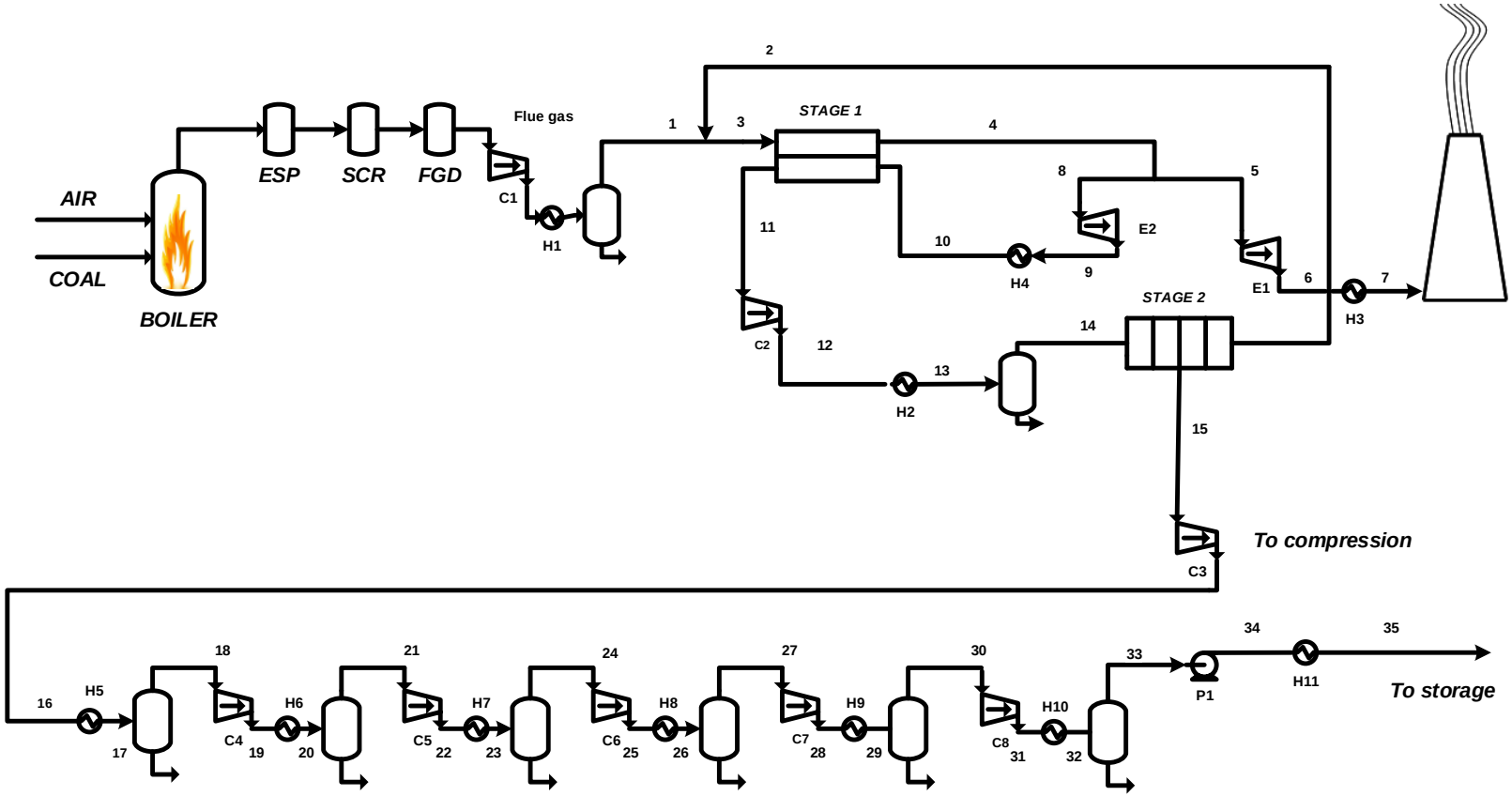

Figure VIII: Retrofit design.

Table X: Stream properties for the Retrofit design reported in Figure VIII – Part 1.

Stream	**Flue gas**	**1**	**2**	**3**	**4**	**5**	**6**	**7**	**8**	**9**	**10**	**11**	**12**	**13**
Flow [mol/s]	2.02E+04	1.87E+04	8.81E+03	2.75E+04	1.91E+04	1.56E+04	1.56E+04	1.56E+04	3.50E+03	3.50E+03	3.50E+03	1.19E+04	1.19E+04	1.19E+04
T [K]	330.4	298.2	298.2	298.2	298.2	298.2	292.0	330.4	298.2	286.8	298.2	298.2	470.0	298.2
P [MPa]	0.117	0.117	0.117	0.117	0.117	0.117	0.110	0.110	0.117	0.100	0.100	0.022	0.117	0.117
O_2	2.08%	2.2%	2.9%	2.4%	2.6%	2.6%	2.6%	2.6%	2.6%	2.6%	2.6%	2.2%	2.2%	2.2%
N_2	73.67%	79.4%	58.8%	72.8%	95.2%	95.2%	95.2%	95.2%	95.2%	95.2%	95.2%	43.8%	43.8%	43.8%
H_2O	9.49%	2.5%	1.8%	2.3%	0.2%	0.2%	0.2%	0.2%	0.2%	0.2%	0.2%	4.9%	4.9%	4.9%
CO_2	14.76%	15.9%	36.5%	22.5%	2.0%	2.0%	2.0%	2.0%	2.0%	2.0%	2.0%	49.0%	49.0%	49.0%
Total	100.0%	100.0%	100.0%	100.0%	100.0%	100.0%	100.0%	100.0%	100.0%	100.0%	100.0%	100.0%	100.0%	100.0%
Stream	**14**	**15**	**16**	**17**	**18**	**19**	**20**	**21**	**22**	**23**	**24**	**25**	**26**	**27**
Flow [mol/s]	1.16E+04	2.93E+03	2.93E+03	2.93E+03	2.88E+03	2.88E+03	2.88E+03	2.88E+03	2.88E+03	2.88E+03	2.85E+03	2.85E+03	2.85E+03	2.82E+03
T [K]	298.1	298.1	439.1	298.1	298.1	373.8	318.1	318.1	396.2	318.1	318.1	397.4	318.1	318.1
P [Pa]	0.11	0.02	0.10	0.10	0.10	0.24	0.24	0.24	0.56	0.56	0.56	1.32	1.32	1.32
O_2	2.3%	0.6%	0.6%	0.6%	0.6%	0.6%	0.6%	0.6%	0.6%	0.6%	0.6%	0.6%	0.6%	0.6%
N_2	44.9%	3.6%	3.6%	3.6%	3.7%	3.7%	3.7%	3.7%	3.7%	3.7%	3.7%	3.7%	3.7%	3.8%
H_2O	2.5%	4.5%	4.5%	4.5%	2.7%	2.7%	2.7%	2.7%	2.7%	2.7%	1.6%	1.6%	1.6%	0.8%
CO_2	50.3%	91.3%	91.3%	91.3%	93.0%	93.0%	93.0%	93.0%	93.0%	93.0%	94.0%	94.0%	94.0%	94.8%
Total	100.0%	100.0%	100.0%	100.0%	100.0%	100.0%	100.0%	100.0%	100.0%	100.0%	100.0%	100.0%	100.0%	100.0%

Table XI: Stream properties for the Retrofit design reported in Figure VIII – Part 2.

Stream	28	29	30	31	32	33	34	35
Flow [mol/s]	2.82E+03	2.82E+03	2.81E+03	2.81E+03	2.81E+03	2.81E+03	2.81E+03	2.81E+03
T [K]	398.3	318.1	318.1	318.1	396.5	288.1	299.7	298.1
P [Pa]	3.120	3.120	3.120	3.120	7.380	7.380	15.000	15.000
O_2	0.6%	0.6%	0.6%	0.6%	0.6%	0.6%	0.6%	0.6%
N_2	3.8%	3.8%	3.8%	3.8%	3.8%	3.8%	3.8%	3.8%
H_2O	0.8%	0.8%	0.8%	0.4%	0.4%	0.4%	0.4%	0.4%
CO_2	94.8%	94.8%	94.8%	95.2%	95.2%	95.2%	95.2%	95.2%
Total	100.0%	100.0%	100.0%	100.0%	100.0%	100.0%	100.0%	100.0%

Table XII: Energy consumption for heat exchangers and compression equipment and membrane area for the Retrofit design reported in Figure VIII.

Heat Exchanger Equipment	Energy Consumption [kWth]	Compressors/ Expanders and Vacuum pumps	Energy Consumption [kWe]	Membrane stages	Area [m^2]
H1	83980	**E1**	-1685	**Area 1**	290000
H2	85810	**E2**	-582	**Area 2**	15000
H3	19070	**P1**	1566	**Total**	**305000**
H4	1152	**C1**	0		
H5	18860	**C2**	70286 (= 61927 + 8360)*		
H6	6346	**C3**	15879		
H7	10420	**C4**	8162		
H8	10520	**C5**	8496		
H9	10810	**C6**	8409		
H10	37750	**C7**	8117		
H11	149	**C8**	7056		
		TOTAL	**125704**		

*The values in parentheses indicate energy consumption of the vacuum pump + energy consumption of the blower.

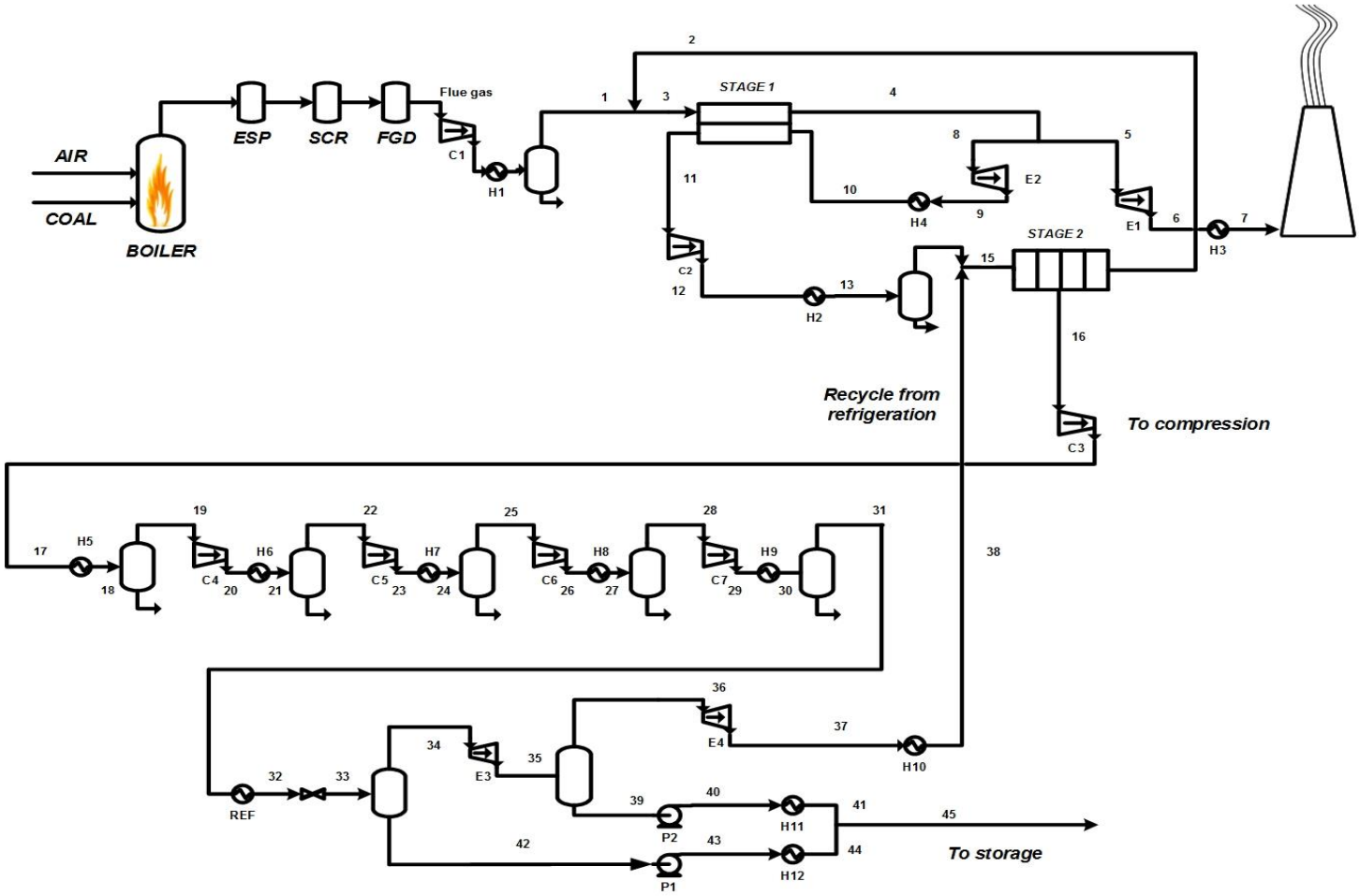

Figure IX: Hybrid design.

Table XIII: Stream properties for the Hybrid design reported in Figure IX – Part 1.

Stream	**Flue gas**	**1**	**2**	**3**	**4**	**5**	**6**	**7**	**8**	**9**	**10**	**11**	**12**	**13**
Flow [mol/s]	2.02E+04	1.87E+04	7.85E+03	2.65E+04	1.91E+04	1.91E+04	1.91E+04	1.56E+04	3.50E+03	3.50E+03	3.50E+03	1.10E+04	1.10E+04	1.10E+04
T [K]	330.4	298.1	298.1	298.1	298.1	298.1	294.7	330.1	298.1	292.2	298.1	298.1	473.8	298.1
P [MPa]	0.117	0.117	0.117	0.117	0.117	0.117	0.110	0.110	0.117	0.100	0.100	0.022	0.110	0.110
O_2	2.1%	2.2%	3.4%	2.6%	2.7%	2.7%	2.7%	2.7%	2.7%	2.7%	2.7%	2.5%	2.5%	2.5%
N_2	73.7%	79.5%	66.8%	75.8%	95.4%	95.4%	95.4%	95.4%	95.4%	95.4%	95.4%	48.1%	48.1%	48.1%
H_2O	9.5%	2.3%	1.4%	2.0%	0.2%	0.2%	0.2%	0.2%	0.2%	0.2%	0.2%	4.6%	4.6%	4.6%
CO_2	14.8%	15.9%	28.3%	19.6%	1.7%	1.7%	1.7%	1.7%	1.7%	1.7%	1.7%	44.7%	44.7%	44.7%
Total	100.0%	100.0%	100.0%	100.0%	100.0%	100.0%	100.0%	100.0%	100.0%	100.0%	100.0%	100.0%	100.0%	100.0%
Stream	**14**	**15**	**16**	**17**	**18**	**19**	**20**	**21**	**22**	**23**	**24**	**25**	**26**	**27**
Flow [mol/s]	1.07E+04	1.14E+04	3.48E+03	3.48E+03	3.48E+03	3.48E+03	3.42E+03	3.42E+03	3.42E+03	3.42E+03	3.42E+03	3.38E+03	3.38E+03	3.38E+03
T [K]	298.1	298.1	298.1	373.6	298.1	298.1	374.3	318.1	318.1	396.8	318.1	318.1	398.3	318.1
P [Pa]	0.12	0.12	0.02	0.10	0.10	0.10	0.24	0.24	0.24	0.56	0.56	0.56	1.32	1.32
O_2	2.6%	2.6%	0.9%	0.9%	0.9%	0.9%	0.9%	0.9%	0.9%	0.9%	0.9%	0.9%	0.9%	0.9%
N_2	49.2%	47.7%	5.0%	5.0%	5.0%	5.0%	5.1%	5.1%	5.1%	5.1%	5.1%	5.1%	5.1%	5.1%
H_2O	2.5%	2.3%	4.4%	4.4%	4.4%	4.4%	2.7%	2.7%	2.7%	2.7%	2.7%	1.6%	1.6%	1.6%
CO_2	45.7%	47.3%	89.7%	89.7%	89.7%	89.7%	91.4%	91.4%	91.4%	91.4%	91.4%	92.4%	92.4%	92.4%
Total	100.0%	100.0%	100.0%	100.0%	100.0%	100.0%	100.0%	100.0%	100.0%	100.0%	100.0%	100.0%	100.0%	100.0%

Table XIV: Stream properties for the hybrid design reported in Figure IX – Part 2.

Stream	**28**	**29**	**30**	**31**	**32**	**33**	**34**	**35**	**36**	**37**	**38**	**39**	**40**	**41**
Flow [mol/s]	3.35E+03	3.35E+03	3.35E+03	3.35E+03	3.35E+03	3.35E+03	6.80E+02	6.80E+02	6.47E+02	6.47E+02	6.47E+02	3.26E+01	3.26E+01	3.26E+01
T [K]	318.1	399.8	323.1	323.1	253.1	243.6	243.6	224.8	224.8	195.9	298.1	224.8	231.6	298.1
P [MPa]	1.320	3.120	3.120	3.120	3.120	2.000	2.000	1.000	1.000	0.117	0.117	1.000	15.000	15.000
O_2	0.9%	0.9%	0.9%	0.9%	0.9%	0.9%	3.6%	3.6%	3.8%	3.8%	3.8%	0.1%	0.1%	0.1%
N_2	5.2%	5.2%	5.2%	5.2%	5.2%	5.2%	22.1%	22.1%	23.2%	23.2%	23.2%	0.4%	0.4%	0.4%
H_2O	0.8%	0.8%	0.8%	0.8%	0.8%	0.8%	0.0%	0.0%	0.0%	0.0%	0.0%	0.0%	0.0%	0.0%
CO_2	93.2%	93.2%	93.2%	93.2%	93.2%	93.2%	74.2%	74.2%	73.0%	73.0%	73.0%	99.5%	99.5%	99.5%
Total	100.0%	100.0%	100.0%	100.0%	100.0%	100.0%	100.0%	100.0%	100.0%	100.0%	100.0%	100.0%	100.0%	100.0%

Stream	**42**	**43**	**44**	**45**
Flow [mol/s]	2.67E+03	2.67E+03	2.67E+03	2.71E+03
T [K]	243.6	251.5	298.1	298.1
P [MPa]	2.000	15.000	15.000	15.000
O_2	0.2%	0.2%	0.2%	0.2%
N_2	0.9%	0.9%	0.9%	0.9%
H_2O	1.0%	1.0%	1.0%	0.9%
CO_2	98.0%	98.0%	98.0%	98.0%
Total	100.0%	100.0%	100.0%	100.0%

Table XV: Energy consumption for heat exchangers and compression equipment and membrane area for the design reported in Figure IX.

Heat Exchanger Equipment	Energy Consumption [kWth]	Compressors/ Expanders and Vacuum pumps	Energy Consumption [kWe]	Membrane stages	Area [m^2]
H1	88050	**Refrigeration**	14367	**Area 1**	280000
H2	78240	**E1**	-1735	**Area 2**	20000
H3	16200	**E2**	-640	**Total**	**300000**
H4	-596	**E3**	-609		
H5	7560	**E4**	-2082		
H6	12430	**P1**	1740		
H7	12510	**P2**	22		
H8	11860	**C1**	0		
H9	22450	**C2**	65552 (=57749 + 7803)*		
H10	-2298	**C3**	19090		
H11	-200	**C4**	9791		
H12	-12010	**C5**	10182		
		C6	10065		
		C7	9679		
		TOTAL	**135423**		

*The values in parentheses indicate energy consumption of the vacuum pump + energy consumption of the blower.

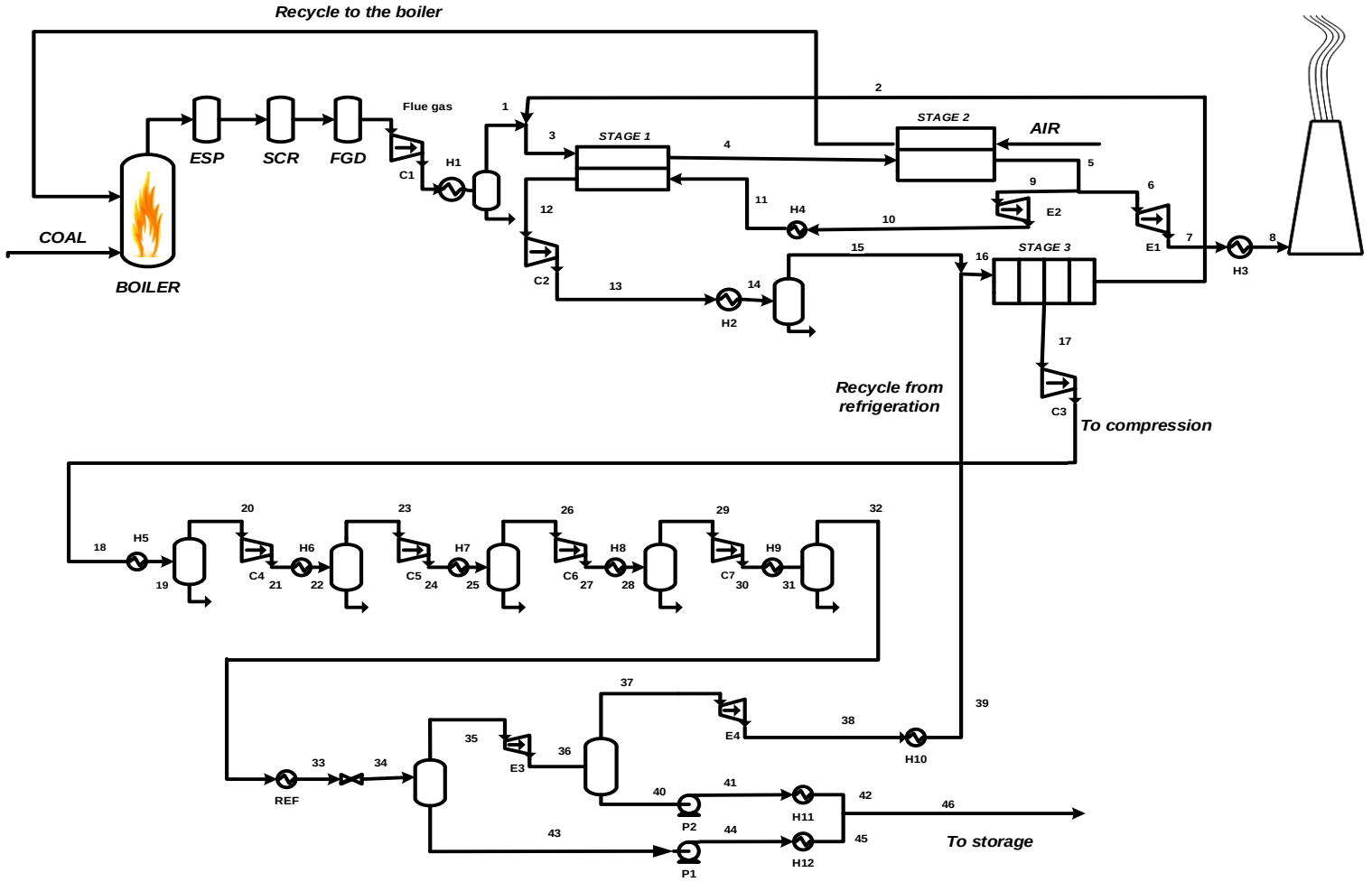

Figure X: Selective exhaust gas recycling design.

Table XVI: Stream properties for the selective exhaust gas recycling design reported in Figure X – Part 1.

Stream	**Flue gas**	**1**	**2**	**3**	**4**	**5**	**6**	**7**	**8**	**9**	**10**	11	**12**	**13**
Flow [mol/s]	2.03E+04	1.90E+04	6.27E+03	2.52E+04	1.95E+04	1.93E+04	1.93E+04	1.93E+04	1.93E+04	3.50E+03	3.50E+03	3.50E+03	9.28E+03	9.28E+03
T [K]	330.4	298.1	298.1	298.1	298.1	298.1	298.1	294.0	330.1	294.0	288.5	298.1	298.1	479.7
P [MPa]	0.117	0.117	0.117	0.117	0.117	0.117	0.117	0.110	0.110	0.117	0.100	0.100	0.022	0.100
O_2	0.7%	0.8%	2.3%	1.1%	1.3%	3.0%	3.0%	3.0%	3.0%	3.0%	3.0%	3.0%	1.6%	1.6%
N_2	73.5%	78.6%	68.9%	76.2%	93.8%	94.3%	94.3%	94.3%	94.3%	94.3%	94.3%	94.3%	46.6%	46.6%
H_2O	8.7%	2.3%	1.2%	2.0%	0.5%	0.8%	0.8%	0.8%	0.8%	0.8%	0.8%	0.8%	4.8%	4.8%
CO_2	17.1%	18.3%	27.5%	20.6%	4.4%	1.9%	1.9%	1.9%	1.9%	1.9%	1.9%	1.9%	47.1%	47.1%
Total	100.0%	100.0%	100.0%	100.0%	100.0%	100.0%	100.0%	100.0%	100.0%	100.0%	100.0%	100.0%	100.0%	100.0%
Stream	**14**	**15**	**16**	**17**	**18**	**19**	**20**	**21**	**22**	**23**	**24**	**25**	**26**	**27**
Flow [mol/s]	9.28E+03	9.04E+03	9.59E+03	3.34E+03	3.34E+03	3.34E+03	3.34E+03	3.34E+03	3.34E+03	3.29E+03	3.29E+03	3.29E+03	3.26E+03	3.26E+03
T [K]	298.1	298.1	298.1	298.1	298.1	439.7	298.1	298.1	374.2	318.1	396.6	318.1	318.1	398.1
P [MPa]	0.117	0.117	0.117	0.022	0.100	0.100	0.100	0.240	0.240	0.240	0.560	0.560	0.560	1.320
O_2	1.6%	1.6%	1.7%	0.5%	0.5%	0.5%	0.5%	0.5%	0.5%	0.5%	0.5%	0.5%	0.5%	0.5%
N_2	46.6%	47.8%	46.4%	4.6%	4.6%	4.6%	4.7%	4.7%	4.7%	4.7%	4.7%	4.7%	4.8%	4.8%
H_2O	4.8%	2.3%	2.2%	4.0%	4.0%	4.0%	2.7%	2.7%	2.7%	2.7%	2.7%	2.7%	1.6%	1.6%
CO_2	47.1%	48.3%	49.8%	90.8%	90.8%	90.8%	92.1%	92.1%	92.1%	92.1%	92.1%	92.1%	93.1%	93.1%
Total	100.0%	100.0%	100.0%	100.0%	100.0%	100.0%	100.0%	100.0%	100.0%	100.0%	100.0%	100.0%	100.0%	100.0%

Table XVII: Stream properties for the selective exhaust gas recycling design reported in Figure X – Part 2.

Stream	**28**	**29**	**30**	**31**	**32**	**33**	**34**	**35**	**36**	**37**	**38**	**39**	**40**	**41**
Flow [mol/s]	3.26E+03	3.23E+03	3.23E+03	3.23E+03	3.23E+03	3.23E+03	3.23E+03	5.79E+02	5.79E+02	5.51E+02	5.51E+02	5.51E+02	2.78E+01	2.78E+01
T [K]	318.1	318.1	398.1	318.1	398.1	253.1	244.1	244.1	225.2	225.2	196.0	298.1	225.2	232.0
P [MPa]	1.320	1.320	1.320	3.120	3.120	3.120	2.000	2.000	1.000	1.000	0.117	0.117	1.000	15.000
O_2	0.5%	0.5%	0.5%	0.5%	0.5%	0.5%	0.5%	2.4%	2.4%	2.5%	2.5%	2.5%	0.1%	0.1%
N_2	4.8%	4.8%	4.8%	4.8%	4.8%	4.8%	4.8%	22.7%	22.7%	23.8%	23.8%	23.8%	0.4%	0.4%
H_2O	1.6%	0.8%	0.8%	0.8%	0.8%	0.8%	0.8%	0.0%	0.0%	0.0%	0.0%	0.0%	0.0%	0.0%
CO_2	93.1%	93.9%	93.9%	93.9%	93.9%	93.9%	93.9%	74.9%	74.9%	73.7%	73.7%	73.7%	99.5%	99.5%
Total	100.0%	100.0%	100.0%	100.0%	100.0%	100.0%	100.0%	100.0%	100.0%	100.0%	100.0%	100.0%	100.0%	100.0%

Stream	**42**	**43**	**44**	**45**	**46**	**Air**	**Recycle to the boiler**
Flow [mol/s]	2.78E+01	2.65E+03	2.65E+03	2.65E+03	2.68E+03	1.86E+04	1.88E+04
T [K]	298.1	244.1	252.0	298.1	298.1	298.0	298.0
P [MPa]	1.000	2.000	15.000	15.000	15.000	0.172	0.117
O_2	0.1%	0.1%	0.1%	0.1%	0.1%	20.9%	18.93%
N_2	0.4%	0.9%	0.9%	0.9%	0.9%	79.1%	77.68%
H_2O	0.0%	0.9%	0.9%	0.9%	0.9%	0.0%	0.70%
CO_2	99.5%	98.0%	98.0%	98.0%	98.1%	0.0%	2.69%
Total	100.0%	100.0%	100.0%	100.0%	100.0%	100.0%	100.0%

Table XVIII: Energy consumption for heat exchangers and compression equipment and membrane area for the design reported in Figure X.

Heat Exchanger Equipment	Energy Consumption [kWth]	Compressors/ Expanders and Vacuum pumps	Energy Consumption [kWe]	Membrane stages	Area [m^2]
H1	81320	**Refrigeration**	14220	**Area 1**	140000
H2	70030	**E1**	-1793	**Area 2**	60000
H3	16665	**E2**	-960	**Area 3**	30000
H4	-996	**E3**	-514	**Total**	**230000**
H5	20840	**E4**	-1755		
H6	7275	**P1**	1709		
H7	11970	**P2**	18		
H8	12050	**C1**	0		
H9	11430	**C2**	57434 (= 50606 + 6827)*		
H10	-1959	**C3**	18110		
H11	-170	**C4**	9330		
H12	-12000	**C5**	9700		
		C6	9586		
		C7	9218		
		TOTAL	**124303**		

*The values in parentheses indicate energy consumption of the vacuum pump + energy consumption of the blower.

Appendix D: Conference presentations and publications

Conference presentations

- Greenhouse Gas Control Technologies (GHGT) Conference, 18th-22nd November 2012, Kyoto (Japan)
    - Bocciardo, Ferrari and Brandani. "Modelling and multi-stage design of membrane processes applied to carbon capture in coal-fired power plants", Poster presentation

- Euromembrane 2012, 23rd-27th September 2012, London (UK)
    - Bocciardo, Ferrari and Brandani. "Membrane Processes Applied to Carbon Capture in Coal-Fired Power Plants: From Modelling to Multi-Stage Design", Poster presentation
    - Kapetaki, Bocciardo, Ferrari, Ahn and Brandani. "Performance of Hybrid Membrane – Solvent Configurations for Pre – Combustion Carbon Capture in IGCC Power Plants", Poster presentation

- 2012 AIChE Annual Meeting, 28th October – 2nd November 2012, Pittsburgh (US)
    - Bocciardo, Ferrari and Brandani. "Membrane Processes applied to Carbon Capture in Coal-Fired Power Plants: Multi-Stage Design and Economic Analysis", Oral presentation

- Honeywell Users Group 2012 Conference for Europe, Middle-East and Africa, 11th-14th November 2012, Istanbul (Turkey)
    - Bocciardo, Ferrari and Brandani. "Customising UniSim Design: membrane separation and its application to carbon capture". Winning entry of the 2012 UniSim Design Challenge for EMEA, Oral presentation and award.

- 2nd Membrane Separation Processes Symposium (SIMPAM), 29th July – 2nd August 2013, Rio de Janeiro (Brazil)
    - Bocciardo, Ferrari and Brandani. "1D and 2D Approaches for Modelling Hollow-fibre and Spiral-wound Permeators For Gas Separation", Poster presentation
    - Bocciardo, Ferrari and Brandani. "Multi-stage Design for Carbon Capture from Coal-fired Power Plants: From Process Design to Economic Analysis", Oral presentation

- 2013 AIChE Annual Meeting, 3rd-8th November, San Francisco (US)
    - Ozcan, Bocciardo, Ferrari, Ahn, Kierzkowska, Müller and Brandani. "Comparison of Various Carbon Capture Technologies to Reduce CO_2 Emissions From a Cement Plant", Oral presentation

Publications

- Bocciardo, Ferrari and Brandani (2013). "Modelling and multi-stage design of membrane processes applied to carbon capture in coal-fired power plants." Energy Procedia 37: 932-940.

References

1. IPCC, *Renewable Energy Sources and Climate Change Mitigation - Special Report of the Intergovernmental Panel on Climate Change*. 2012.
2. IPCC, *Managing the risks of extreme events and disasters to advance climate change adaptation*. 2011, Cambridge University Press.

3. IPCC, *CLIMATE CHANGE 2013: THE PHYSICAL SCIENCE BASIS*. 2013.
4. IEA, *Energy Technology Transitions for Industry: Strategies for the Next Industrial Revolution*. 2009, International Energy Agency: Paris.
5. Kuramochi T., Ramírez A., Turkenburg W., and Faaij A., *Comparative assessment of CO_2 capture technologies for carbon-intensive industrial processes.* Progress in Energy and Combustion Science, 2012. **38**(1): p. 87-112.
6. *UK Department of Energy & Climate Change (DECC)*. Access date: 12/2013; Available from: https://www.gov.uk/government/organisations/department-of-energy-climate-change.
7. Luis P., Van Gerven T., and Van der Bruggen B., *Recent developments in membrane-based technologies for CO_2 capture.* Progress in Energy and Combustion Science, 2012. **38**(3): p. 419-448.
8. Hammond G.P., Akwe S.S.O., and Williams S., *Techno-economic appraisal of fossil-fuelled power generation systems with carbon dioxide capture and storage.* Energy, 2011. **36**(2): p. 975-984.
9. IEA, *World Energy Outlook 2012*. 2012.
10. Aden N., Fridley D., and Zheng N., *China's Coal: Demand, Constraints and Externalities*. 2009.
11. Gibbins J. and Chalmers H., *Carbon capture and storage.* Energy Policy, 2008. **36**(12): p. 4317-4322.
12. Herzog H. and Eide J., *Rethinking CCS - Moving Forward in Times of Uncertainty.* The Official jJournal of the World Coal Association, 2013.
13. IEA, *Energy Technologies Perspectives*. 2008.
14. Figueroa J.D., Fout T., Plasynski S., McIlvried H., and Srivastava R.D., *Advances in CO_2 capture technology—The U.S. Department of Energy's Carbon Sequestration Program.* International Journal of Greenhouse Gas Control, 2008. **2**(1): p. 9-20.
15. Kapetaki Z., Ahn H., and Brandani S., *Detailed Process Simulation of Pre-combustion IGCC Plants Using Coal-slurry and Dry Coal Gasifiers.* Energy Procedia, 2013. **37**: p. 2196-2203.
16. Boot-Handford M.E., Abanades J.C., Anthony E.J., Blunt M.J., Brandani S., Mac Dowell N., Fernández J.R., Ferrari M.C., Gross R., Hallett J.P., Haszeldine R.S., Heptonstall P., Lyngfelt A., Makuch Z., Mangano E., Porter R.T.J., Pourkashanian M., Rochelle G.T., Shah N., Yao J.G., and Fennell P.S., *Carbon capture and storage update.* Energy & Environmental Science, 2013.
17. IPCC, *IPCC Special Report on Carbon Dioxide Capture and Storage*. 2005.
18. Favre E., *Carbon dioxide recovery from post-combustion processes: Can gas permeation membranes compete with absorption?* Journal of Membrane Science, 2007. **294**(1-2): p. 50-59.
19. Bounaceur R., Lape N., Roizard D., Vallieres C., and Favre E., *Membrane processes for post-combustion carbon dioxide capture: A parametric study.* Energy, 2006. **31**(14): p. 2556-2570.

20. Ahn H., Luberti M., Liu Z., and Brandani S., *Process configuration studies of the amine capture process for coal-fired power plants.* International Journal of Greenhouse Gas Control, 2013. **16**: p. 29-40.
21. NETL, *Advanced Carbon Dioxide Capture R&D Program: Technology Update. Appendix B: Carbon Dioxide Capture Technology Sheets - Post-Combustion Solvents.* 2013.
22. Rubin E.S., Mantripragada H., Marks A., Versteeg P., and Kitchin J., *The outlook for improved carbon capture technology.* Progress in Energy and Combustion Science, 2012. **38**(5): p. 630-671.
23. Zhao L., Riensche E., Menzer R., Blum L., and Stolten D., *A parametric study of CO_2/N_2 gas separation membrane processes for post-combustion capture.* Journal of Membrane Science, 2008. **325**(1): p. 284-294.
24. NETL, *Cost and Performance Baseline for Fossil Energy Plants*. 2007, US Department Of Energy.
25. Bocciardo D., Ferrari M.C., and Brandani S., *Customising UniSim Design: membrane separation and its application to carbon capture*, in *EMEA HUG 2012 (Honeywell Users' Group conference for Europe, Middle-East and Africa)*. 2012: Istanbul.
26. Baker R., *Membrane technology and applications*. 3rd ed. 2012: John Wiley & Sons, Ltd.
27. Baker R., *Future Directions of Membrane Gas Separation Technology.* Industrial & Engineering Chemistry Research, 2002. **41**: p. 1393-1411.
28. Scholes C.A., Stevens G.W., and Kentish S.E., *Membrane gas separation applications in natural gas processing.* Fuel, 2012. **96**: p. 15-28.
29. Drioli E. and Barbieri G., *Membrane Engineering for the Treatment of Gases*. 1st ed. 2011: RCS Publishing.
30. *Cooperative Research Centre for Greenhouse Gases Technologies*. Access date: 12/2013; Available from: http://www.co2crc.com.au.
31. Agrawal R., *A simplified method for the synthesis of gas separation membrane cascades with limited numbers of compressors.* Chemical Engineering Science, 1996. **52**: p. 1029-1044.
32. Agrawal R., *Membrane Cascade Schemes for Multicomponent Gas Separation.* Industrial & Engineering Chemistry Research, 1996. **35**: p. 3607-3617.
33. Agrawal R. and Jiango X., *Gas-Separation Membrane Cascades Utilizing Limited Number of Compressors.* AIChE Journal, 1996. **42**(8): p. 2141-2154.
34. Follmann P.M., Bayer C., Wessling M., and Melin T., *Membrane Gas Separation Processes for CO_2 Capture from Coal fired Power Plants*, in *ICOM 2011*. Amsterdam.
35. *decarboni.se Solutions To Climate Change*. Access date: 01/2014; Available from: http://decarboni.se/publications/strategic-analysis-global-status-carbon-capture-storage-report-2/2-post-combustion.
36. Hasan M.M.F., Baliban R.C., Elia J.A., and Floudas C.A., *Modeling, Simulation, and Optimization of Postcombustion CO_2 Capture for Variable Feed Concentration and Flow Rate. 1. Chemical Absorption and Membrane*

Processes. Industrial & Engineering Chemistry Research, 2012. **51**(48): p. 15642-15664.
37. Favre E., *Membrane processes and postcombustion carbon dioxide capture: Challenges and prospects.* Chemical Engineering Journal, 2011. **171**(3): p. 782-793.
38. Ho M.T., Allinson G., and Wiley D.E., *Reducing the Cost of CO_2 Capture from Flue Gases Using Membrane Technology.* Industrial & Engineering Chemistry Research, 2008. **47**: p. 1562-1568.
39. Merkel T.C., Lin H., Wei X., and Baker R., *Power plant post-combustion carbon dioxide capture: An opportunity for membranes.* Journal of Membrane Science, 2010. **359**(1-2): p. 126-139.
40. Ramasubramanian K. and Ho W.S.W., *Recent developments on membranes for post-combustion carbon capture.* Current Opinion in Chemical Engineering, 2011. **1**(1): p. 47-54.
41. Shao P., Dal-Cin M.M., Guiver M.D., and Kumar A., *Simulation of membrane-based CO_2 capture in a coal-fired power plant.* Journal of Membrane Science, 2013. **427**: p. 451-459.
42. Vallieres C., *Vacuum versus sweeping gas operation for binary mixtures separation by dense membrane processes.* Journal of Membrane Science, 2004. **244**(1-2): p. 17-23.
43. Zhai H. and Rubin E.S., *Techno-Economic Assessment of Polymer Membrane Systems for Postcombustion Carbon Capture at Coal-Fired Power Plants.* Environmental Science & Technology, 2013. **47**(6): p. 3006-3014.
44. Zhang X., He X., and Gundersen T., *Post-combustion Carbon Capture with a Gas Separation Membrane: Parametric Study, Capture Cost, and Exergy Analysis.* Energy & Fuels, 2013: p. 130308131947001.
45. Zhao L., Riensche E., Blum L., and Stolten D., *Multi-stage gas separation membrane processes used in post-combustion capture: Energetic and economic analyses.* Journal of Membrane Science, 2010. **359**(1-2): p. 160-172.
46. Brunetti A., Scura F., Barbieri G., and Drioli E., *Membrane technologies for CO_2 separation.* Journal of Membrane Science, 2010. **359**(1-2): p. 115-125.
47. Bernardo P., Drioli E., and Golemme G., *Membrane Gas Separation: A Review/State of the Art.* Industrial & Engineering Chemistry Research, 2009. **48**: p. 4638-4663.
48. Low B.T., Zhao L., Merkel T.C., Weber M., and Stolten D., *A parametric study of the impact of membrane materials and process operating conditions on carbon capture from humidified flue gas.* Journal of Membrane Science, 2013. **431**: p. 139-155.
49. NETL, *Advanced Carbon Dioxide Capture R&D Program: Technology Update. Appendix B: Carbon Dioxide Capture Technology Sheets - Post-Combustion Membranes.* 2013.
50. Robeson L.M., *Correlation of separation factor versus permeability for polymeric membranes.* Journal of Membrane Science, 1991. **62**: p. 165-185.
51. Robeson L.M., *The upper bound revisited.* Journal of Membrane Science, 2008. **320**(1-2): p. 390-400.

52. Budd P., McKeown N., Ghanem B., Msayib K., Fritsch D., Starannikova L., Belov N., Sanfirova O., Yampolskii Y., and Shantarovich V., *Gas permeation parameters and other physicochemical properties of a polymer of intrinsic microporosity: Polybenzodioxane PIM-1.* Journal of Membrane Science, 2008. **325**(2): p. 851-860.
53. Amo K., He Z., Kaschemekat J., Merkel T., Pande S., Wei X., White S., Seshadri P., and Farzan H., *Pilot Testing of a Membrane System for Post-Combustion CO_2 Capture*, in *NETL CO_2 Capture Technology Meeting*. 2013.
54. Amo K.H., Z.; Kaschemekat, J.; Merkel, T.; Pande, S.; Wei, X.; White, S.; Seshadri, P.; Farzan, H., *Pilot Testing of a Membrane System for Post-Combustion CO_2 Capture* in *NETL CO_2 Capture Technology Meeting*. 2014.
55. Wijmans H., Merkel T., Baker R., Lin H., Pande S., Wei X., and Zhou M., *Membrane Solutions for Carbon Capture (Membrane Technology and Research, Inc.)*, in *ICOM 2011*. 2011: Amsterdam.
56. Huang Y., Merkel T.C., and Baker R.W., *Pressure ratio and its impact on membrane gas separation processes.* Journal of Membrane Science, 2014. **463**: p. 33-40.
57. Lasseuguette E., Ferrari M.-C., and Brandani S., *Humidity Impact on the Gas Permeability of PIM-1 Membrane for Post-combustion Application.* Energy Procedia, 2014. **63**(0): p. 194-201.
58. Adymkanov S.V., Yampol'skii Y.P., Polyakov A.M., Budd P.M., Reynolds K.J., McKeown N.B., and Msayib K.J., *Pervaporation of alcohols through highly permeable PIM-1 polymer films.* Polymer Science Series A, 2008. **50**(4): p. 444-450.
59. Hussain A. and Hägg M.-B., *A feasibility study of CO_2 capture from flue gas by a facilitated transport membrane.* Journal of Membrane Science, 2010. **359**(1-2): p. 140-148.
60. Alshehri A., Khalilpour R., Abbas A., and Lai Z., *Membrane Systems Engineering for Post-combustion Carbon Capture.* Energy Procedia, 2013. **37**: p. 976-985.
61. Ramasubramanian K., Verweij H., and Ho W.S., *Membrane processes for carbon capture from coal-fired power plant flue gas: A modeling and cost study.* Journal of Membrane Science, 2012. **421-422**: p. 299-310.
62. Brunetti A., Drioli E., Lee Y.M., and Barbieri G., *Engineering evaluation of CO_2 separation by membrane gas separation systems.* Journal of Membrane Science, 2014. **454**: p. 305-315.
63. *The Costs of CO_2 Capture*. 2009, European Technology Platform for Zero Emission Fossil Fuel Power Plants.
64. DECC, *UK Electricity Generation Costs Update*. 2010.
65. NETL, *Current and Future Technologies for Power Generation with Post-Combustion Carbon Capture - Final Report*, in *DOE/NETL-2012/1557*. 2012, US Department Of Energy.
66. Zhang X., Solli C., Hertwich E.G., Tian X., and Zhang S., *Exergy Analysis of the Process for Dimethyl Ether Production through Biomass Steam Gasification.* Industrial & Engineering Chemistry Research, 2009. **48**: p. 10976-10985.

67. Yuan M., Narakornpijit K., Haghpanah R., and Wilcox J., *Consideration of a nitrogen-selective membrane for postcombustion carbon capture through process modeling and optimization.* Journal of Membrane Science, 2014. **465**: p. 177-184.
68. Kulkarni S., Hasse D., Sanders E., and Chaubey T., *CO_2 capture by Sub-ambient Membrane Operation - Final Scientific Report*. 2013, American Air Liquide.
69. Liu L., Sanders E.S., Kulkarni S.S., Hasse D.J., and Koros W.J., *Sub-ambient temperature flue gas carbon dioxide capture via Matrimid® hollow fiber membranes.* Journal of Membrane Science, 2014. **465**: p. 49-55.
70. Toy L., Kataria A., and Gupta R.P., *CO_2 Capture Membrane Process for Power Plant Flue Gas - Final Technical Report*. 2013, RTI Internationl.
71. Baker R., Wijmans J.G., Merkel T.C., Lin H., Daniels R., and Thompson S., *Gas separation process using membranes with permeate sweep to remove CO_2 from combustion gases*, U.S.P. Application, Editor. 2010, Membrane Technology And Research Inc.
72. Liu F., Hashim N.A., Liu Y., Abed M.R.M., and Li K., *Progress in the production and modification of PVDF membranes.* Journal of Membrane Science, 2011. **375**(1-2): p. 1-27.
73. Scholes C.A., Ho M.T., Wiley D.E., Stevens G.W., and Kentish S.E., *Cost competitive membrane—cryogenic post-combustion carbon capture.* International Journal of Greenhouse Gas Control, 2013. **17**: p. 341-348.
74. *Air Products PRISM Membranes*. Access date: 12/2013; Available from: http://www.airproducts.com/products/Gases/supply-options/prism-membranes.
75. *G8 Hokkaido Toyako Summit (2008) Leaders Declaration*. Access date: 01/2014; Available from: http://www.mofa.go.jp/policy/economy/summit/2008/doc/doc080714__en.html.
76. IEA, *Carbon Capture and Storage, IEA Technology Roadmaps.* 2009.
77. *National Carbon Capture Center*. Access date: 01/2014; Available from: http://www.nationalcarboncapturecenter.com/.
78. NETL, *Advanced Carbon Dioxide Capture R&D Program: Technology Update, May 2011 - APPENDIX B: CARBON DIOXIDE CAPTURE TECHNOLOGY SHEETS - POST-COMBUSTION MEMBRANES*. 2011.
79. *The NANOGLOWA Project*. Access date: 12/2013; Available from: http://www.nanoglowa.com/index.html.
80. *NANOGLOWA Public summary*. 2012.
81. Raats P., *Membrane gas separation for industrial flue gases*, in *ICOM 2011 - Workshop on membrane gas separation for industrial flue gases*. 2011: Amsterdam.
82. DECC, *Digest of UK energy statistics (DUKES)*. 2013.
83. *The New Electricity Trading Arrangements*. Access date: 12/2013; Available from: http://www.bmreports.com/bsp/bsp_home.htm.

84. Chalmers H. and Gibbins J., *Initial evaluation of the impact of post-combustion capture of carbon dioxide on supercritical pulverised coal power plant part load performance.* Fuel, 2007. **86**(14): p. 2109-2123.
85. Chalmers H., Gibbins J., and Leach M., *Valuing power plant flexibility with CCS: the case of post-combustion capture retrofits.* Mitigation and Adaptation Strategies for Global Change, 2011. **17**(6): p. 621-649.
86. Fleming G., *Gas Separation Membranes MEDAL™ Air Liquide*. 2009.
87. Keong L.K., *Feed spacer of spiral-wound membrane module for nanofiltration and reverse osmosis* 2007.
88. Mulder M., *Basic Principles of Membrane Technology* 2nd ed. 1996: Springer.
89. Davis R., *Simple Gas Permeation and Pervaporation Membrane Unit Operation Models for Process Simulations.* Chemical Engineering Technology, 2002. **25**(7): p. 717-722.
90. Levenspiel O., *Chemical Reaction Engineering*. John Wiley & Sons.
91. Weller S. and Steiner W.A., *Engineering aspects of separation of gases.* Chemical Engineering & Progress, 1950. **46**: p. 585.
92. Naylor R.W. and Backer P.O., *Enrichment calculation in gaseous diffusion: Large separation factor.* AIChE Journal, 1955. **1**: p. 95.
93. Kovvali A.S., Vemury S., Krovvidi K.R., and Khan A.A., *Models and analyses of membrane gas permeators.* Journal of Membrane Science, 1992. **73**: p. 1-23.
94. Saltonstall C.W., *Calculation of the membrane area required for gas separations.* Journal of Membrane Science, 1987. **32**: p. 185-193.
95. Giglia S., Bikson B., and Perrin J.E., *Mathematical and Experimental Analysis of Gas Separation by Hollow Fiber Membranes.* Industrial & Engineering Chemistry Research, 1991. **30**: p. 1239-1248.
96. Li K., Acharya D.R., and Hughes R., *Mathematical Modelling of Multicomponent Membrane Permeators.* Journal of Membrane Science, 1990. **52**: p. 205-219.
97. Pan C.Y., *Gas Separation by Permeators with High-Flux Asymmetric membranes.* AIChE Journal, 1983. **29**(4): p. 545-552.
98. Koros W.J. and Lively R.P., *Water and beyond: Expanding the spectrum of large-scale energy efficient separation processes.* AIChE Journal, 2012. **58**(9): p. 2624-2633.
99. Mat N.C., Lou Y., and Lipscomb G.G., *Hollow fiber membrane modules.* Current Opinion in Chemical Engineering, 2014. **4**: p. 18-24.
100. Costello M.J., *Shell-side fluid dynamics and mass transfer through hollow fibre membrane modules*, in *The School of Chemical Engineering and Industrial Chemistry*. 1995, University of New South Wales.
101. Kundu P.K., Chakma A., and Feng X., *Modelling of multicomponent gas separation with asymmetric hollow fibre membranes-methane enrichment from biogas.* The Canadian Journal of Chemical Engineering, 2013. **91**(6): p. 1092-1102.

102. Khalilpour R., Abbas A., Lai Z., and Pinnau I., *Analysis of hollow fibre membrane systems for multicomponent gas separation.* Chemical Engineering Research and Design, 2013. **91**(2): p. 332-347.
103. Chern R.T., Koros W.J., and Fedkiw P.S., *Simulation of a Hollow-Fiber Gas Separator: The Effects of Process and Design Variables.* Ind. Eng. Chem. Process Des. Dev., 1985. **24**: p. 1015-1022.
104. Coker D.T. and Freeman B.D., *Modeling Multicomponent Gas Separation Using Hollow-Fiber Membrane Contactors.* AIChE Journal, 1998. **44**(6).
105. Coker D.T., Allen T., Freeman B.D., and Flemming G.K., *Nonisothermal Model for Gas Separation Hollow-Fiber Membranes.* AIChE Journal, 1999. **45**(7).
106. Ahmad F., Keong L.K., Shariff A.M., and Murshid G., *The Study of Joule Thompson Effect for the Removal of CO_2 from Natural Gas by Membrane Process.* International Journal of Chemical and Environmental Engineering, 2012. **3**(2): p. 15-18.
107. Wang L. and Chung L., *Characterization of hollow fiber membranes in a permeator using binary gas mixtures.* Chemical Engineering Science, 2002. **57**: p. 967-976.
108. Scholz M., Harlacher T., Melin T., and Wessling M., *Modeling Gas Permeation by Linking Nonideal Effects.* Industrial & Engineering Chemistry Research, 2013. **52**(3): p. 1079-1088.
109. Thundyil M.J. and Koros W.J., *Mathematical modeling of gas separation permeators - for radial crossflow, countercurrent, and cocurrent hollow fiber membrane modules.* Journal of Membrane Science, 1997. **125**: p. 275-291.
110. Marriott J. and Sørensen E., *A general approach to modelling membrane modules.* Chemical Engineering Science, 2003. **58**(22): p. 4975-4990.
111. Marriott J.I., Sorensen E., and Bogle I.D.L., *Detailed mathematical modelling of membrane modules.* Computers & Chemical Engineering, 2001. **25**: p. 693-670.
112. Labecki M., Piret J.M., and Bowen B.D., *Two-dimensional analysis of fluid flow in hollow-fibre modules.* Chemical Engineering Science, 1995. **50**(21): p. 3369-3384.
113. Lemanski J. and Lipscomb G.G., *Effect of shell-side flows om the performance of hollow-fiber gas separation modules.* Journal of Membrane Science, 2001. **195**: p. 215-228.
114. Wang K.L. and B. C.E., *Baffled membrane modules made with hollow fiber fabric.* Journal of Membrane Science, 1993. **85**: p. 265-278.
115. Wang K., L.; Cussler, E., L., *Baffled membrane modules made with hollow fiber fabric.* Journal of Membrane Science, 1993. **85**: p. 265-278.
116. Reid R.C., Prausnitz J., M., and Poling B.E., *The properties of gases & liquids* 4ed.: McGraw-Hill Inc.
117. Sinnot R.K., *Coulson & Richardson's Chemical Engineering*. Vol. 6. 1999: Butterworth-Heinemann.
118. Sangani A.S. and Yao C., *Transport processes in random arrays of cylinders. II. Viscous flow.* Physics of Fluids, 1988. **31**(9): p. 2435.

119. Whitacker S., *Flow in Porous Media I: A Theoretical Derivation of Darcy's Law.* Transport in Porous Media 1, 1986(1): p. 3-25.
120. Costello M.J., Fane A.G., Hogan P.A., and Schofield R.W., *The effect of shell side hydrodynamics on the performance of axial flow hollow fibre modules* Journal of Membrane Science, 1993. **80**(1): p. 1-11.
121. Prithiviraj M. and Andrews M.J., *Three Dimensional Numerical Simulation of Shell-and-Tube Heat Exchangers. Part I: Foundation and Fluid Mechanics.* Numerical Heat Transfer, Part A: Applications, 1998. **33**(8): p. 799-816.
122. Rehme K., *Simple method of predicting friction factors of turbulent flow in non-circular channels.* International Journal of Heat and Mass Transfer, 1973. **16**: p. 933-950.
123. Lively R.P., Chance R.R., Koros W.J., Deckman H.W., and Kelley B.T., *Sorbent fiber compositions and methods of temperature swing adsorption*. 2012, Google Patents.
124. Lively R.P., R. C.R., Kelley B.T., Deckman H.W., Drese J.H., Jones C.W., and Koros W.J., *Hollow Fiber Adsorbents for CO_2 Removal from Flue Gas.* Industrial & Engineering Chemistry Research, 2009. **48**: p. 7314–7324.
125. *Engineering Data Book lll*. Wolverine Tube Inc.
126. Qi R. and Henson M., *Approximate modeling of spiral-wound gas permeators.* Journal of Membrane Science, 1996. **121**: p. 11-24.
127. Qi R. and Henson M., *Modeling of Spiral-Wound Permeators for Multicomponent Gas Separations.* Industrial & Engineering Chemistry Research, 1997. **36**: p. 2320-2331.
128. Qi R. and Henson M., *Optimal design of spiral-wound membrane networks for gas separations.* Journal of Membrane Science, 1998. **148**: p. 71-89.
129. Brinkmann T., Pohlmann J., Withalm U., Wind J., and Wolff T., *Theoretical and Experimental Investigations of Flat Sheet Membrane Module Types for High Capacity Gas Separation Applications.* Chemie Ingenieur Technik, 2013. **85**(8): p. 1210-1220.
130. White F.M., *Heat and Mass Transfer*. 1991: Addison-Wesley.
131. Friedrich D., Ferrari M.C., and Brandani S., *Efficient Simulation and Acceleration of Convergence for a Dual Piston Pressure Swing Adsorption System.* Industrial & Engineering Chemistry Research, 2013. **52**(26): p. 8897-8905.
132. Hindmarsh A.C., Brown P.N., Grant K.E., Lee S.L., Serban R., Shumaker D.E., and Woodward C.S., *Sundials: Suite of Nonlinear and Differential/Algebraic Equation Solvers.* ACM Trans. Math. Software, 2005. **31**(3).
133. Finlayson B.A., *The Method of Weighted Residuals and Variational Principles (with application in fluid mechanics, heat and mass transfer)* 1972: Academic Press.
134. Villadsen J. and Michelsen M.L., *Solution of Differential Equations Models by Polynomial Approximation*. 1978: Prentice-Hall, inc.

135. Lemanski J. and Lipscomb G.G., *Effect of fiber variation on the performance of countercurrent hollow fiber gas separation modules.* Journal of Membrane Science, 2000. **167**: p. 241-252.
136. Irwin J.O., *On the Frequency Distribution of the Means of Samples from a Population Having any Law of Frequency with Finite Moments, with Special Reference to Pearson's Type II.* Biometrika, 1927. **19**(3/4): p. 225-239.
137. Walpole R., Myers R., Myers S., and Ye K., *Probability and Statistics for Engineers and Scientists*. 7th edition ed. 2002: Pearson Education.
138. Pettersen T. and Lien K.M., *A new robust design model for gas separating membrane modules, based on analogy with counter-current heat exchangers.* Computers & Chemical Engineering, 1994. **18**(5): p. 427-439.
139. Bhide D.D. and Stern S.A., *Membrane Processes for the Recovery of Acid Gases from Natural Gas: II. Effects od Operating Conditions, Economic Parameters and Membrane Properties.* Journal of Membrane Science, 1993. **81**.
140. Baker R. and Lokhandwala K.A., *Natural Gas Processing with Membranes: An Overview.* Industrial & Engineering Chemistry Research, 2008. **47**: p. 2109-2121.
141. Bocciardo D., Ferrari M.C., and Brandani S., In preparation, 2014.
142. Budd P., Msayib K., Tattershall C., Ghanem B., Reynolds K., McKeown N., and Fritsch D., *Gas separation membranes from polymers of intrinsic microporosity.* Journal of Membrane Science, 2005. **251**(1-2): p. 263-269.
143. Adewole J.K., Ahmad A.L., Ismail S., and Leo C.P., *Current challenges in membrane separation of CO_2 from natural gas: A review.* International Journal of Greenhouse Gas Control, 2013. **17**: p. 46-65.
144. Finkenrath M., *Cost and Performance of Carbon Dioxide Capture from Power Generation*. IEA - International Energy Agency.
145. Hao J., Rice P.A., and Stern S.A., *Upgrading low-quality natural gas with H_2S- andCO_2-selective polymer membranesPart I. Process design and economics of membrane stages without recycle streams.* Journal of Membrane Science, 2002. **209**: p. 177-206.
146. *The Costs of CO_2 Capture, Transport and Storage*. 2009, European Technology Platform for Zero Emission Fossil Fuel Power Plants.
147. DECC, *Electricity Generation Cost Model - 2011 Update Revision 1*. 2011.
148. Rubin E.S., Short C., Booras G., Davison J., Ekstrom C., Matuszewski M., and McCoy S., *A proposed methodology for CO_2 capture and storage cost estimates.* International Journal of Greenhouse Gas Control, 2013. **17**: p. 488-503.
149. *X-rates Currency Calculator*. Access date: 01/2014; Available from: http://www.x-rates.com.
150. Ares E., *Carbon Price Floor*. 2013, House of commons library.
151. *Europe`s Energy Portal*. Access date: 12/2013; Available from: http://www.energy.eu/.
152. Honeywell, *UniSim Design: Customisation Guide*.
153. Kapetaki K., Bocciardo D., Ferrari M.C., Ahn H., and Brandani S., *Performance of Hybrid Membrane – Solvent Configurations for Pre –*

Combustion Carbon Capture in IGCC Power Plants. Procedia Engineering, 2012. **44**: p. 1281-1283.

154. Ozcan D.C., Bocciardo D., Ferrari M.C., Ahn H., Kierzkowska A.M., Müller C.R., and Brandani S., *Comparison of Various Carbon Capture Technologies to Reduce CO_2 Emissions From a Cement Plant,* in *AIChE Annual Meeting*. 2013: San Francisco (US).
155. Honeywell, *Developing Dynamic Unit Operations Exstensions for UniSim Design*
156. Totaro R., *A new OTS feature: dynamic accident simulation,* in *EMEA HUG 2010 (Honeywell Users' Group conference for Europe, Middle-East and Africa*. 2010.